NATIONAL AERONAUTICS AND SPACE ADMINISTRATION

Technical Memorandum 33-478

Applications of Two-Dimensional Integral-Equation Theory to Reflector-Antenna Analysis

W. V. T. Rusch

JET PROPULSION LABORATORY
CALIFORNIA INSTITUTE OF TECHNOLOGY
PASADENA, CALIFORNIA

May 15, 1971

NATIONAL AERONAUTICS AND SPACE ADMINISTRATION

Technical Memorandum 33-478

Applications of Two-Dimensional Integral-Equation Theory to Reflector-Antenna Analysis

W. V. T. Rusch

JET PROPULSION LABORATORY
CALIFORNIA INSTITUTE OF TECHNOLOGY
PASADENA, CALIFORNIA

May 15, 1971

Prepared Under Contract No. NAS 7-100
National Aeronautics and Space Administration

PREFACE

The work described in this report was performed by the Telecommunications Division of the Jet Propulsion Laboratory.

ACKNOWLEDGEMENT

The author wishes to thank Mr. D. A. Bathker for continuing interest and valuable technical discussions, and to acknowledge Mr. J. A. Hatfield for programming the integral-equation solution. In addition, Mr. R. A. Norman provided invaluable assistance with computer liaison.

CONTENTS

CONTENTS (contd)

TABLES

FIGURES

FIGURES (contd)

FIGURES (contd)

ABSTRACT

The Method of Moments is applied to the solution of integral equations for the current induced on conducting cylinders immersed in an arbitrary two-dimensional field. The solution is outlined and such scattering parameters as the induced-field ratio and the extinction cross section are defined. Numerical solutions are obtained for several geometries which are relevant to the problem of large reflector antenna analysis.

I. INTRODUCTION

A. Reflector-Antenna Analysis

Performance analysis of large-aperture reflector antennas has reached a highly developed state. Twenty years ago calculations were based on scalar aperture theory and a few degenerate vector formulations that could be integrated in closed form. With the advent of high-speed computing machines, the complex integrals of physical optics including experimental illumination functions could be evaluated numerically, yielding even more accurate results. Consequently, the analysis of these large antennas has generally kept pace with the development of superb electronic systems used to process the signals from the antenna terminals.

The two most significant problems remaining in the analysis of reflector antennas are:

(1) Aperture blocking and shadowing by struts, supports, or subreflectors within the geometrical shadow of the aperture;

(2) Back radiation into the rear hemisphere.

Various attempts have been made to approximate these effects. However, no genuinely accurate methods have been developed for their quantitative evaluation, particularly with respect to their influence on the antenna sidelobes. While these problems are generally considered to be "higher order effects", more and more systems have come to depend upon the correct evaluation of such effects. For example, the spurious radiation arising from aperture blocking is important in deep-space tracking[1], and will become equally important in tracking synchronous satellites when several are parked close together in orbit. Furthermore, millions of dollars are spent to construct large ground antennas with the highest possible gain, but no really accurate techniques are available to design feed support structures which invariably degrade overall gain.

B. The Integral Equation for the Induced Current Density

The electric field at a point P due to currents on a metallic body can be expressed as an integral of the surface-current density over the surface of the body. In the general formulation of an electromagnetic scattering problem, these currents are induced by a "known" incident field $\bar{E}_{inc}$. The resulting scattered electrical field is subject to the primary boundary condition that its tangential component at the surface of the metallic body is equal to the negative of the tangential component of the incident field. Consequently:

$$-\bar{n} \times \bar{E}_{inc}(P_S) = \frac{\bar{n}x}{4\pi} \int_S \left\{ -j\omega\mu_0 \psi \bar{J}_S + \frac{1}{j\omega\epsilon_0} \left[\bar{J}_S \cdot \nabla \right] \nabla\psi \right\} dS \qquad (I-1)$$

where P_S is on S.

Equation (1) is an integral equation for the surface-current density, $\bar{J}_S$, on the scatterer. This integral equation provides a computational technique to calculate the induced currents. Having determined the currents, it is then straightforward to obtain the scattered field. In the case of a reflector-antenna, $\bar{E}_{inc}$ is the electric field of the feed system. Determination of the resulting scattered field yields the directivity, radiation pattern, and polarization of the antenna.

Analytic solutions to equation (I-1) are generally not possible. However, numerical solutions have been reported in the literature for both two-dimensional[2-4] and three-dimensional[5-7] geometries. These numerical solutions have produced information on the induced currents which had not previously been obtainable using techniques based on geometrical or physical optics. Examples of such new information are the currents flowing in penumbral or completely shadowed regions, and currents flowing in the vicinity of relatively sharp edges. Furthermore, two-dimensional studies have yielded new insights and better quantitative approximations for the difficult problem of aperture blocking by feed-support structures[8] and members of space-frame radomes[9].

The material in this report describes the application of two-dimensional integral-equation theory to the problem of aperture blocking of an idealized two-dimensional parabola. The theory is described in Section II. Alternative descriptions of the scattering characteristics of a conducting cylinder are presented in Section III. These descriptions include "extinction cross-section", which is useful in describing the effects of blocking on sidelobe deterioration, and "induced field ratio" (IFR), which is used advantageously in describing gain loss due to blockage. In Section IV numerical studies are presented for several useful cylinder cross-sections. The double blocking problem is examined in some detail. Finally, in order to evaluate the usefulness of these simple concepts, the entire problem of a parabolic antenna with circular blocking objects is solved. Some of these results can be extrapolated to three-dimensions for a better evaluation of the problem of the blocked and shadowed paraboloid.

II. TWO-DIMENSIONAL INTEGRAL-EQUATION THEORY

The theory of two-dimensional electromagnetic integral equations has received considerable attention during the past decade.[2-4] Large computers have enabled solutions to be obtained for many different sizes and shapes of scatterers. The theory itself, being scalar in nature, is considerably less complex than the more general three-dimensional vector integral theory. The basic two-dimensional integral equation is derived in Appendix A1.

The geometry of the two-dimensional scattering problem is shown in cross-section in Figure II-1. The axis of the scattering cylinder is parallel to the Z-axis. The coordinates of the field point P are (ρ, ϕ); the coordinates of a point on the scatterer are (ρ_0, ϕ_0). The distance between the two points is r. It is convenient to define a localized coordinate system at each point on the scatterer. In the xy plane the coordinates are defined by the outward unit normal vector, $\bar{a}_n$, and the unit tangent vector, $\bar{a}_t$, defined such that

$$\bar{a}_n \times \bar{a}_t = \bar{a}_z \tag{II-1}$$

A. Plane-Wave at Oblique Incidence

In the event that a plane electromagnetic wave is incident upon the scatterer, it is necessary to describe the polarization of the wave and its direction of propagation with respect to the cylinder. The directional relationships are shown in Figure II-2. A propagation vector is defined

$$\bar{k} = k\bar{n} \tag{II-2}$$

where

$$k = \omega \sqrt{\mu_0 \epsilon_0} = 2\pi/\lambda \tag{II-3}$$

$$\bar{n} = \cos\alpha \, (\cos\beta \, \bar{a}_x + \sin\beta \, \bar{a}_y) + \sin\alpha \, \bar{a}_z \tag{II-4}$$

The plane of incidence is the plane containing both the z-axis and the wave normal $\bar{n}$. This plane is defined without ambiguity unless $\bar{n} = \bar{a}_z$. However, this special case shall be excluded from consideration in this report.

It is convenient to define $\bar{a}_{xy}$, a unit vector in the x-y plane that also lies in the plane of incidence:

$$\bar{a}_{xy} \equiv \cos\beta\, \bar{a}_x + \sin\beta\, \bar{a}_y \tag{II-5}$$

so that

$$\bar{n} = \cos\alpha\, \bar{a}_{xy} + \sin\alpha\, \bar{a}_z \tag{II-6}$$

It is also convenient to define $\bar{a}_\perp$, a unit vector in the x-y plane that is perpendicular to the plane of incidence. Then $\bar{a}_z$, $\bar{a}_\perp$, $\bar{a}_{xy}$ constitute a right-handed set of orthogonal unit vectors:

$$\bar{a}_z \times \bar{a}_\perp = \bar{a}_{xy} \tag{II-7a}$$

$$\bar{a}_\perp \times \bar{a}_{xy} = \bar{a}_z \tag{II-7b}$$

$$\bar{a}_{xy} \times \bar{a}_z = \bar{a}_\perp \tag{II-7c}$$

From (II-5) and (II-7c) it may be shown that

$$\bar{a}_\perp = \sin\beta\, \bar{a}_x - \cos\beta\, \bar{a}_y \tag{II-8}$$

Finally, a unit vector $\bar{a}_\parallel$ will be defined such that it lies in both the plane of incidence and the plane wave front. Consequently, $\bar{a}_\parallel$ is perpendicular to both $\bar{n}$ and $\bar{a}_\perp$ and completes a right-handed triplet of orthogonal unit vectors $\bar{a}_\parallel$, $\bar{a}_\perp$, $\bar{n}$:

$$\bar{a}_{\parallel} \times \bar{a}_{\perp} = \bar{n} \tag{II-9a}$$

$$\bar{a}_{\perp} \times \bar{n} = \bar{a}_{\parallel} \tag{II-9b}$$

$$\bar{n} \times \bar{a}_{\parallel} = \bar{a}_{\perp} \tag{II-9c}$$

From (II-4) and (II-9b)

$$\bar{a}_{\parallel} = -\sin\alpha \cos\beta\, \bar{a}_x - \sin\alpha \sin\beta\, \bar{a}_y + \cos\alpha\, \bar{a}_z = -\sin\alpha\, \bar{a}_{xy} + \cos\alpha\, \bar{a}_z \tag{II-10}$$

The electric field of the incident plane, TEM wave is given by

$$\bar{E}^i = \bar{E}_0\, e^{-j\bar{k}\cdot\bar{R}} \tag{II-11}$$

where

$$\bar{R} = x\bar{a}_x + y\bar{a}_y + z\bar{a}_Z \tag{II-12}$$

The phase may be expanded using (II-2), (II-4), and (II-12):

$$\bar{k}\cdot\bar{R} = k\rho\cos\alpha\cos(\phi - \beta) + kz\sin\alpha = kx\cos\alpha\cos\beta$$

$$+ ky\cos\alpha\sin\beta + kz\sin\alpha \tag{II-13}$$

The electric field vector $\bar{E}_0$ lies in the plane of the wavefront, tilted an angle δ with respect to the plane of incidence (Figure II-3). Consequently

$$\bar{E}_0 = E_0(\cos\delta\, \bar{a}_{\parallel} + \sin\delta\, \bar{a}_{\perp}) \tag{II-14}$$

or, in terms of the Cartesian coordinates

$$\bar{E}_0 = E_0 \Big[(\sin\beta \sin\delta - \sin\alpha \cos\beta \cos\delta)\, \bar{a}_x - (\cos\beta \sin\delta + \sin\alpha \sin\beta \cos\delta)\, \bar{a}_y + \cos\alpha \cos\delta\, \bar{a}_z \Big] \tag{II-15}$$

Similarly, the magnetic field of the incident wave is given by

$$\bar{H}^i = \bar{H}_0 e^{-j\bar{k}\cdot\bar{R}} \tag{II-16}$$

where

$$\bar{H}_0 = \frac{1}{\eta} \bar{n} \times \bar{E}_0 \tag{II-17}$$

Inserting (II-4) and (II-15) into (II-17) yields

$$\bar{H}_0 = \frac{E_0}{\eta} \Big\{ (\sin\beta \cos\delta + \sin\alpha \cos\beta \sin\delta)\, \bar{a}_x - (\cos\beta \cos\delta - \sin\alpha \sin\beta \sin\delta)\, \bar{a}_y - \cos\alpha \sin\delta\, \bar{a}_z \Big\} \tag{II-18}$$

This can be further simplified using (II-8) and (II-10) to yield

$$\bar{H}_0 = \frac{E_0}{\eta} (-\sin\delta\, \bar{a}_{\parallel} + \cos\delta\, \bar{a}_{\perp}) \tag{II-19}$$

The vector relationships indicated in eq. (II-19) are verified by the geometrical relationships in Figure II-3.

The general incident field described by equations (II-11), (II-15), (II-16), and (II-18) can be decomposed into an incident E-wave and an incident H-wave (Ref. 10). The incident E-wave has no longitudinal (i.e. z-directed) component of magnetic field

$$\bar{E}_e^i = \bar{E}_e \, e^{-j\bar{k} \cdot \bar{R}} \tag{II-20}$$

where

$$E_{ex} = -E_0 \sin\alpha \cos\beta \cos\delta \tag{II-21a}$$

$$E_{ey} = -E_0 \sin\alpha \sin\beta \cos\delta \tag{II-21b}$$

$$E_{ez} = E_0 \cos\alpha \cos\delta \tag{II-21c}$$

$$H_{ex} = \frac{E_0}{\eta} \sin\beta \cos\delta \tag{II-21d}$$

$$H_{ey} = -\frac{E_0}{\eta} \cos\beta \cos\delta \tag{II-21e}$$

$$H_{ez} = 0 \tag{II-21f}$$

Similarly, the incident H-wave has no longitudinal component of electric field

$$\bar{H}_h^i = \bar{H}_h \, e^{-j\bar{k} \cdot \bar{R}} \tag{II-22}$$

where

$$E_{hx} = E_0 \sin\beta \sin\delta \tag{II-23a}$$

$$E_{hy} = -E_0 \cos\beta \sin\delta \tag{II-23b}$$

$$E_{hz} = 0 \tag{II-23c}$$

$$H_{hz} = \frac{E_0}{\eta} \sin\alpha \cos\beta \sin\delta \tag{II-23d}$$

$$H_{hy} = \frac{E_0}{\eta} \sin\alpha \sin\beta \sin\delta \tag{II-23e}$$

$$H_{hz} = -\frac{E_0}{\eta} \cos\alpha \sin\delta \tag{II-23f}$$

The general scattering problem can now be separated into two independent problems: E-wave and H-wave scattering. The total incident field can be seen to be made of its separated components, e.g. the total x-component of eq. (II-15) consists of the sum of (II-21a) plus (II-23a), etc.

1. Incident E-wave. It shall be assumed that a perfectly conducting, infinitely long, z-directed cylinder (Fig. II-1) is immersed in the field of an incident E-wave. The z-component of the incident field is [from eq (II-21c)]

$$E^i_z = E^i_{z_{xy}} e^{-jkz\sin\alpha} \tag{II-25}$$

where

$$E^i_{z_{xy}} = E_0 \cos\alpha \cos\delta \; e^{-j(kx\cos\alpha\cos\beta + ky\cos\alpha\sin\beta)} \tag{II-26}$$

In terms of the quantities defined in the Appendix A

$$\psi^i_{z_{xy}} \equiv E^i_{z_{xy}} \tag{II-27}$$

Similarly

$$E^s_z = E^s_{z_{xy}} e^{-jkz\sin\alpha} \tag{II-28}$$

$$\psi^s_{xy} = E^s_{z_{xy}} \tag{II-29}$$

and

$$\psi_{xy} = E^i_{z_{xy}} + E^s_{z_{xy}} \tag{II-30}$$

Since $E_{z_{xy}}$ is zero on S_1, eq. (A-32) becomes

$$E_{z_{xy}}(P) = E^i_{z_{xy}}(P) + \frac{j}{4} \int_{S_1} G_{xy} \frac{\partial E_{z_{xy}}}{\partial n} dS \tag{II-31}$$

However

$$\frac{\partial E_{z_{xy}}}{\partial n} = jk\eta \cos^2\alpha \; J_{Sz_{xy}} \tag{II-32}$$

where the surface current density is defined by

$$\bar{J}_S = J_{Sz_{xy}} e^{-jkz\sin\alpha} \bar{a}_z \tag{II-33}$$

Then the scattered field becomes

$$E^s_{z_{xy}} = -\frac{k\eta \cos^2\alpha}{4} \int_{S_1} G_{xy} J_{Sz_{xy}} dS \tag{II-34}$$

and eq. (II-31) is

$$E_{z_{xy}}(P) = E^{i}_{z_{xy}}(P) - \frac{k\eta \cos^2\alpha}{4} \int_{S_1} G_{xy} J_{Sz_{xy}} \, dS \qquad \text{(II-35)}$$

The final integral equation is generated by letting P be a point P_S on the perfectly conducting cylinder so that $E_{z_{xy}}(P_S)$ is zero and

$$\frac{k\eta \cos^2\alpha}{4} \int_{S_1} G_{xy} J_{Sz_{xy}} \, dS = E^{i}_{z_{xy}}(P_S) \qquad \text{(II-36)}$$

a. Piecewise constant current approximation. The integral equation (II-36) for the surface current distribution has been solved by dividing the periphery of the cylinder into N segments (Fig. II-4). Generally, each segment is significantly shorter than a wavelength. The current density on each segment is assumed to be a (complex) constant. Thus (II-36) is transformed into N linear equations in the N unknown current densities

$$\sum_{i=1}^{N} \left\{ \frac{k\eta \cos^2\alpha}{4} \int_{S_i} H_0^{(2)}(k \cos\alpha \, r_{iM}) \, dS_i \right\} \{J_i\} = E^{i}_{z_{xy}}(P_M) \qquad \text{(II-37)}$$

where J_i is the (complex) current density on the ith segment; P_M is a point (fixed) on the Mth segment; r_{iM} is the distance from P_M to the integration point on the ith segment; and the integration is carried out along the ith segment. The coefficients of each current density are evaluated numerically. N equations may be generated by allowing P_M to be on each of the N segments. Special attention must be given to the coefficient of J_M since the argument of the Hankel function vanishes. However, the singularity is integrable and yields

$$\sum_{\substack{i=1 \\ i\neq M}}^{i=N}\left\{\frac{k\eta\cos^2\alpha}{4}\int_{S_i} H_0^{(2)}(k\cos\alpha\, r_{iM})\, dS_i\right\}\{J_i\}$$

$$+ J_M\left\{\frac{k\eta\Delta S_M\cos^2\alpha}{4}\right\}\left\{\left[1 - \frac{(k\Delta S_M)^2}{48}\right] - \frac{2j}{\pi}\left[\log\left(\frac{\gamma k\Delta S_M}{4}\right) - 1\right]\right.$$

$$\left. + j\frac{(k\Delta S_M)^2}{24\pi}\left[\log\left(\frac{\gamma k\Delta S_M}{4}\right) - \frac{1}{3}\right]\right\} = E^i_{z\,xy}(P_M) \qquad \text{(II-38)}$$

where $\log\gamma = 0.5772$. These equations are generally solved using matrix techniques. If the geometry of the scatterer exhibits such symmetries as planes of symmetry, the matrices may be considerably simplified (Appendix B). These symmetries are only functions of the scatterer geometry and not the incident field.

b. The Scattered E-wave. From eq (II-34) the scattered E-Wave is given by

$$E^s_{z\,xy} = -\frac{k\eta\cos^2\alpha}{4}\sum_{i=1}^{N}\left[J_i\int_{S_i} H_0^{(2)}(k\cos\alpha\, r)\, dS_i\right] \qquad \text{(II-39)}$$

At great distances the Hankel function can be approximated by

$$H_0^{(2)}(k\cos\alpha\, r) = \sqrt{\frac{2j}{\pi k\cos\alpha}}\,\frac{e^{-jk\cos\alpha\rho}}{\sqrt{\rho}}\, e^{j\cos\alpha\rho_0\cos(\phi_0-\phi)} \qquad \text{(II-40)}$$

in terms of the geometrical parameters defined in Figures (II-1) and (II-4). Consequently, at great distances the scattered field is

$$E^s_{z_{xy}} = -\frac{k\eta \cos^2\alpha}{4}\left[\sqrt{\frac{2j}{\pi k \cos\alpha}}\frac{e^{-jk\cos\alpha\rho}}{\sqrt{\rho}}\right]\sum_{i=1}^{N}\left[J_i \int_{S_i} e^{jk\cos\alpha\rho_0\cos(\phi_0-\phi)}\, dS_i\right] \tag{II-41}$$

2. Incident H-wave. The scattering cylinder is now assumed to be immersed in an incident H-wave described in eqs. (II-22) and (II-23). From (II-23f) the z-component of the incident field is

$$H^i_z = H^i_{z_{xy}} e^{-jkz\sin\alpha} \tag{II-42}$$

where

$$H^i_{z_{xy}} = -\frac{E_0}{\eta}\cos\alpha \sin\delta\ e^{-j(kx\cos\alpha\cos\beta + ky\cos\alpha\sin\beta)} \tag{II-43}$$

Then, in terms of the quantities defined in Appendix A

$$\psi^i_{xy} \equiv H^i_{z_{xy}} \tag{II-44}$$

Similarly

$$H^s_z = H^s_{z_{xy}} e^{-jkz\sin\alpha} \tag{II-45}$$

$$\psi^s_{xy} \equiv H^s_{z_{xy}} \tag{II-46}$$

and

$$\psi_{xy} = H^{i}_{z_{xy}} + H^{s}_{z_{xy}} \tag{II-47}$$

But

$$\frac{\partial H_{z_{xy}}}{\partial n} = -j\frac{k}{n}\cos^{2}\alpha\ E_{tan_{xy}} \tag{II-48}$$

and E_{tan} is zero on S_1 so that eq. (A-32) becomes

$$H_{z_{xy}}(P) = H^{i}_{z_{xy}}(P) - \frac{j}{4}\int_{S_1} H_{z_{xy}}\frac{\partial G_{xy}}{\partial n}\,dS \tag{II-49}$$

The scattered field is then given by

$$H^{s}_{z_{xy}} = -\frac{j}{4}\int_{S_1} H_{z_{xy}}\frac{\partial G_{xy}}{\partial n}\,dS \tag{II-50}$$

which can be simplified by taking the normal derivative of the Hankel function

$$H^{s}_{z_{xy}} = -\frac{jk\cos\alpha}{4}\int_{S_1}(\bar{a}_r \cdot \bar{n})\,H_1^{(2)}(k\cos\alpha\ r)\,H_{z_{xy}}\,dS \tag{II-51}$$

where $\bar{a}_r$ is a unit vector from the integration point S to the field point P.

If P becomes a point P_S on the cylinder, the final equation is

$$H_{z_{xy}}(P_S) + \frac{jk\cos\alpha}{4}\int_{S_1}(\bar{a}_r \cdot \bar{n})\, H_1^{(2)}(k\cos\alpha\, r)\, H_{z_{xy}}\, dS = H^i_{xy}(P_S) \qquad \text{(II-52)}$$

This is an integral equation for $H_{z_{xy}}$ at the surface of the cylinder. Since $H_{z_{xy}}$ is tangent to the cylinder, it is proportional to the circumferential surface current density.

a. Piecewise constant field/current approximation. The integral equation for $H_{z_{xy}}$ has been solved by again dividing the periphery of the cylinder into N segments (Fig. II-4) and approximating the field/current on each segment by a complex constant, H_i. Equation (II-52) is transformed into N linear equations in the N unknown current densities:

$$\sum_{\substack{i=1\\ i\neq M}}^{i=N}\left\{\frac{jk\cos\alpha}{4}\int_{S_i}\left(\bar{a}_{r_{iM}} \cdot \bar{n}_i\right) H_1^{(2)}(k\cos\alpha\, r_{iM})\, dS_i\right\}\{H_i\}$$

$$+\frac{1}{2}H_M = H^i_{z_{xy}}(P_M) \qquad \text{(II-53)}$$

where $\bar{n}_i$ is the unit outward normal on the ith segment and the unit vector $\bar{a}_{r_{iM}}$ is directed from the integration point on S_i to P_M on the Mth segment. The term involving H_M has been separated from the summation (as for for E-wave) because of the necessity for evaluation of an integrable singularity.

b. The Scattered H-wave. From eq (II-51) the scattered H-Wave is given by

$$H^s_{z_{xy}} = -\frac{jk\cos\alpha}{4}\sum_{i=1}^{N}\left[H_i\int_{S_i}(\bar{a}_r\cdot\bar{n}_i)\,H_1^{(2)}(k\cos\alpha\, r)\,dS_i\right] \quad \text{(II-54)}$$

At great distances the Hankel function can be approximated by

$$H_1^{(2)}(k\cos\alpha\, r) \approx j\sqrt{\frac{2j}{\pi k\cos\alpha}}\,\frac{e^{-jk\cos\alpha\rho}}{\sqrt{\rho}}\,e^{jk\cos\alpha\,\rho_0\cos(\phi_0-\phi)} \quad \text{(II-55)}$$

Consequently at great distances the scattered H-wave is

$$H^s_{z_{xy}} = \frac{k\cos\alpha}{4}\left[\sqrt{\frac{2j}{\pi k\cos\alpha}}\,\frac{e^{-jk\cos\alpha\rho}}{\sqrt{\rho}}\right]\sum_{i=1}^{N}\left[H_i\int_{S_i}(\bar{a}_r\cdot\bar{n}_i)\,e^{jk\cos\alpha\rho_0\cos(\phi_0-\phi)}\,dS_i\right] \quad \text{(II-56)}$$

B. General Field at Normal Incidence

A general two-dimensional electromagnetic field that does not vary in the direction of the cylinder axis (z-direction) can be expanded in terms of one or more E-waves and one-or more H-waves (Ref. 10).

1. Incident E-wave. The basic field components are

$$E^i_z = E^i_z(x, y) \quad \text{(II-57a)}$$

$$H^i_n = (-1/j\omega\mu)\frac{\partial E^i_z}{\partial t} \quad \text{(II-57b)}$$

$$H_t^i = (1/j\omega\mu)\frac{\partial E_z^i}{\partial n} \tag{II-57c}$$

$$E_n^i = E_t^i = H_z^i = 0 \tag{II-57d}$$

where the normal, tangential, and axial (z) directions are defined in Figure II-1 and eq (II-1). The basic integral equation, derived in a manner analogous to eq (II-31) is

$$E_z(P) = E_z^i(P) + \frac{j}{4}\int_{S_1} H_0^{(2)}(kr)\frac{\partial E_z}{\partial n}\,dS \tag{II-58}$$

The integral equation for the z-directed surface-current density is

$$\frac{k\eta}{4}\int_{S_1} H_0^{(2)}(kr)\,J_{Sz}\,dS = E_z^i(P_S) \tag{II-59}$$

The scattered field is

$$E_z^s = -\frac{k\eta}{4}\int H_0^{(2)}(kr)\,J_{Sz}\,dS \tag{II-60}$$

These integrals can be evaluated using the techniques outlined in previous sections.

2. Incident H-wave. The basic field components are

$$H_z^j = H_z^i(x, y) \tag{II-61a}$$

$$E_n^i = (1/j\omega\epsilon)\frac{\partial H_z^i}{\partial t} \tag{II-61b}$$

$$E_t^i = (-1/j\omega\epsilon)\frac{\partial H_z^i}{\partial n} \tag{II-61c}$$

$$H_n^i = H_t^i = E_z^i = 0 \tag{II-61d}$$

The basic integral equation is

$$H_z(P) = H_z^i(P) - \frac{j}{4}\int_{S_1} H_z \frac{\partial}{\partial n}\left[H_0^{(2)}(kr)\right] dS \tag{II-62}$$

and the integral equation for the total H_z at the surface of the scatterer is:

$$H_z(P_S) + \frac{jk}{4}\int_{S_1} (\bar{a}_r \cdot \bar{n})\, H_1^{(2)}(kr)\, H_z\, dS = H_z^i(P_S) \tag{II-63}$$

The scattered field is

$$H_z^s = -\frac{jk}{4}\int_{S_1} (\bar{a}_r \cdot \bar{n}) H_1^{(2)}(kr)\, H_z\, dS \tag{II-64}$$

3. Examples. A useful example of such a two dimensional incident field is

$$\left.\begin{matrix} H_z^i \\ E_z^i \end{matrix}\right\} = A\, e^{-jk\rho\cos(\phi-\beta)} \tag{II-65}$$

which is a normally incident plane wave in the β-direction. This is a special case of the previously derived plane-wave formulas for $\alpha = 0$. A second example is that of a cylindrical wave of the form

$$\left.\begin{matrix} H_z^i \\ \\ E_z^i \end{matrix}\right\} = f(\phi)\,\frac{e^{-jk\rho}}{\sqrt{\rho}} \tag{II-66}$$

which is the field of a directional line feed.

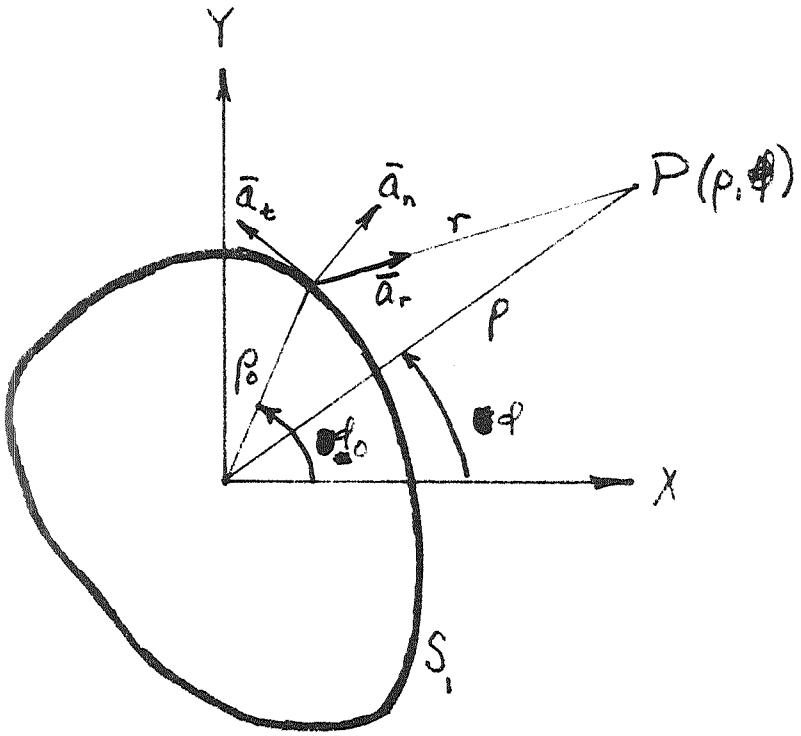

Fig. II-1. Geometry of Scattering Cylinder (Transverse Plane)

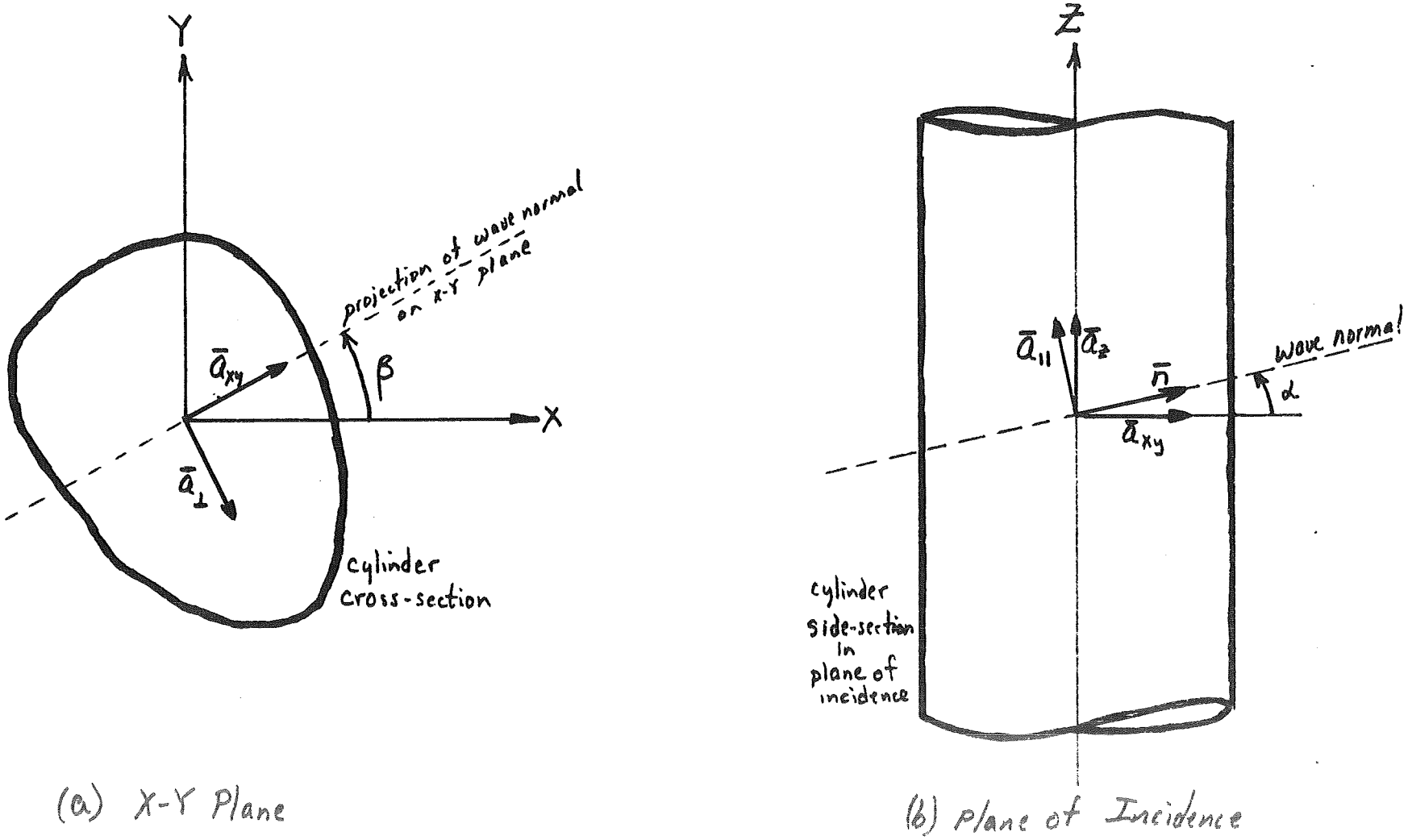

Fig. II-2. Geometry of Plane Wave and Cylinder

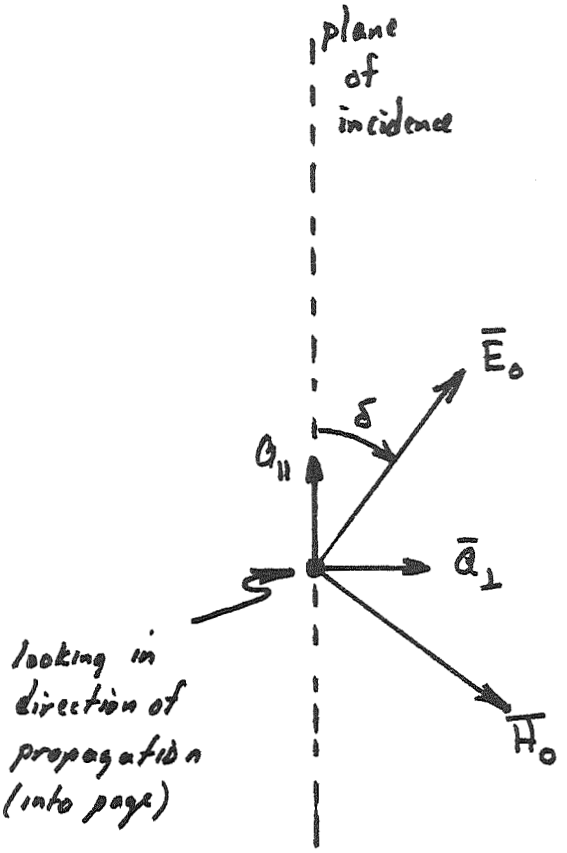

Fig. II-3. Geometry of Plane Wave Polarization Vector

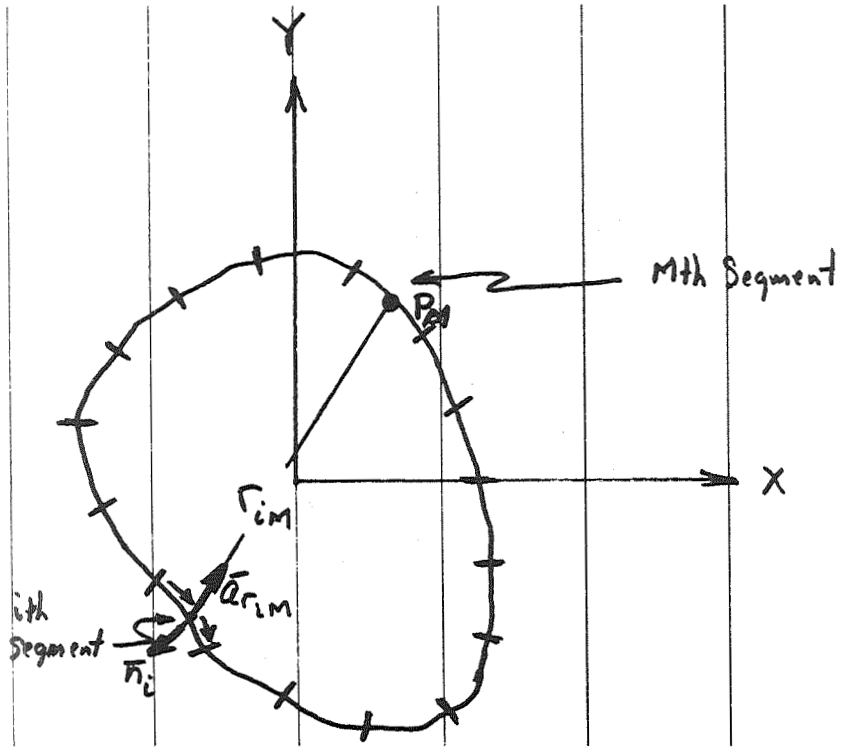

Fig. II-4. Geometry of Discretization of Cylinder Surface

III. SCATTERING PARAMETERS

A. Extinction Cross-Section

The extinction cross-section is a measure of the total power extracted from the incident wave per unit length of the cylinder. As described in Section II, the field of an incident plane, TEM wave may be decomposed into E-wave and H-wave components. The incident, scattered, and total fields are then:

$$E_z^i = E_{z_{xy}}^i e^{-jkz\sin\alpha} \tag{III-1a}$$

$$E_z^s = E_{z_{xy}}^s e^{-jkz\sin\alpha} \tag{III-1b}$$

$$E_z = E_{z_{xy}} e^{-jkz\sin\alpha} \tag{III-1c}$$

where

$$E_{z_{xy}}^i = E_0 \cos\alpha \cos\delta \; e^{-j(kx\cos\alpha\cos\beta + ky\cos\alpha\sin\beta)} \tag{III-2}$$

It may be shown that the total power extracted from the incident wave per unit length of the cylinder is

$$P_{extr} = -\frac{1}{2}\,\mathrm{Re}\left\{\frac{1}{j\omega\mu\cos^2\alpha}\int_{S_1}\left(E_{z_{xy}}^s \frac{\partial E_{z_{xy}}^{i*}}{\partial n} + E_{z_{xy}}^i \frac{\partial E_{z_{xy}}^{s*}}{\partial n}\right) dS\right\} \tag{III-3}$$

By expanding the incident wave using (III-2), the expression for the extracted power becomes

$$P_{extr} = \left(\frac{E_0 \cos\alpha \cos\delta}{2\omega\mu \cos^2\alpha}\right) \mathrm{Re}\left\{ j \int_{S_1} \left[E^s_{z_{xy}} (jk\cos\alpha)\left(\bar{a}_n \cdot \bar{a}_{xy}\right) e^{jk\rho_0\cos\alpha\cos(\phi_0-\beta)} + \frac{\partial E^s_{z_{xy}}}{\partial n} e^{-jk\rho_0\cos\alpha\cos(\phi_0-\beta)} \right] dS \right\} \quad \text{(III-4)}$$

From eq. (A-23) the scattered field is given by

$$E^s_{z_{xy}}(\rho,\phi) = \frac{j}{4} \int_{S_1} \left[G_{xy} \frac{\partial E^s_{z_{xy}}}{\partial n} - E^s_{z_{xy}} \frac{\partial G_{xy}}{\partial n} \right] dS \quad \text{(III-5)}$$

where the Green's function $G_{xy} = H_0^{(2)}(k\cos\alpha r)$. Using the large-argument approximation for the Hankel function at great distances yields

$$E^s_{z_{xy}} \approx \sqrt{\frac{2j}{\pi k\rho\cos\alpha}}\, e^{-jk\rho\cos\alpha} E_0 \cos\alpha \cos\delta\, f(\phi) \quad \text{(III-6)}$$

where

$$f(\phi) = \frac{1}{E_0 \cos\alpha \cos\delta} \frac{j}{4} \int_{S_1} \left[\frac{\partial E^s_{z_{xy}}}{\partial n} e^{jk\rho_0\cos\alpha\cos(\phi_0-\phi)} - jk\cos\alpha\left(\bar{a}_n \cdot \bar{a}_r\right) E^s_{z_{xy}} e^{+jk\rho_0\cos\alpha\cos(\phi_0-\phi)} \right] dS \quad \text{(III-7)}$$

The angular function, $f(\phi)$, is normalized by the magnitude of the incident field so that it is the pattern for a unit-amplitude normally incident E-wave. Combination of eqs. (III-4) and (III-7) yields the power extracted from the E-wave to be:

$$P_{extr} = -\frac{2}{\omega\mu} E_0^2 \cos^2\delta \; \mathrm{Re}\left\{f(\beta)\right\} \qquad \text{(III-8)}$$

Consequently it is only necessary to determine the real part of the pattern factor of the scattered field in the direction of the incident field to determine the total power extracted.

A similar analysis of the power extracted from the H-wave component of the incident field yields

$$P_{extr} = -\frac{2}{\omega\mu} E_0^2 \sin^2\delta \; \mathrm{Re}\left\{g(\beta)\right\} \qquad \text{(III-9)}$$

where $g(\phi)$ is the pattern function obtained for a unit-amplitude normally incident H-wave:

$$g(\phi) = \frac{1}{\left(-\frac{E_0}{\eta}\cos\alpha \sin\delta\right)} \frac{j}{4} \int_{S_1} \left[\frac{\partial H_z^s}{\partial n}_{xy} e^{+jk\rho_0\cos\alpha\cos(\phi_0-\phi)} \right.$$

$$\left. -jk\cos\alpha \left(\bar{a}_n \cdot \bar{a}_r\right) H_{z\,xy}^s e^{+jk\rho_0\cos\alpha\cos(\phi_0-\phi)} \right] dS \qquad \text{(III-10)}$$

and, at great distances

$$H_{z\,xy}^s(\rho,\phi) \approx \sqrt{\frac{2j}{\pi k\rho\cos\alpha}} e^{-jk\rho\cos\alpha} \left(-\frac{E_0}{\eta}\cos\alpha \sin\delta\right) g(\phi) \qquad \text{(III-11)}$$

Since the two mode types are orthogonal, the total power extracted from the incident wave is the sum of (III-8) and (III-9)

$$P_{extr} = -\frac{2}{\omega\mu} E_0^2 \left[\cos^2\delta \, \mathrm{Re}\{f(\beta)\} + \sin^2\delta \, \mathrm{Re}\{g(\beta)\}\right] \qquad \text{(III-12)}$$

The extinction cross-section, σ_e, is then defined as the ratio of P_{extr} and the incident power density, $E_0^2/2\eta$:

$$\sigma_e = -\frac{4}{k}\left[\cos^2\delta \, \mathrm{Re}\{f(\beta)\} + \sin^2\delta \, \mathrm{Re}\{g(\beta)\}\right] \qquad \text{(III-13)}$$

The derivation has been sufficiently general to include lossy cylinders for which the extracted power includes dissipative losses as well as the scattered power. In the case of a perfectly conducting cylinder, however, the extracted power includes only the scattered power. Consequently, the extinction cross-section in the material to follow is effectively a "total scattering cross-section" and provides a useful measure of the total scattered energy in all directions.

B. Differential Scattering Cross-Section

It may be shown that at great distances the power density of the scattered field in the (α, ϕ) direction is

$$S(\alpha, \phi) = \frac{E_0^2}{\pi\omega\mu\rho}\left[\frac{\sin^2\delta \left|g(\phi)\right|^2 + \cos^2\delta \left|f(\phi)\right|^2}{\cos\alpha}\right] \qquad \text{(III-14)}$$

The differential scattering cross-section in the (α, ϕ) direction is

$$\sigma(\alpha, \phi) = \frac{2\pi\rho \cos\alpha \, S(\alpha, \phi)}{E_0^2/2\eta} = \frac{4}{k}\left[\sin^2\delta \left|g(\phi)\right|^2 + \cos^2\delta \left|f(\phi)\right|^2\right] \qquad \text{(III-15)}$$

This quantity provides a measure of the power density of the scattered field in a particular direction. It is conventionally used to describe the scattered field for a purely E- or purely H-wave at normal incidence. In this case

$$\sigma_e(\phi) = \frac{4}{k}\left|f(\phi)\right|^2 \tag{III-16a}$$

$$\sigma_h(\phi) = \frac{4}{k}\left|g(\phi)\right|^2 \tag{III-16b}$$

If $\phi = \beta$, $\sigma(\beta)$ is the "forward scattering cross-section." If $\phi = \pi + \beta$, $\sigma(\pi + \beta)$ is the "backscattering cross-section" or two-dimensional "radar cross-section."

C. Equivalent Aperture Radiation

1. Radiation from a One-dimensional Aperture. A one-dimensional aperture is defined as a segment of the ξ-axis in Figure III-1. The figure shows the ξ and η coordinate axes in the $z = 0$ plane of an ξ-η-z coordinate system. (Consequently, the one-dimensional aperture may also be interpreted as an infinitely long slit in the z-direction provided that there is no variation of the fields in the z-direction.) If u is one of the six rectangular electric or magnetic field components subject to the wave equation and the radiation condition, and if u is zero everywhere on the ξ-axis except between ξ_1 and ξ_2, then it may be shown that

$$u(\xi_0, \eta_0) = -\frac{jk}{2}\int_{\xi_1}^{\xi_2} u(\xi, 0)\, H_1^{(2)}(k\rho)\, d\xi \tag{III-17}$$

where

$$\rho = \sqrt{\eta_0^2 + (\xi - \xi_0)^2} \tag{III-18}$$

If u represents a rectangular component of the electric field, both sides of eq. (III-17) may be multiplied by a constant unit vector $\bar{e}$ which represents the polarization

$$u(\xi_0, \eta_0)\,\bar{e} = -\bar{e}\,\frac{jk}{2}\int_{\xi_1}^{\xi_2} u(\xi, 0)\, H_1^{(2)}(k\rho)\, d\xi \qquad \text{(III-19)}$$

Let P be a distant field point in the $\xi_0 = 0$ direction so that

$$\eta_0 \gg |\xi_1| \qquad \text{(III-20a)}$$

$$\eta_0 \gg |\xi_2| \qquad \text{(III-20b)}$$

$$\rho \approx \eta_0 \qquad \text{(III-20c)}$$

$$H_1 \approx j\sqrt{\frac{2j}{\pi k\rho}}\; e^{-jk\rho} \qquad \text{(III-20d)}$$

Furthermore, assume $u(\xi, 0) = E_0$. Then

$$u(0, \eta_0)\,\bar{e} = \bar{E}_{REF} \qquad \text{(III-21)}$$

where

$$\bar{E}_{REF} = RE_0\,\bar{e} \qquad \text{(III-22a)}$$

$$R = \frac{(k\xi_2 - k\xi_1)}{2}\sqrt{\frac{2j}{\pi k\eta_0}}\; e^{-jk\eta_0} \qquad \text{(III-22b)}$$

2. E-wave induced field ratio, IFR_E. The aperture concepts of the previous section will now be applied to the two-dimensional scattering geometry shown in Figure III-2. A plane wave travels in the $\phi = \beta$ direction relative to the x-axis. The E-field of the wave is polarized in the z-direction. The coordinate system (ξ, η, z) is defined such that the η-axis is coincident with the direction of propagation. The fields may then be written as

$$\bar{E}^i = E_0 \bar{a}_z e^{-jk\eta} \qquad \text{(III-23a)}$$

$$\bar{H}^i = \frac{E_0}{Z_0} \bar{a}_\xi e^{-jk\eta} \qquad \text{(III-23b)}$$

A perfectly conducting cylindrical scatterer of arbitrary cross-section lies in the path of the wave. The axis of the cylinder is parallel to the z-axis and the cylinder lies in the vicinity of the origin. A z-directed surface current J_{Sz} is induced on the cylinder, which, in turn, generates a scattered field $E_z^s \bar{a}_z$. At a field point $P(0, \eta_0)$ on the η-axis the forward-scattered field is [cf. eq. (II-34)]:

$$E_z^s = -\frac{k\eta_0}{4} \int_{S_1} J_{Sz} H_0^{(2)}(k\rho)\, dS \qquad \text{(III-24)}$$

For a distant field point $H_0^{(2)}(k\rho)$ may be approximated by its asymptotic value.

A reference aperture is now defined by the projection of the scatterer onto the $\eta = 0$ plane from $\xi = \xi_1$ to $\xi = \xi_2$. A reference field $\bar{E}_{REF}$ is now defined as the field radiated to P by the portion of the incident field in the reference aperture. With $\bar{e} = \bar{a}_z$ in eq (III-22) the reference field is:

$$\bar{E}_{REF} = \frac{k\xi_2 - k\xi_1}{2} \sqrt{\frac{2j}{\pi k\eta_0}}\, e^{-jk\eta_0} \bar{a}_z \qquad \text{(III-25)}$$

The Induced Field Ratio (IFR_E) is defined so that

$$\bar{E}_z^s(P) = (IFR_E)\,\bar{E}_{REF} \tag{III-26}$$

or

$$IFR_E = \frac{E_z^s}{R\bar{E}_0} \tag{III-27}$$

In general, IFR_E is a complex quantity. In the limit of very high frequencies IFR_E approaches -1. As a result, the field at P is equal to the field of the wave with the portion of the wavefront in the geometrical shadow of the cylinder cancelled. This is known as the "optical blocking" approximation.

3. H-wave induced field ratio, IFR_H. The incident plane wave and the (ξ, η, z) coordinate system are again defined in Fig. III-2. However the H-field is polarized in the z-direction so that

$$\bar{H}^i = H_0\,\bar{a}_z\,e^{-jk\eta} = \frac{E_0'}{Z_0}\,\bar{a}_z\,e^{-jk\eta} \tag{III-28a}$$

$$\bar{E}^i = Z_0 H_0(-\bar{a}_\xi)\,e^{-jk\eta} = E_0'(-\bar{a}_\xi)\,e^{-jk\eta} \tag{III-28b}$$

A circumferential surface-current density distribution $H_z(S)$ is induced on the cylinder (i.e., the current flows in planes of constant z). This current gives rise to a scattered field $\bar{H}^s$ which is also z-directed. At a distant field point $P(0, \eta_0)$ the forward scattered field is

$$\bar{H}^s(P) = -\frac{j}{4}\,\bar{a}_z \int_{S_1} H_z(S)\,\frac{\partial}{\partial n}\left[H_0^{(2)}(k\rho)\right] dS \tag{III-29a}$$

$$\bar{E}^s(P) = \eta_0 \bar{H}^s(P) \times \bar{a}_\eta \tag{III-29b}$$

A reference aperture is again defined as before. Reference fields may be defined, alternatively, for the E- or H-fields

$$\bar{E}_{REF} = R\, E_0'(-\bar{a}_\xi) \tag{III-30a}$$

or

$$\bar{H}_{REF} = R\, H_0\, \bar{a}_z \tag{III-30b}$$

and the H-Wave Induced Field Ratio, IFR_H, is defined so that

$$\bar{E}^s(P) = (IFR_H)\, \bar{E}_{REF} \tag{III-31a}$$

or

$$\bar{H}^s(P) = (IFR_H)\, \bar{H}_{REF} \tag{III-31b}$$

Consequently

$$IFR_H = \frac{H_z^s}{RH_0} = -\frac{E_\xi^s}{RE_0'} \tag{III-32}$$

4. IFR for arbitrary linear polarization. Assume the incident field vectors to be rotated an angle δ with respect to the coordinate axes as shown in Figure III-3. Then

$$\bar{E}^i = E_0\, \bar{e}\, e^{-jk\eta} \tag{III-33a}$$

where

$$\bar{e} = \cos\delta\, \bar{a}_z + \sin\delta\, \bar{a}_\xi \tag{III-33b}$$

Similarly

$$\bar{H}^i = \frac{E_0}{Z_0} \bar{e}_c \, e^{-jk\eta} \tag{III-34a}$$

where

$$\bar{e}_c = -\sin\delta \, \bar{a}_z + \cos\delta \, \bar{a}_\xi \tag{III-34b}$$

From eqs (III-26) and (III-31a)

$$\bar{E}^s(P) = (IFR_E) \, RE_0 \cos\delta \, \bar{a}_z + (IFR_H) \, RE_0 \sin\delta \, \bar{a}_\xi \tag{III-35}$$

Expanding $\bar{a}_z$ and $\bar{a}_\xi$ yields

$$\bar{E}^s(P) = RE_0 \left[\cos^2\delta \, IFR_E + \sin^2\delta \, IFR_H\right]\bar{e}$$

$$+ RE_0 \left[IFR_H - IFR_E\right] \sin\delta \cos\delta \, \bar{e}_c \tag{III-36}$$

Hence the scattered field has both normally-polarized and cross-polarized components. If the scattered field is defined in terms of these components:

$$\bar{E}^s(P) = RE_0 \, IFR_N \, \bar{e} + RE_0 \, IFR_C \, \bar{e}_c \tag{III-37}$$

then, by comparison with (III-36)

$$IFR_N = \cos^2\delta \, IFR_E + \sin^2\delta \, IFR_H \tag{III-38a}$$

$$IFR_C = (IFR_H - IFR_E) \sin\delta \cos\delta \tag{III-38b}$$

5. IFR for circular polarization. In terms of the coordinates of Figure III-2, assume the polarization of the incident field to be right handed circular polarization

$$\bar{e} = \bar{e}_R = \frac{1}{\sqrt{2}}\left(\bar{a}_z + j\,\bar{a}_\xi\right) \tag{III-39}$$

Then,

$$\bar{E}^i = E_0\,\bar{e}_R\,e^{-jk\eta} \tag{III-40}$$

From eqs (III-26) and (III-31a)

$$\bar{E}^s(P) = \frac{RE_0}{\sqrt{2}}\left[IFR_E\,\bar{a}_z + j\,IFR_H\,\bar{a}_\xi\right] \tag{III-41}$$

If a unit vector describing left handed circular polarization is defined by

$$\bar{e}_L = \frac{1}{\sqrt{2}}\left(\bar{a}_z - j\,\bar{a}_\xi\right) \tag{III-42}$$

then, by expanding $\bar{a}_z$ and $\bar{a}_\xi$ in terms of $\bar{a}_R$ and $\bar{a}_L$ yields

$$\bar{E}^s(P) = RE_0\left\{\left(\frac{IFR_E + IFR_H}{2}\right)\bar{e}_R + \left(\frac{IFR_E - IFR_H}{2}\right)\bar{e}_c\right\} \tag{III-43}$$

Consequently unless IFR_E and IFR_H are equal the scattered field has both right-handed and left-handed circular polarization. It is then possible to define

$$IFR_{RR} = \frac{IFR_E + IFR_H}{2} \tag{III-44a}$$

$$IFR_{RL} = \frac{IFR_E - IFR_H}{2} \qquad \text{(III-44b)}$$

so that the incident field can be defined as

$$\bar{E}^s(P) = RE_0 \left[IFR_{RR}\, \bar{e}_R + IFR_{RL}\, \bar{e}_L \right] \qquad \text{(III-45)}$$

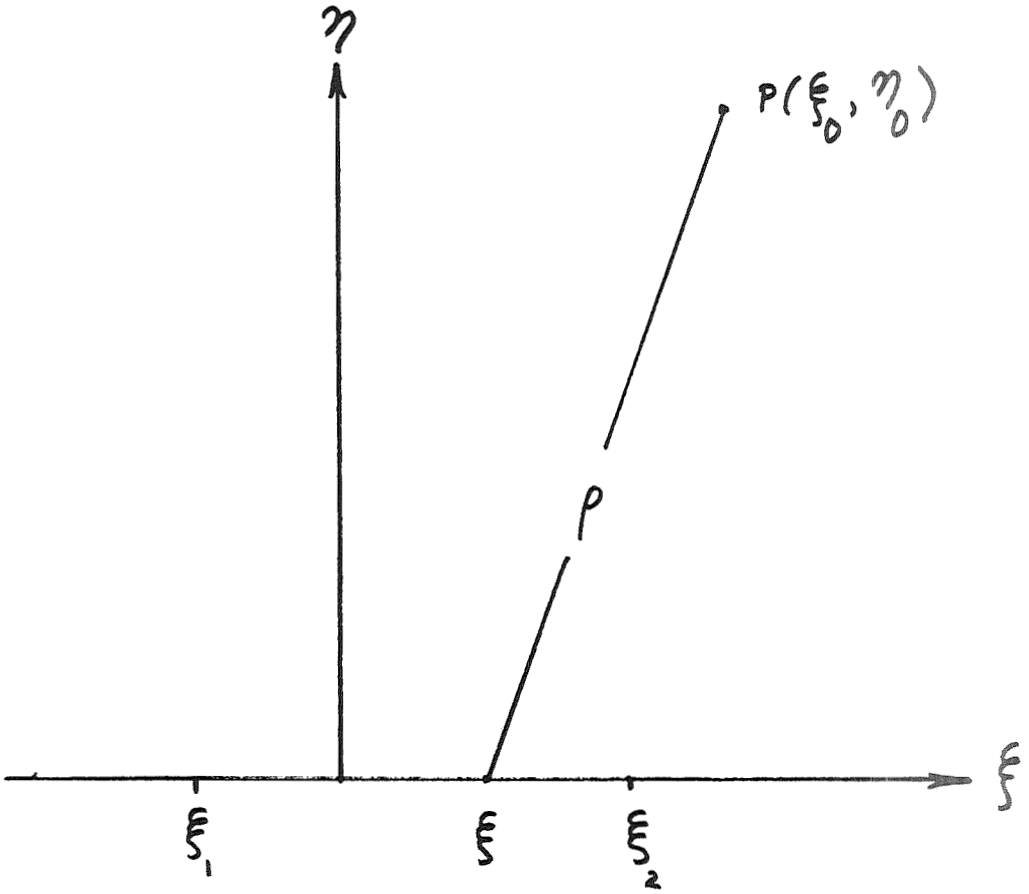

Fig. III-1. Geometry of One-Dimensional Aperture

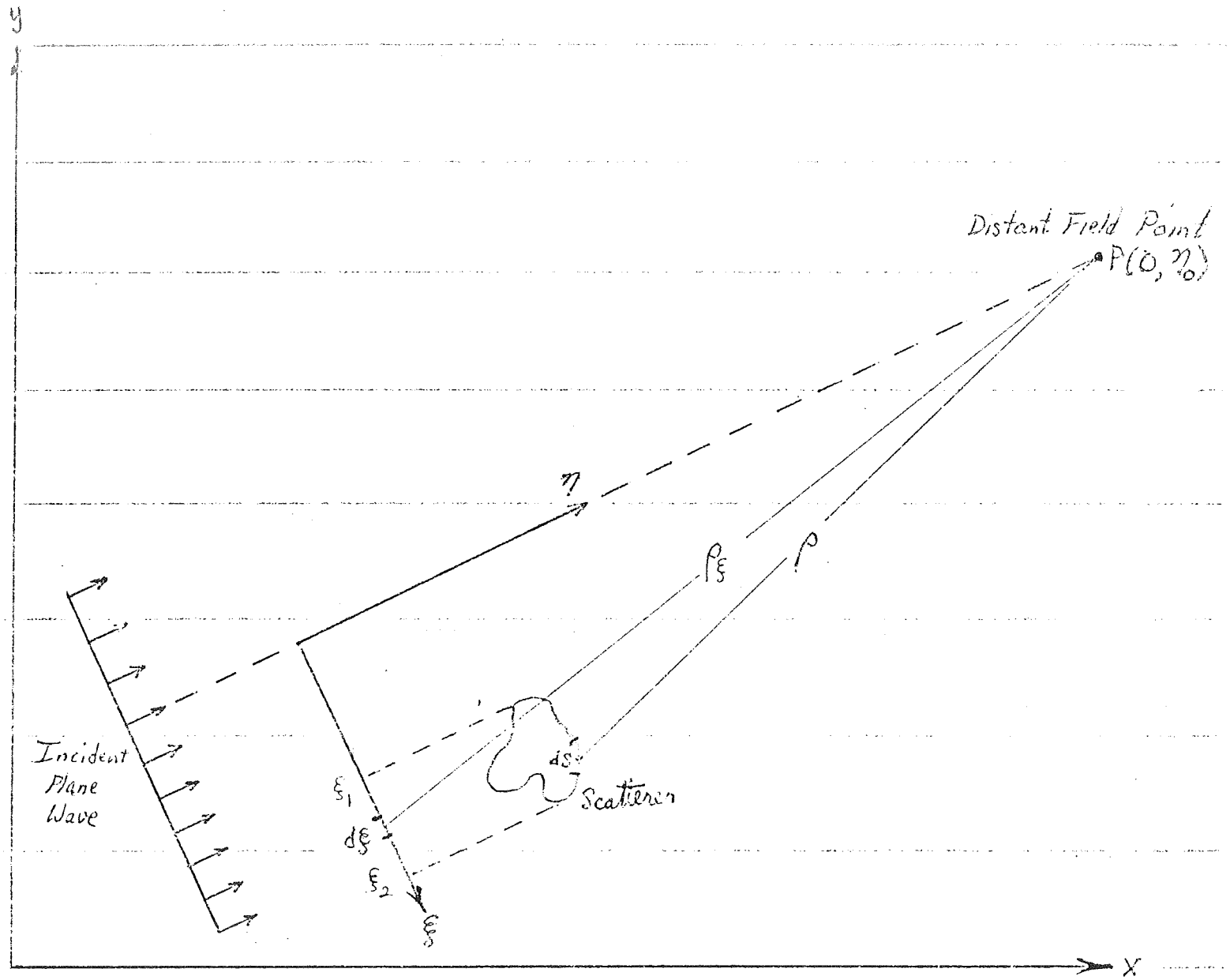

Fig. III-2. Geometry for Induced Field Ratio

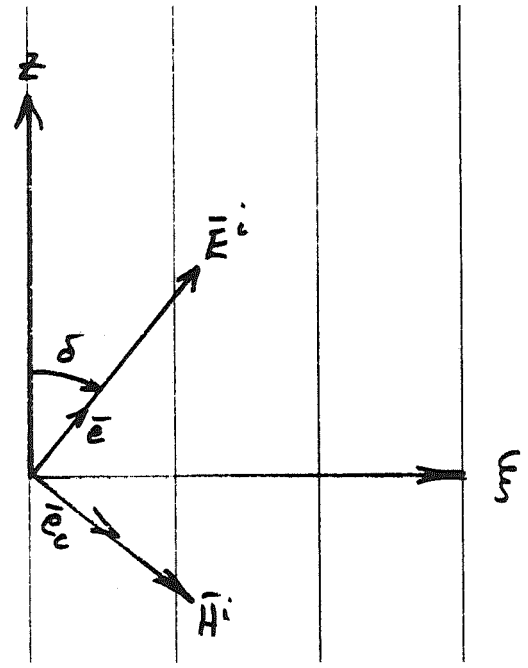

Fig. III-3. Geometry of Polarization Vector

IV. NUMERICAL STUDIES

A. Right-Circular Cylinder

The right-circular cylinder presents a useful cross-sectional geometry with which to begin a numerical study of cylindrical scattering because (1) classical results are available for the right-circular cylinder and can be used to check the numerical accuracy of the numerical process, and (2) the right-circular cylinder is a base-line configuration that can be used to check the "reasonableness" of other configurations.

The current induced on a right-circular cylinder by an incident plane wave may be tabulated in terms of an infinite series of Hankel functions[11]. These classical results are plotted in Figure IV-1 (dashed curves) for E- and H-waves incident on a right-circular cylinder of diameter equal to one wavelength. The current distributions were also computed using eqs. (II-38) and (II-53). These "integral-equation" results are plotted as the solid curves in the figure. The surface of the cylinder was divided into 20 equal segments on which the current density was assumed piecewise constant. The two different processes yield results which are very nearly equal, with slight differences which are most noticeable in regions where the current changes more rapidly than the non-vanishing segment size can detect.

The induced field ratios for a right-circular cylinder are given by

$$IFR_E = -\frac{1}{ka}\sum_{n=-\infty}^{+\infty}\frac{J_n(ka)}{H_n^{(2)}(ka)} \qquad \text{(IV-1)}$$

$$IFR_H = -\frac{1}{ka}\sum_{n=-\infty}^{+\infty}\frac{J_n'(ka)}{H_n^{(2)'}(ka)} \qquad \text{(IV-2)}$$

Similarly, the total scattering cross-section of a right-circular cylinder [cf. eq. (III-13)] is given by

$$\frac{\sigma}{2a} = (-2) \times \mathrm{Re}\left\{\mathrm{IFR}\right\} \tag{IV-3}$$

These results are plotted in Figure IV-2. The magnitude of IFR approaches unity as the radius/wavelength ratio increases, with IFR_H approaching monotonically from below, and IFR_E approaching monotonically from above. Similarly, the total scattering cross-section approaches 4a with increasing radius/wavelength ratio, with the H-wave result approaching monotonically from below and the E-wave result approaching monotonically from above.

The induced field ratio was also computed using integral-equation techniques for a one-wavelength-diameter cylinder with 20 equal segments. The results are indicated below:

$$\mathrm{IFR}_E = \begin{cases} -1.229 + j0.407 = 1.294 \angle 161.7 \text{ deg} & \text{(Classical)} \\ -1.234 + j0.413 = 1.302 \angle 161.5 \text{ deg} & \text{(Int. Eq.)} \end{cases} \tag{IV-4}$$

$$\mathrm{IFR}_H = \begin{cases} -0.765 - j0.268 = 0.811 \angle -160.7 \text{ deg} & \text{(Classical)} \\ -0.773 - j0.288 = 0.825 \angle -159.5 \text{ deg} & \text{(Int. Eq.)} \end{cases} \tag{IV-5}$$

The accuracy of the integral-equation result reflects the corresponding accuracy with which the integral-equation technique is capable of determining the current distribution induced on a right-circular cylinder. Although it should not be inferred that corresponding accuracy can be achieved for other cross-sectional shapes, these are the accuracies which one might expect providing (a) the density of segments per wavelength of arc length is comparable or higher; (b) the density of segments per angle of curvature is comparable or higher; (c) roundoff errors from the matrix inversion process may be neglected.

If a plane wave is incident on a right circular cylinder from directions other than at right angles to the cylinder axis, the induced field ratios are

$$IFR_E(\alpha) = -\frac{1}{ka\cos\alpha}\sum_{n=-\infty}^{+\infty}\frac{J_n(ka\cos\alpha)}{H_n^{(2)}(ka\cos\alpha)} \qquad \text{(IV-6)}$$

$$IFR_H(\alpha) = -\frac{1}{ka\cos\alpha}\sum_{n=-\infty}^{+\infty}\frac{J_n'(ka\cos\alpha)}{H_n^{(2)'}(ka\cos\alpha)} \qquad \text{(IV-7)}$$

where α is the angle between the wave normal and the normal to the cylinder axis (cf. Figure II-2). Consequently, in the determination of the induced field ratio, the effective radius of the cylinder is simply reduced by the factor $\cos\alpha$. Although this result is derived for a right-circular cylinder, similar results are valid for scattering cylinders with other cross-sections: dimensions in the transverse plane are effectively reduced by the factor $\cos\alpha$.

Figure IV-3 is a plot of $|IFR_E|$ versus α for diameter/wavelength ratios of 0.1, 1.0, and 10.0. These curves increase with α because the reduction in effective radius causes $|IFR_E|$ to increase (cf. Figure IV-2). As α increases from zero, the IFR_E remains initially constant before beginning to increase monotonically. The range over which IFR_E remains essentially constant is only a few degrees for $D/\lambda = 0.1$, but is as much as 30-40 degrees for larger D/λ. Consequently, for waves that are almost normally incident, a good first-order approximation can be made by assuming IFR_E to be independent of α. However, this approximation is not valid at large angles for which the exact value of IFR_E must be computed.

Figure IV-4 is a plot of $|IFR_H|$ versus α for the same three diameter/wavelength ratios. These curves decrease monotonically as the effective radius decreases. However, the values of IFR_H are essentially constant for angles not far from normal incidence, similar to the behavior described in the previous paragraph.

B. Two Coupled Right-Circular Cylinders

Calculations were made for the problem of plane-wave scattering from two coupled right-circular cylinders, each of which is one wavelength in diameter. Integral-equation techniques were used to compute the current distributions and the IFR's for E- and H-wave scattering. Each cylinder was subdivided into twenty segments for the analysis.

The resulting IFR magnitudes are plotted as functions of the separation, D, in Figure IV-5, for separations lateral to the wave direction, and in Figure IV-6, for separations in the wave direction. When the two cylinders are separated laterally:

(1) For small or moderate separations the IFR exhibits coupling effects in the form of a series of resonances and anti-resonances oscillating about the value of 1.294 for the E-wave and 0.811 for the H-wave (cf. eqs. IV-4 and IV-5).

(2) As the separation continues to increase the oscillations decay and the IFR approaches the value expected from each obstacle considered separately.

However, when the two cylinders are separated in the direction of the wave normal:

(1) For small or moderate separations the IFR's again exhibit coupling effects;

(2) For large separations the IFR's approach twice the value expected from a single obstacle, although continuing to oscillate about the asymptotic value due to the differential phasing of the contributions from the two cylinders.

It appears from the results of Figure IV-6, that when two scatterers are separated by a great distance relative to their transverse dimensions, even though one scatterer lies within the shadow of the second (as cast by the incident wave) the wave "fills in" behind the first scatterer so that essentially free-space scattering occurs at each scatterer. This principle is illustrated by the current density distributions plotted in Figure IV-7. Two right-circular cylinders are separated by a distance of 15 wavelengths in the direction of

the incident wave. The dashed curves are the classical, free-space, single-cylinder current distributions. For both incident E- and H-waves the current on the forward cylinder closely resembles the free-space value with the exception of slight oscillations in the H-wave current and a moderate low-level enhancement in the E-wave current. The H-wave current on the rear cylinder closely follows the free-space value. However, the E-wave current on the rear cylinder closely resembles the free-space current but is uniformly reduced by 10-20%. To first order, then, for both E- and H-waves incident, the currents induced on these widely separated cylinders closely resemble the free-space value. Consequently, the effect on the forward-scattered field is a superposition of each scatterer considered separately. The implications of this result in estimating reflector antenna aperture blocking by complex support structures are significant. It is insufficient to take the projected area of the entire blocking structure when different members of the structures are separated by great distances compared to their transverse dimensions. Instead, one must account for all of the widely separated members without eliminating overlapping.

When the separation between the two one-wavelength-diameter cylinders is 15 wavelengths in the direction of propagation:

$$IFR_H = -1.48 - j0.44 = 1.54 \angle -163.4 \text{ deg} \qquad \text{(IV-8a)}$$

$$IFR_E = -2.05 + j0.83 = 2.21 \angle 158.0 \text{ deg} \qquad \text{(IV-8b)}$$

These values are almost double the free-space values of eqs. (IV-4) and (IV-5), suggesting the "filling in" mechanism by which essentially free-space scattering occurs at both cylinders. It appears possible to exclude the incident wave from the shadow region behind the first cylinder to prevent it from scattering from the second. Such a geometry is shown in Figure IV-8b; it is simply an elongated cross-section with parallel sides 15 wavelengths long, one wavelength apart, and capped by semicircular ends. For this geometry, with the wave incident from the same direction as before:

$$IFR_H = -0.79 - j0.27 = 0.83 \angle -161.2 \text{ deg} \qquad \text{(IV-9)}$$

This remarkable result indicates that the H-wave blocking by the elongated structure in nearly identical to the blocking by a single cylinder (Eq. IV-5) and only about half the value for two separated cylinders (Eq. IV-8a). Addition of the conducting sides has indeed prevented the wave from "filling in" behind the first cylinder.

Unfortunately, the E-wave blocking deteriorates even further for the elongated structure because the boundary condition of zero-tangential-electric field on the long sides of the structure is not inherently satisfied by the incident field. For the E-wave

$$IFR_E = -2.93 + j1.96 = 3.53 \angle 146.3 \text{ deg} \qquad \text{(IV-10)}$$

Furthermore, for circular polarization

$$IFR_{CP} = \frac{IFR_E + IFR_H}{2} \qquad \text{(IV-11)}$$

In which case, for the single cylinder

$$IFR_{CP} = -0.99 + 0.07 = 1.0 \angle 176.0 \text{ deg} \qquad \text{(IV-12)}$$

For the two cylinder combination

$$IFR_{CP} = -1.77 + j0.19 = 1.78 \angle 173.9 \text{ deg} \qquad \text{(IV-13)}$$

For the elongated cylinder

$$IFR_{CP} = -1.86 + j0.85 = 2.04 \angle 155.4 \text{ deg}$$

Consequently, the aperture blocking of a circularly polarized wave increases by adding sides to the two cylinders. Furthermore, a significant cross-polarized component is excited.

A second structure proposed to reduce "filling in" without violating the electric boundary condition is illustrated in Figure IV-8c. This corrugated

surface has quarter-wavelength grooves to present an "opencircuited" surface to the incident E-wave. The absolute accuracy of the results is questionable, because of the extremely large peripheral length. These results were

$$IFR_E = -2.75 + j2.15 = 3.49 \angle 142.0 \text{ deg} \qquad \text{(IV-14a)}$$

$$IFR_H = -2.67 + j1.39 = 3.00 \angle 152.5 \text{ deg} \qquad \text{(IV-14b)}$$

This type of a surface appears to increase both IFR's, with the corresponding enhancement of the effective aperture blocking cross-section. The preceding analysis was repeated for structures 7.5 wavelength long, leading to essentially the same conclusions.

C. Square Cylinders

1. One cylinder. Mei and Van Bladel[12] first analyzed the problem of plane-wave scattering from rectangular cylinders using integral equations. The basic structural member on the AAS* feed system configuration is a square cylinder, 8.9 cm (3.50 in.) on a side with an 0.48-cm (0.19-in.) radius on the corners (Figs. IV-9 and IV-10). These slightly modified square cylinders were analyzed using eqs. (II-38) and (II-52). At a frequency of 2295 MHz, the dimension of the straight side, S, was 0.606 wavelength, and the dimension of the radius, R, was 0.0369 wavelength (cf. Fig. IV-11). The analysis was carried out with eight segments per side and four segments per corner. The incident plane wave was first normally incident against the face of the square (incident wave #1) and then normally incident against one of the rounded corners (incident wave #2). The analysis was then repeated at an angle of 62.5 degrees from normal incidence. This direction corresponds to the actual oblique angle at which the "aperture" wave strikes the support members of the AAS feed system (Figure IV-9).

The current densities induced by a normally incident E-wave are plotted in Figure IV-12(a). The most noticeable feature of these current distributions is the current density peaks at the four corners. These peaks, although

*Advanced Antenna System located at Goldstone, California

pronounced, are not nearly as sharp as those reported by Mei and Van Bladel for the rectangular cylinders with abrupt corners. In the case of incident wave #1 there is symmetry about the x-axis so that two large current peaks exist on the two leading corners A and D, while the peaks on the trailing corners B and C are much smaller. For incident wave #2 the symmetry exists about the diagonal so that there is only a single large peak on leading corner A, with intermediate peaks on corners B and D, and a very small peak on the trailing corner C. For reference, the current density on a right-circular cylinder with equal circumference (2.657 wavelength) is plotted in the figures. The current densities induced by a plane wave incident at 62.5 deg from normal incidence are plotted in Figures IV-12(b). The results are very similar to those in (a), although the densities are somewhat higher (as expected, because the effective physical cross-section is reduced by a factor of cos 62.5 = 0.462).

The current densities induced by an incident H-wave are plotted in Figure IV-13, first for normal incidence (a) and then for 62.5 deg from normal incidence (b). The edge peaks are not found for the H-wave, and the results are quite similar to those for the right-circular cylinders with equal circumferences.

The IFR's of the square cylinder for normal incidence are tabulated in Table IV-1 together with corresponding IFR's for four reference cylinders of circular cross-section. The reference cylinders are

(a) equal diameter as "seen" by incident wave #1, i.e., 0.680 wavelength. This right-circular cylinder can be inscribed within the square cylinder;

(b) equal cross-sectional area, i.e., 0.461 square wavelengths. The diameter is 0.766 wavelength;

(c) equal circumference, i.e., 2.657 wavelength. The diameter is 0.846 wavelength;

(d) equal diameter as "seen" by incident wave #2, i.e., 0.931 wavelength. This right-circular cylinder can be circumscribed around the square cylinder.

The IFR magnitudes for electric, magnetic, and circular polarization are tabulated. From eq. (III-43) it will be recalled that the IFR for circular polarization is equal to the algebraic mean of the E- and H-wave IFR's. In order to compare the different geometries the quantity (width)x(IFR) is also plotted. This quantity yields the effective blocking contribution on the forward-scattered field since the IFR alone is normalized by the width (cf. eqs. III-22b, III-27). From observing the first two rows of the Table it may be seen that the blocking by the square cylinder of incident wave #1 is slightly greater than the blocking of incident wave #2. In the case of the E-wave, this result can be interpreted in terms of the edge peaks of the current distribution described previously: at 45 degrees only one major edge peak is excited, whereas at zero degrees two edge peaks are excited. In the case of the H-wave the interpretation is more obscure. The most intrinsically significant number in the first two rows of the table is the value of 1.099 for the H-wave IFR magnitude for the square cylinder (incident wave #1). It will be called from Figure IV-2 that for a right-circular cylinder the IFR magnitude of an H-wave is always less than unity. Consequently, the H-wave scattering of the square cylinder is relatively enhanced. Although intermediate directions for the incident wave were not considered, it will be assumed that the IFR's for the two incident waves will effectively bound the range of values for arbitrary directions. Consequently, the wIFR product seen by a circularly polarized wave normally incident on the square cylinder ranges from 0.797 to 0.893.

The blocking parameters of the four reference cylinders are plotted in the four bottom rows of Table IV-1. The electric IFR magnitudes decrease toward unity as the diameter increases while the magnetic IFR magnitudes increase toward unity. The circular polarization magnitudes are close to unity over the range. The wIFR product for the two smaller circular cylinders is less than that of the square cylinder for the E-wave and circular polarization. Because the magnetic scattering appears enhanced for the square cylinder, three of the circular cylinders have smaller wIFR products than the square cylinder. It appears to be most useful to compare the square cylinder with the circular cylinder of equal cross-sectional area because these two geometries have the same support strength. In this case the circular cylinder has 1-5% less E-wave blocking, 19-20% less H-wave blocking, and 4-15% less blocking for circular polarization.

Table IV-2 presents the extinction cross-sections for the square and reference cylinders at normal incidence. The extinction cross-section (Section III-A) yields the total energy extracted from the incident wave. For circular polarization the extinction cross-section is the algebraic mean of the electric and magnetic values. In all cases the circular cylinder of equal cross-sectional area scatters significantly less energy than the square cylinder.

The parameters described in the preceding paragraphs are tabulated in Tables IV-3 and IV-4 for square and reference circular cylinders with the two incident waves tilted 62.5 degrees from normal incidence. Virtually all of the previous comments concerning the relative blocking and scattering properties of the square and circular cylinders are again applicable. For circular polarization the circular cylinder with equal cross-sectional area causes 4% less blocking and 5% less scattering.

The actual structural member on the AAS feed system support is a seamless tube of 8.9 x 8.9 cm^2 (3.5 x 3.5 $in.^2$) square cross-section. The wall thickness is 0.6 cm (1/4 in.). The total cross-sectional area of the metal tube is 21 cm^2 (3.25 $in.^2$). The radius of gyration ($r = \sqrt{I/A}$), an important mechanical property of the member, is 1.3307. The 0.6-cm wall thickness has no effect on the rf scattering properties of the structure since the skin depth in steel at S-band is 0.5 x 10^{-3} cm (0.2 mil).

A practical comparison of the AAS square support members with equivalent circular tubes requires that only commercially available circular tubes be considered, since a special machine run for non-standard sizes would be prohibitively expensive. The two available seamless round tubes that most nearly matched the cross-sectional area and radius of gyration of the square tube were:

Seamless Tube #1: 10.2 cm (4 in.) outer diameter; 0.7 cm (9/32-in.) wall thickness; 21.2 cm^2 (3.29 $in.^2$) cross-section; 1.3185 radius of gyration

Seamless Tube #2: 10.5 cm (4-1/8 in.) outer diameter; 0.7 cm (9/32-in.) wall thickness; 21.9 cm^2 (3.40 $in.^2$) cross-section; 1.3626 radius of gyration

The scattering properties of these two seamless round tubes were calculated and are also included in Tables IV-1 to IV-4. These two commercially available round tubes most nearly match the two important mechanical properties of the square tubes actually used in the AAS supports. It may be

seen that for the case of 62.5 deg incidence, the blocking afforded by the circular cross-section is of the order of 1-2% less than for the square tube, and the scattering decrease is less than a percent.

2. Array of four square cylinders. Each quadripod leg shown in Figures IV-9 and IV-10 consists of four single square tubes, each of which is the size considered in the previous section, arranged in the form of a rectangular parallelepiped. Cross-members are also arranged for additional structural support but these cross-members are not considered in the following analysis. The fields scattered from this array of four square cylinders were calculated for an incident plane wave coming from the direction shown in Figure IV-14, both for normal incidence, and for 62.5 deg from normal incidence. To first order, the plane wave may be interpreted as the field reflected from the paraboloidal surface and radiated into space. The 62.5 degree angle of incidence corresponds to the actual angle at which the reflected wave strikes the quadripod legs.

The currents induced on each of the four cylinders by a normally incident plane wave are plotted in Figures IV-15 (E-wave) and IV-16 (H-wave). Symmetry is evident about the midplane. With the exception of moderate assymetry due to proximity effects, the currents induced on all four cylinders are the same as those induced on a square cylinder alone in free space (Figs. IV-12 and IV-13). The total effective blocking area ($w\left|IFR_E\right|$) for the E-wave is 4.18 versus four times the value of a single square cylinder (1.096) equalling 4.384. Similarly, for the H-wave $w\left|IFR_H\right|$ is 2.92 compared with four times the single-cylinder value of 2.99; for circular polarization $w\left|IFR_{CP}\right|$ is 6.62 and four times the single cylinder value is 7.06. Similarly, for all three polarizations, the extinction cross-section of the four-cylinder array is slightly less than four times the cross-section of a single cylinder.

The currents induced by a plane wave at 62.5 deg incidence are shown in Figures IV-17 and IV-18. These are similar to the currents induced on the single cylinder in free space. Similarly, the effective blocking and extinction cross-sections of the array are slightly less than four times the values for free space (Cf. Table IV-5). Consequently, the above evidence indicates that, similar to the results in Section IV-B, when the separation is as large as 10-20 wavelengths, the blocking and scattering properties of several scatterers are

simply the sum of the blocking and scattering of the individual components, whether or not the members of the array lie in each other's shadow.

D. Scattering from a Parabolic Cylinder

1. Line feed. A useful application of two-dimensional scattering theory has been suggested by Ruze[8] and Kay[9] for those members of a feed support structure that are sufficiently long and thin to approximate the equivalent infinite structure. One may assume, in addition, that the fields emerging from the reflector* are sufficiently planar to enable the induced-field-ratio (IFR) parameters to be used in calculating gain loss due to blocking by these members. Ruze has additionally applied the same concept to "shadowing" of the reflector caused by feed-support members interposed between the reflector and direct illumination from the feed. One may further suppose that the extinction cross-sections of the equivalent infinite structures may be used to determine effects on average sidelobe levels, etc.

Unfortunately, this method for blocking calculation lacks analytical or experimental confirmation, although it appears intuitively to be reasonable. A possible analytical confirmation of the method would be a complete solution of the finite circular aperture with a finite feed support structure using integral-equation techniques. Until such a solution becomes feasible numerically, the next best piece of analytical evidence might be provided by an integral-equation solution of the two-dimensional version of the problem. Such a solution has been undertaken below. The geometry is illustrated in Figure IV-19. Because the problem has a plane of symmetry, only half of the reflector is shown. The front of the reflector consists of 90 linear segments, each about 0.175λ in length, the endpoints of which lie on a parabolic cylinder defined by the polar equation

$$\rho_0 = \frac{6.27\lambda}{\cos^2\left(\frac{\phi_0}{2}\right)} \qquad \text{(IV-15)}$$

*The transmit mode is conceptually simpler than the receive mode in the derivation. By reciprocity, the conclusions reached are equally applicable in either transmit or receive.

Consequently, the front of the reflector approximates a parabolic cylinder with a focal length of 6. 27 wavelength. The geometrical aperture diameter is 15 wavelengths. The reflector is 0. 1 wavelength thick, and the back is subdivided into 90 similar segments. The edges of the reflector are semicircular, of radius 0. 05 wavelength, and add an additional 0. 148 wavelength to the geometrical diameter of the aperture. Each semi-circular edge is divided into five segments 0. 031 wavelength long.

The incident field illuminating the reflector consists of a line source located at the origin (which is also the focus of the parabola.) The incident field intensity is given by

$$\left.\begin{matrix} E_z^i \\ \\ H_z^i \end{matrix}\right\} = \frac{\sec\left(\frac{\phi_0}{2}\right) e^{-jk\rho_0}}{\sqrt{\rho_0/\lambda}} \qquad \text{(IV-16)}$$

in the direction of the reflector and zero in other directions. Consequently, the field incident on the front of the reflector is uniform in magnitude, producing (in geometrical terms) a uniformly illuminated aperture.

Calculations were carried out for the parabola alone, and the parabola in the presence of two symmetrically placed one-wavelength-diameter circular cylinders. In one case (blocking) the cylinders are placed in the focal plane so as not to intercept direct radiation from the line source but to affect (block) the scattered fields due to the currents induced on the parabola. In the other case (blocking and shadowing) the cylinders are placed closer to the reflector so as to intercept direct radiation from the feed before it illuminates portions of the reflector (shown with dotted lines in the figure) while at the same time blocking scattered radiation from the parabola.

a. E-wave illumination. The field of equation IV-16, with the electric vector parallel to the z-axis, was used to illuminate the parabolic reflector (in the absence of the blocking cylinders). The current density induced on each reflector segment was computed and is plotted in Figure IV-20. Only the current density induced on the symmetric half of the reflector shown in Figure IV-20 is plotted. The abscissa is the linear path length (in wavelengths)

along the front and back of the reflector. The current density varies uniformly along the illuminated front of the reflector, has a moderate peak at the edge (light-shadow boundary), and drops by two orders of magnitude to a rapidly damped oscillation on the back. For comparison, the physical-optics approximation to the induced current density is also shown on the figure. The two currents are virtually the same on the illuminated front, except for a slight perturbation in the integral-equation result near the edge of the reflector. The physical-optics current drops to zero at the edge and remains zero on the back of the reflector. The current density on the shadowed back of the reflector rapidly decays 40 dB below its value on the front. It is not known whether the damped oscillations are computational or physical in nature. (The oscillations appear to be damped in the wrong direction to be explained by the standard interpretation of interference between two damped surface waves from each of the two edges.) These oscillations were calculated for other diameter/wavelength ratios and other illumination tapers with E-vector polarization.

The scattered field of the unblocked reflector has been calculated from the induced currents. In this and other calculations of the scattered field, only the field on antenna boresight (i. e., radiated in the negative x-direction) has been computed. The phase of the scattered field on boresight is -14. 4 deg. (physical optics) and -15. 7 deg. (integral-equation). The amplitude of the boresight field is 19. 01 or 18. 82 (depending upon whether the rounded corners are included in the calculation or not) from physical optics and 19. 01 using the integral equation. *

Placing the pair of cylinders in the blocking position in the focal plane causes a modification of the currents on the parabola, as shown in Figure IV-21. The current variation on the front of the reflector has changed from monotonic to a significant oscillation. Similarly, the oscillatory pattern on the back has been modified significantly, although the magnitude of these currents is still down by approximately 40 dB. For reference, the currents on the unblocked reflector are also plotted in the figure.

*The field amplitudes given are in arbitrary units. Only relative differences are significant.

The density of the current induced on one of the blocking cylinders is plotted in Figure IV-22. Near-zone fields of the reflector may be approximated using the geometrical interpretation that a plane wave is initially scattered from the reflector. Consequently, to provide a reference, the current induced on a free-space right-circular cylinder by an incident planar E-wave of a magnitude given by the plane wave scattered geometrically from the parabola is also plotted in Figure IV-22, as computed both by the classical normal-mode solution and as computed by the integral-equation method. Except for low magnitudes, these two are indistinguishable. It may be seen that the currents induced on the blocking cylinders closely resemble those induced on a cylinder in free space by a plane wave of comparable magnitude, although the amplitude of the currents on the blocking cylinders averages 10-20% higher.

Evaluation of the boresight field in the presence of the blocking cylinders was based on both the "optical" blocking approximation, i. e., $IFR_E = -1$, and the presumably more accurate use of the IFR for this particular cylinder, i. e., a right-circular cylinder one wavelength in diameter. This value is $IFR_E = 1.29 \angle 161.7$ deg. Furthermore, it was possible to compute the scattered field with the integral-equation method using the complete set of scattering surfaces as the integration surface. This result will be used to evaluate the accuracy of the approximation techniques. The calculations are presented and discussed below.

(1) Computed Field = 15. 22 - j3. 38 = 15. 59 $\angle$ -12. 51 deg.

(2) Field estimated optically:

Unblocked field (computed)	= 18. 31 - j5. 14
Optical blocking correction	= -2. 43 - j0. 62
Net field	= 15. 88 - j4. 51 = 16. 50 $\angle$ -15. 87 deg.

Consequently, the optical estimate of the field (16. 50) is significantly larger than the computed field (15. 59). The effects of the right-circular cylinder on the incident E-wave are underestimated by the optical approximation.

(3) Field estimate using IFR:

Unblocked field (computed)	= 18.31 - j5.14
IFR blocking correction	= -2.73 + j1.76
Net field	= 15.57 - j3.38 = 15.94 $\angle$ -12.25 deg.

Use of the E-wave IFR for the blocking cylinder has significantly improved the estimate of the boresight field. It is possible to obtain even better agreement if use is made of the fact that the current induced on the blocking cylinder is 10-20% higher than expected from the geometrical field. If a blocking correction is generated using 1.1 x IFR, the boresight field is estimated to be 15.63 $\angle$ -11.84 deg. compared to the computed value of 15.59 $\angle$ -12.51 deg. The ultimate goal is use of the IFR as a universal "weighting factor" to calculate blocking. The observation that the actual current is 10-20% higher does not facilitate such calculations. However, it does serve to provide a plausible physical explanation as to the source of the remaining (small) discrepancy.

Finally, the problem was again solved with the two cylinders shifted forward so as to intercept radiation from the feed. The currents induced on the parabola are plotted in Figure IV-23, in addition to the reference currents of the unblocked parabola. Strong oscillations are evident in both the illuminated and shadowed regions. Furthermore, the current in the shadowed regions of the reflector is significantly reduced although not eliminated.

The cylinder current distribution for this location of the cylinder is plotted in Figure IV-24. The current was computed directly using the integral equation for the complete cylinder-parabola geometry. In addition, a current distribution was constructed by superimposing the current induced by the line feed in free space and the current induced by a plane wave equal in magnitude and phase to the quasi-planar wave reflected from the reflector. The superposition solution is a relatively good approximation to the integral-equation current, indicating again that superposition concepts, such as those suggested by Ruze and Kay, appear to be applicable to the blocking and shadowing problem.

Evaluation of the boresight field in the presence of the cylinders (which now both block and shadow the reflector) has been carried out using the IFR to estimate the blocking, and both the optical approximation and additional IFR correction to estimate the shadowing. The calculations are presented below.

(1) Computed field = 11.55 - j1.95 = 11.71 $\angle$ -9.58 deg.

(2) Field with IFR estimate of blocking and optical estimate of shadowing:

Unblocked field (computed)	= 18.31 - j5.14
IFR blocking correction	= -2.73 + j1.76
Optical shadowing correct.	= -4.22 + j1.09
Net field	= 11.35 - j2.30 = 11.58 $\angle$ -11.44 deg.

This estimate has simply applied a factor of -1 to the radiation from the shadowed portions of the front of the reflector. The agreement between the estimated and computed fields is satisfactory, in spite of the fact that the currents in the shadowed regions are not completely negligible (cf. Figure IV-23).

(3) Field with IFR estimate of blocking and IFR estimate of shadowing:

Unblocked field (computed)	= 18.31 - j5.14
IFR blocking correction	= -2.73 + j1.76
IFR shadowing correction	= -4.75 + j3.05
Net field	= 10.82 - j0.33 = 10.83 $\angle$ -1.75 deg.

Consequently, it appears that for the electric polarization, application of the IFR to the shadowed region overcompensates for the shadowing and produces a significant difference between the estimated and computed results.

This provides at least one piece of evidence in favor of using an optical correction to the shadowed region, rather than using the IFR. Mathematically, this seems justifiable since the IFR was originally derived for far-zone scattered fields.

b. H-wave illumination. The previous set of calculations was repeated with the field from the source at the focus of the parabola polarized with its magnetic vector parallel to the axis of the reflector. The illumination is again tapered inversely to produce a uniform aperture illumination. The current density induced on the reflector is plotted in Figure IV-25. This figure is similar to Figure IV-20 except that now the induced currents flow in planes perpendicular to the reflector axis. The physical-optics current density is plotted on the figure for reference. The agreement between the physical-optics and computed currents on the front of the reflector is again excellent, although the computed current exhibits a significant oscillation. Unlike the electric polarization, an edge-diffracted surface wave is predicted for an incident H-wave, and the oscillations superimposed on the physical-optics results may be attributed to interferences between these two surface waves. The computed currents on the rear of the reflector do not decay as fast as they did for the incident E-wave, and the oscillations in the back region may be interpreted in terms of decaying surface waves interacting.

Again, there is excellent agreement between the fields computed using physical optics and computed using the integral-equation technique. The computed phase is 165.9 deg. vs. 165.6 deg. (physical optics) and the computed amplitude is 19.07 vs. 19.01 (physical optics).

The presence of the pair of cylinders in the focal plane has only a minor influence on the parabola surface currents. The induced current density is plotted in Figure IV-26 and compared with the unblocked currents. The currents on the front of the reflector are more modified than those on the back, where only the depths of the nulls seem affected.

The currents induced on one of the blocking cylinders are plotted in Figure IV-27. Also plotted are the currents induced on on a free-space right-circular of the same size with an incident plane wave of comparable

magnitude. Agreement is again generally good, although the computed currents seem to average slightly above the expected free-space values.

Evaluation of the effects of blocking on the boresight field have been estimated both geometrically and using the IFR estimate. For an H-wave, the IFR of a right-circular cylinder of one wavelength diameter is $IFR_H = 0.81 \angle -160.68$ deg. Results of the calculations are presented below.

(1) Computed field $= -15.65 + j5.33 = 16.54 \angle 161.19$ deg.

(2) Field estimated optically:

Unblocked field (computed)	$= -18.50 + j4.65$
Optical blocking correction	$= +2.43 - j0.62$
Net field	$= -16.06 + j4.02 = 16.56 \angle 165.94$ deg.

The optical correction thus provides an excellent estimate of the boresight field in the presence of blocking.

(3) Field estimated using IFR:

Unblocked field (computed)	$= -18.50 + j4.65$
IFR blocking correction	$= 2.03 + j0.17$
Net field	$= 16.47 + j4.82 = 17.16 \angle 163.68$ deg.

Estimating the effects of blocking using the H-wave IFR produces a value that is 4% high. Again, this may be due to the fact that the actual currents on the cylinders are higher than that due to the equivalent plane wave from which the IFR value was originally computed. If a blocking correction is generated using 1.3 x IFR, the boresight field is estimated to be $16.59 \angle 162.91$ deg., which is very close to the computed result.

The currents induced on the parabola when the blocking cylinders are shifted forward into the path of the feed energy are plotted in Figure IV-28. The deviations from the unblocked currents are severe, both on the front and back of the reflector. There is a noticeable decrease in the current

amplitude shifted slightly from the region of geometrical shadowing. However, the magnitude of the current in this region is far from being negligible.

The cylinder current distribution for the cylinder located in the position which both blocks and shadows the reflector is plotted in Figure IV-29. The complete integral equation result is plotted as well as a reference current using superposition of the cylinder currents induced by the line feed alone and the reflected plane wave alone. The agreement is again relatively good.

Evaluation of the boresight field under the influence of the blocking and shadowing of the cylinders was carried out in a manner similar to the E-wave calculations. Again, two different methods were used to estimate the shadowing.

(1) Computed field $= -11.98 + j5.58 = 13.21 \angle 155.03$ deg.

(2) Field with IFR estimate of blocking and optical estimate of shadowing:

Unblocked field (computed)	$= -18.50 + j4.65$
IFR blocking correction	$= 2.03 + j0.17$
Optical shadowing correction	$= 4.23 - j1.09$
Net field	$= -12.24 + j3.74 = 12.80 \angle 163.02$ deg.

(3) Field with IFR estimate of blocking and IFR estimate of shadowing:

Unblocked field (computed)	$= -18.50 + j4.65$
IFR blocking correction	$= 2.03 + j0.17$
IFR shadowing correction	$= 3.52 + j0.30$
Net field	$= -12.94 + j5.13 = 13.92 \angle 158.39$ deg.

Consequently, use of the optical shadowing correction produces a slightly better approximation to the boresight field than the IFR shadowing correction. The case in favor of optical shadowing is not nearly as strong

as it was for the E-wave, however, because the IFR blocking approximation appears to be less accurate than the optical correction. Since the current in the shadowed region is not as small as optically predicted, it is clear that use of the IFR to approximate H-wave shadowing may be a reasonable thing to do. However, under no circumstances does it appear reasonable to use the E-wave IFR to estimate shadowing since the magnitudes of E-wave IFR's are typically greater than unity.

c. Radiation pattern. The pattern of the field radiated from the 15-wavelength-diameter, line-fed, uniformly illuminated parabolic cylinder is plotted in Figure IV-30 for both polarizations. The field is normalized to unity in the boresight direction. In this case no blocking obstacles are present, and the feed is assumed to radiate no direct energy in the boresight direction. The patterns show a well-behaved sidelobe envelope decay. Aperture theory predicts that the first sidelobe of a uniformly illuminated rectangular aperture is 13.2 dB below the peak of the main beam, whereas the integral-equation results yielded first sidelobe levels of -13.76 dB and -13.75 dB for the E-wave and H-wave, respectively.

2. Radar cross-section. The radar cross-section (backscattering cross-section) for the 15-wavelength-diameter parabolic cylinder with an incident plane wave is plotted in Figure IV-31 (E-wave) and IV-32 (H-wave). It has been assumed that no feed is present in the focal region. In a less-idealized case the presence of a feed would significantly affect the energy directed toward the focal region. The figures present the back-scattered patterns for the bare reflector alone. It is seen that virtually all of the backscattered energy is confined to a wedge with a half-angle of about 23 degrees from boresight, in both the forward and rearward directions.

Table IV-1. Comparison of IFR's for Square Cylinder and Equivalent Circular Cylinders — Normal Incidence

	Width, w (wavelength)	$\lvert IFR_E \rvert$	$\lvert IFR_H \rvert$	$\lvert IFR_{CP} \rvert$	$w\lvert IFR_E \rvert$	$w\lvert IFR_H \rvert$	$w\lvert IFR_{CP} \rvert$
Square, Incident Wave #1	0.680	1.612	1.099	1.314	1.096	0.747	0.893
Square, Incident Wave #2	0.930	1.129	0.793	0.855	1.052	0.738	0.797
Circular, inscribed	0.680	1.397	0.761	0.998	0.950	0.517	0.679
Circular, equal cross-sect	0.766	1.362	0.777	0.994	1.044	0.595	0.762
Circular, equal circum.	0.846	1.336	0.794	1.000	1.129	0.671	0.845
Circular, circumscribed	0.931	1.312	0.805	1.000	1.221	0.749	0.931
Seamless Tube #1	0.777	1.358	0.780	0.998	1.056	0.606	0.776
Seamless Tube #2	0.802	1.350	0.785	0.998	1.082	0.629	0.800

Table IV-2. Comparison of Extinction Cross-Sections for Square Cylinder and Equivalent Circular Cylinders – Normal Incidence

	σ_E	σ_H	σ_{CP}
Square, Incident Wave #1	2. 047	1. 480	1. 764
Square, Incident Wave #2	1. 985	1. 197	1. 591
Circular, inscribed	1. 760	0. 940	1. 350
Circular, equal cross-sect	1. 950	1. 087	1. 519
Circular, equal circum.	2. 123	1. 247	1. 685
Circular, circumscribed	2. 309	1. 406	1. 858
Seamless Tube #1	1. 973	1. 116	1. 545
Seamless Tube #2	2. 027	1. 163	1. 595

Table IV-3. Comparison of IFR's for Square Cylinder and Equivalent Circular Cylinders— 62.5 deg Incidence

	Effective Width, w (wavelength)	$\lvert IFR_E \rvert$	$\lvert IFR_H \rvert$	$\lvert IFR_{CP} \rvert$	$w\lvert IFR_E \rvert$	$w\lvert IFR_H \rvert$	$w\lvert IFR_{CP} \rvert$
Square, Incident Wave #1	0.314	1.932	0.928	1.198	0.607	0.291	0.376
Square, Incident Wave #2	0.430	1.400	0.821	0.868	0.602	0.261	0.373
Circular, inscribed	0.314	1.731	0.640	1.019	0.544	0.201	0.320
Circular, equal cross-sect	0.354	1.665	0.652	1.010	0.589	0.231	0.357
Circular, equal circum.	0.391	1.615	0.664	1.003	0.631	0.259	0.392
Circular, circumscribed	0.430	1.570	0.680	0.997	0.675	0.293	0.429
Seamless Tube #1	0.359	1.658	0.654	1.009	0.595	0.235	0.362
Seamless Tube #2	0.370	1.642	0.657	1.007	0.608	0.243	0.372

Table IV-4. Comparison of Extinction Cross-Sections for Square Cylinder and Equivalent Circular Cylinders — 62.5 deg Incidence

	σ_E	σ_H	σ_{CP}
Square, Incident Wave #1	1.061	0.430	0.746
Square, Incident Wave #2	1.049	0.418	0.734
Circular, inscribed	0.930	0.312	0.621
Circular, equal cross-sect.	1.024	0.372	0.698
Circular, equal circum.	1.109	0.427	0.768
Circular, circumscribed	1.199	0.490	0.844
Seamless Tube #1	1.035	0.380	0.707
Seamless Tube #2	1.061	0.396	0.729

Table IV-5. Comparison of Scattering Characteristics of Single Square Cylinder and Array of Four Square Cylinders

	Single Cylinder	4X Single Cylinder	4-Cylinder Array	Single Cylinder	4X Single Cylinder	4-Cylinder Array
$W\|IFR_E\|$	1.096	4.384	4.177	0.607	2.428	2.176
$W\|IFR_H\|$	0.747	2.988	2.922	0.291	1.164	1.033
$W\|IFR_{CP}\|$	0.893	3.572	3.457	0.376	1.504	1.402
σ_E	2.047	8.188	7.405	1.061	4.244	3.996
σ_H	1.480	5.920	5.842	0.430	1.720	1.598
σ_{CP}	1.764	7.056	6.624	0.746	2.984	2.797
	Normal Incidence			62.5-Degree Incidence		

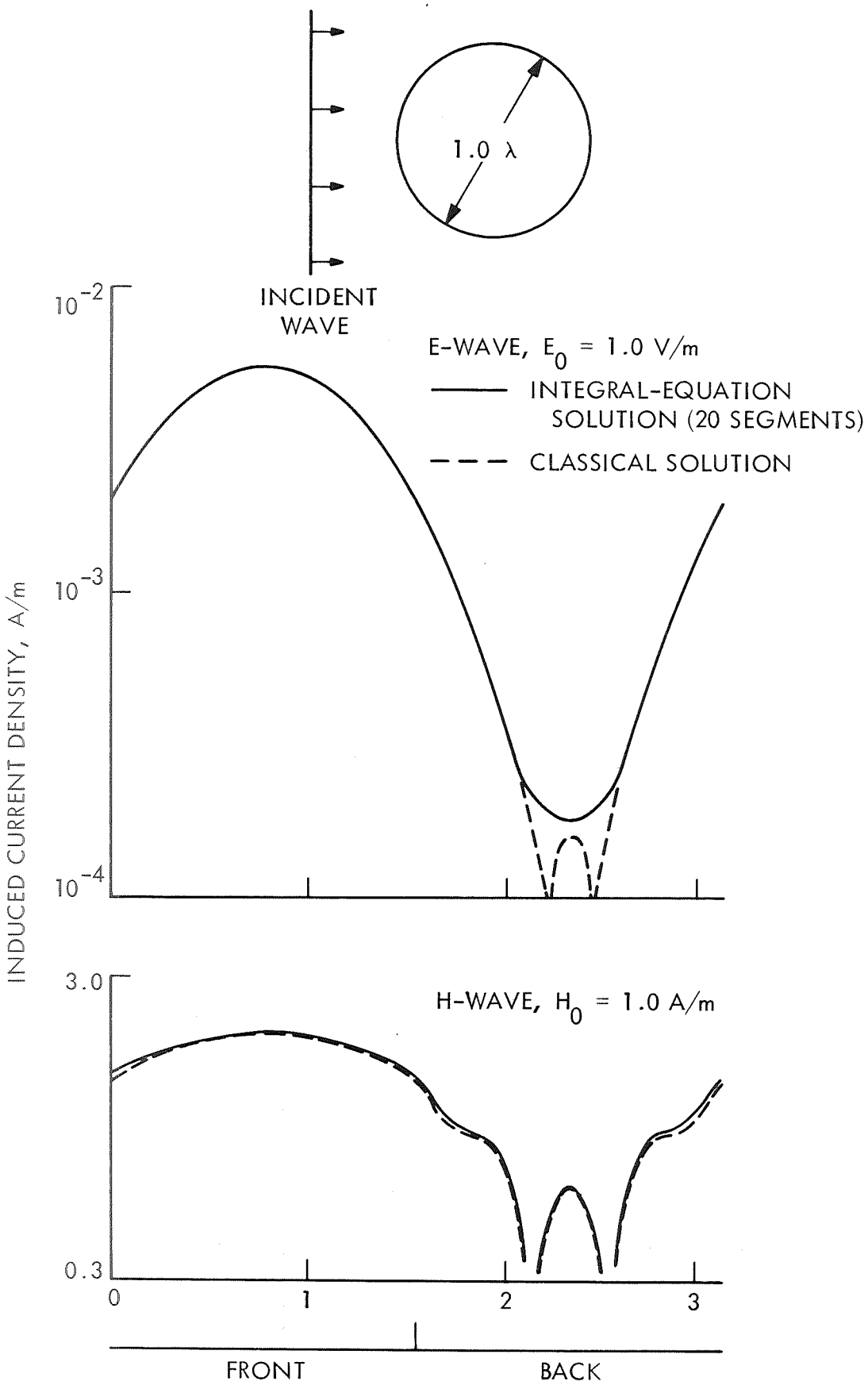

Fig. IV-1. Comparison of Induced Current Density on 1-Wavelength-diameter, Right-Circular Cylinder from Integral Equation with Classical Solution

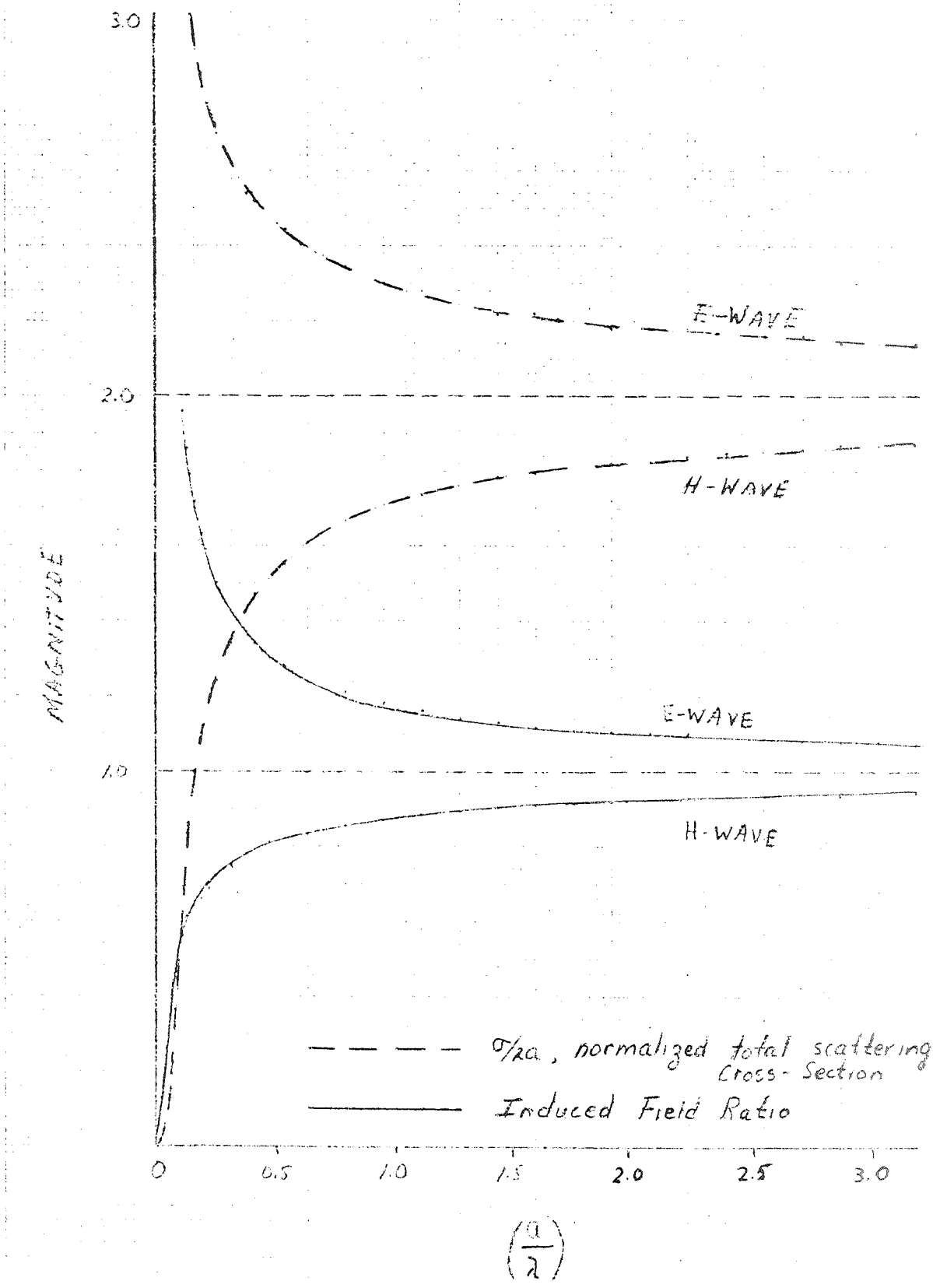

Fig. IV-2. Classical Results for Normalized Total Scattering Cross-section and Induced Field Ratio of Right-Circular Cylinder

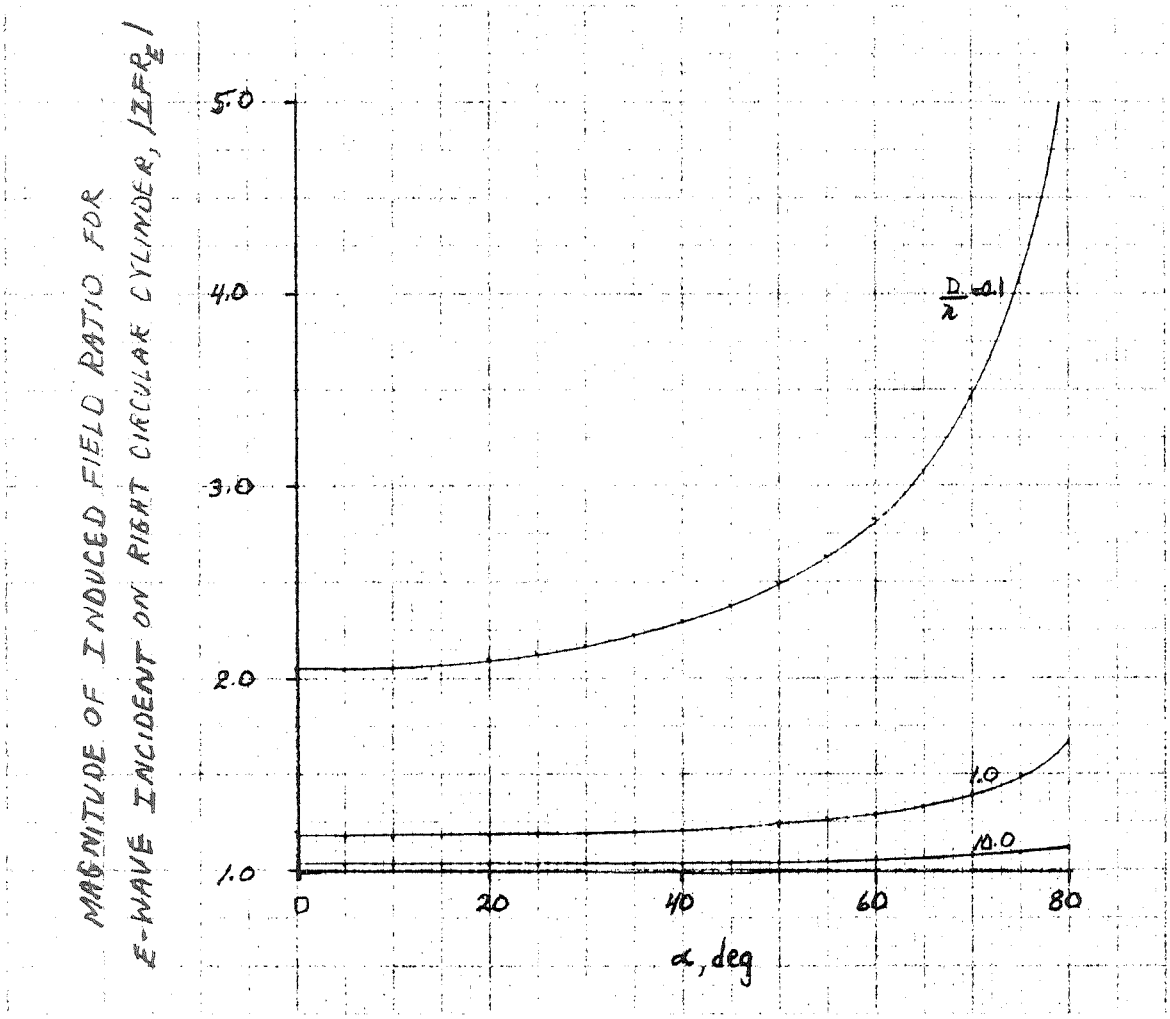

Fig. IV-3. Classical Results for E-Wave Induced Field Ratio versus Angle of Incidence

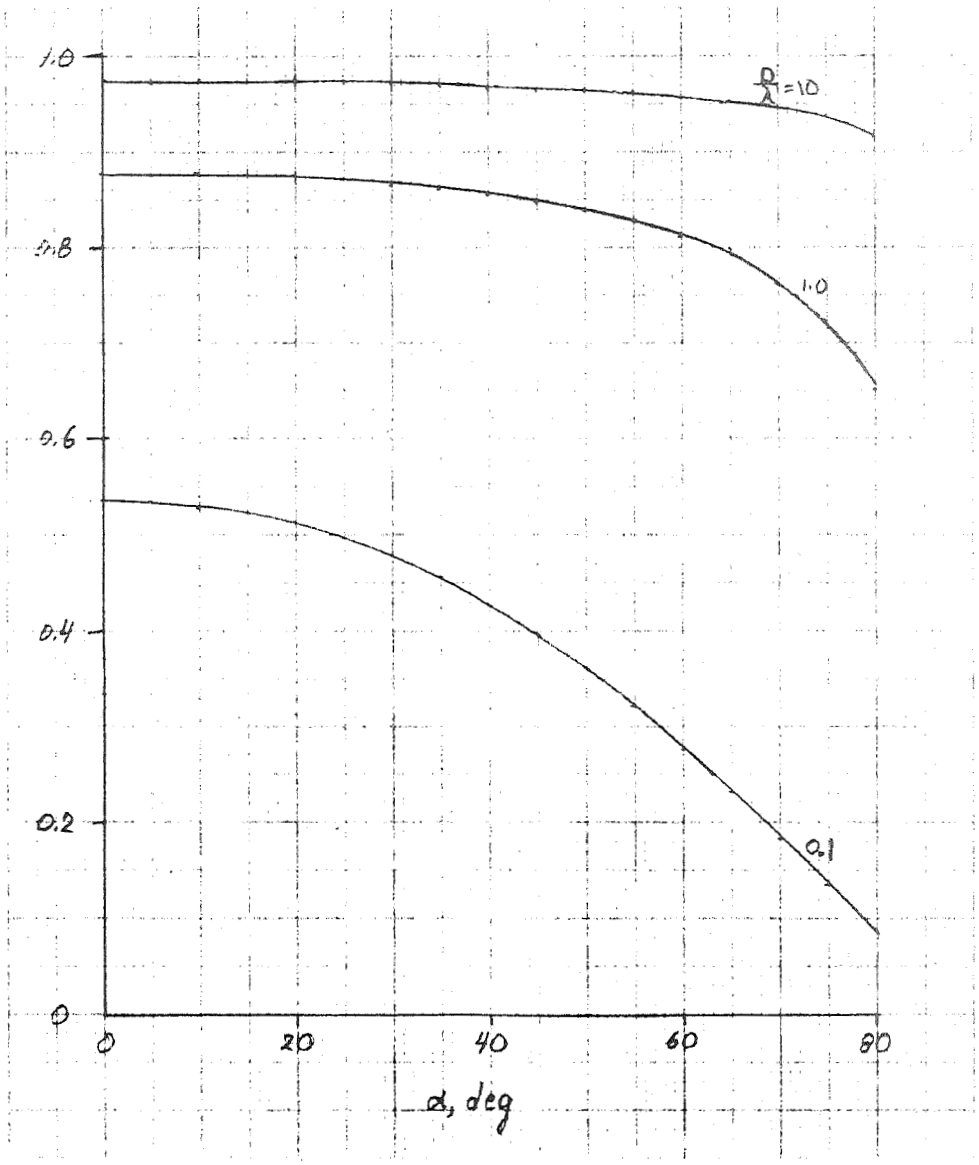

Fig. IV-4. Classical Results for H-Wave Induced Field Ratio versus Angle of Incidence

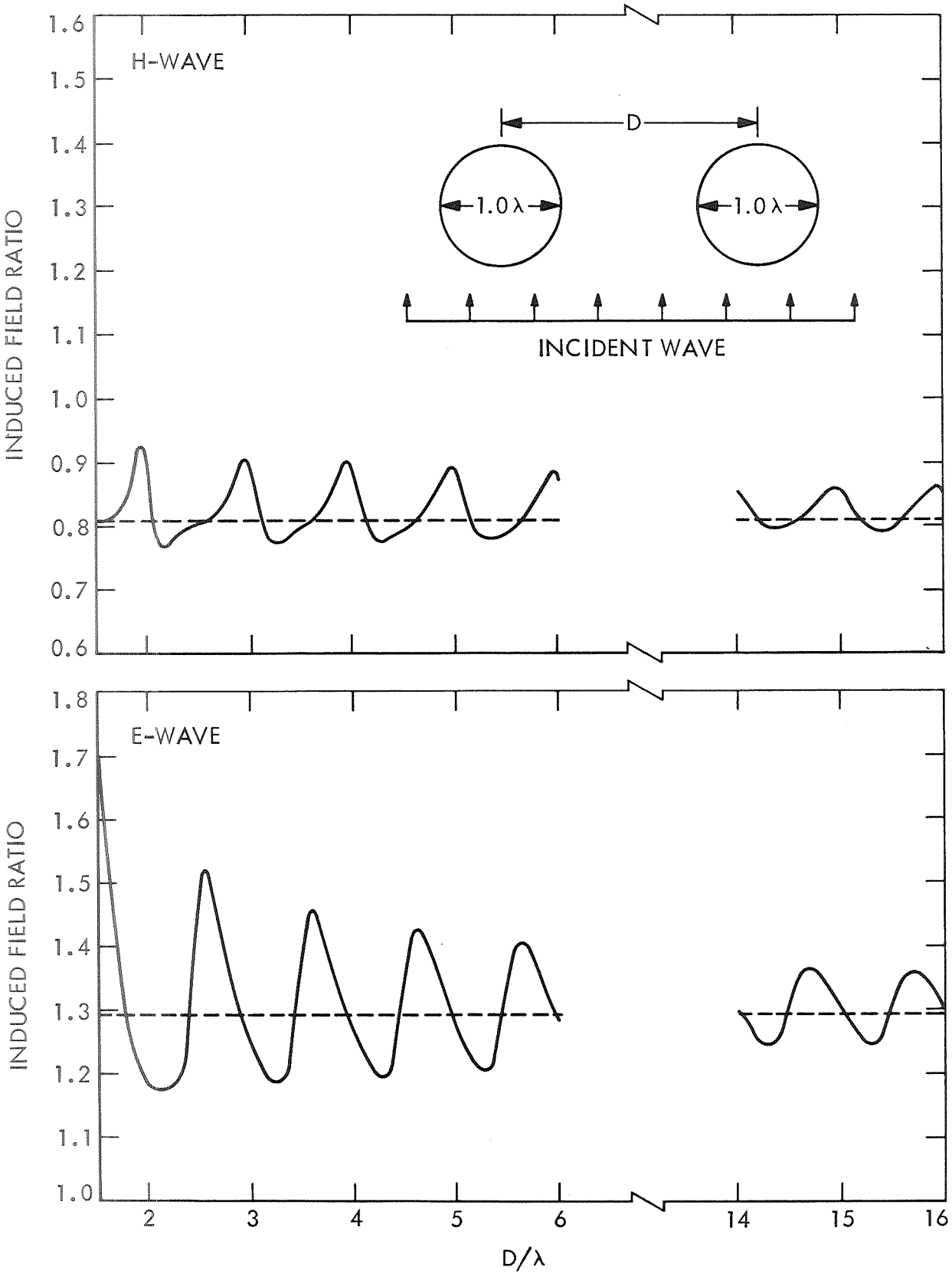

Fig. IV-5. Induced Field Ratio of Two Right-Circular Cylinders versus Transverse Separation

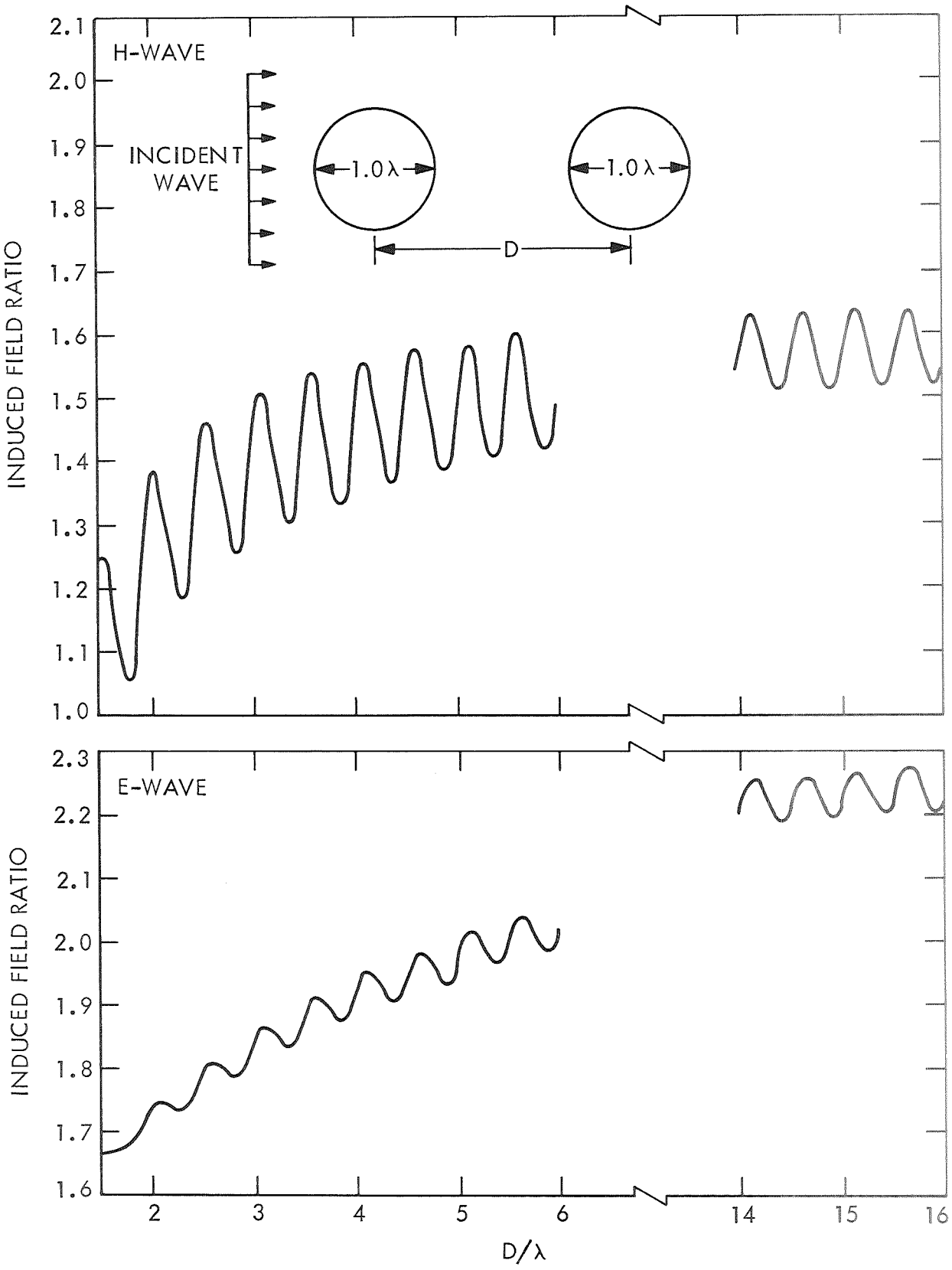

Fig. IV-6. Induced Field Ratio of Two Right-Circular Cylinders versus Longitudinal Separation

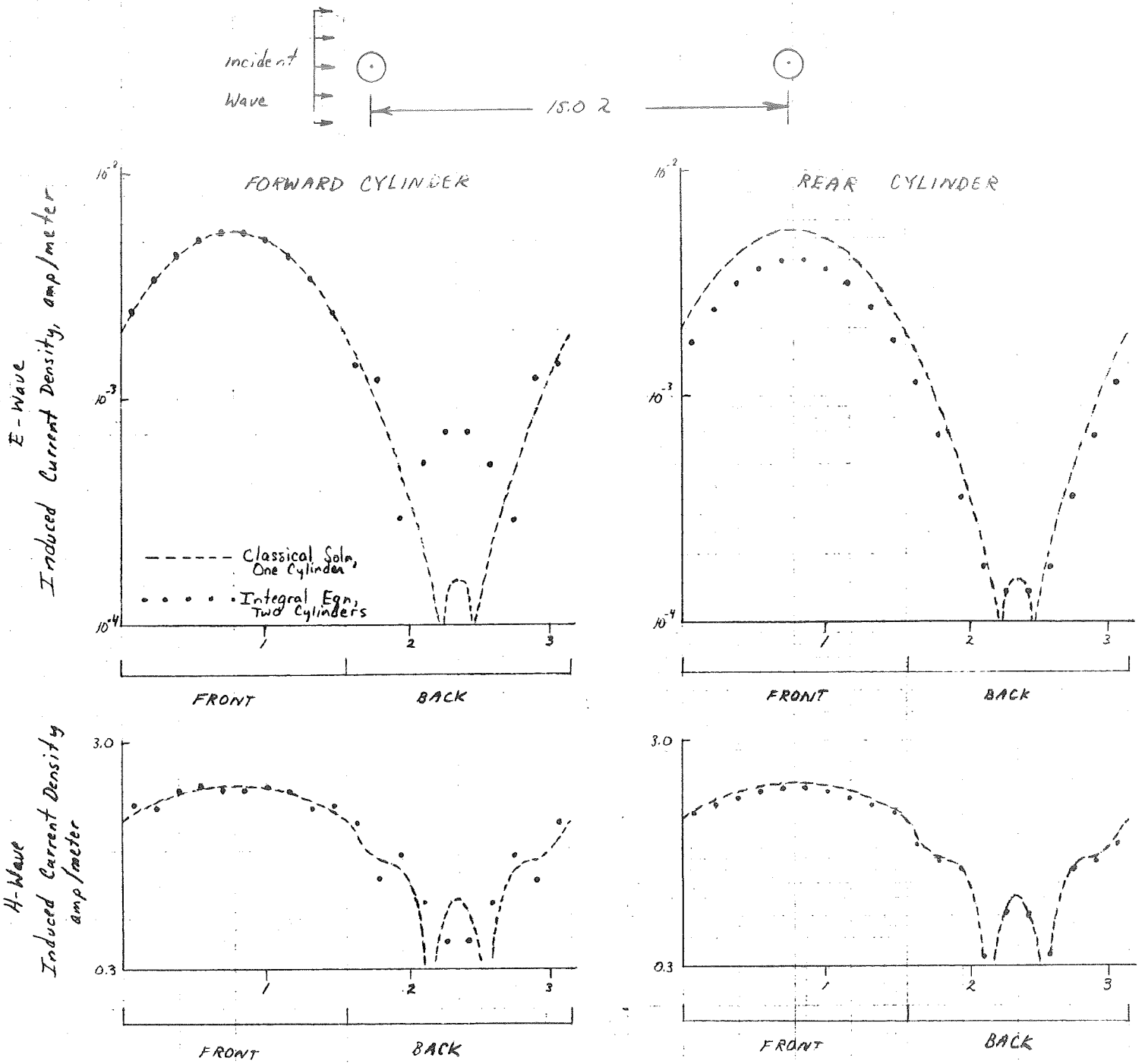

Fig. IV-7. Currents Induced on Two Right-Circular Cylinders with 15-Wavelength Longitudinal Separation

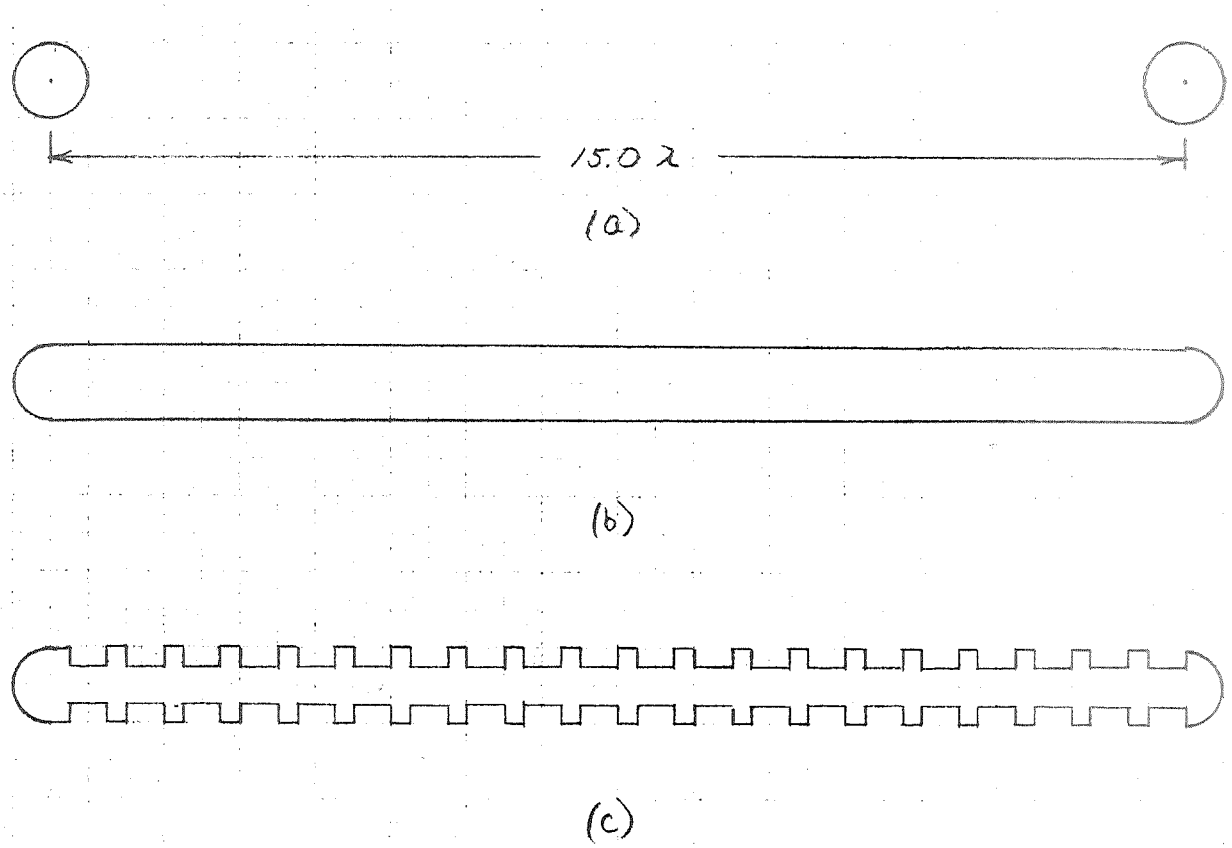

Fig. IV-8. Geometry of Elongated Cylinder

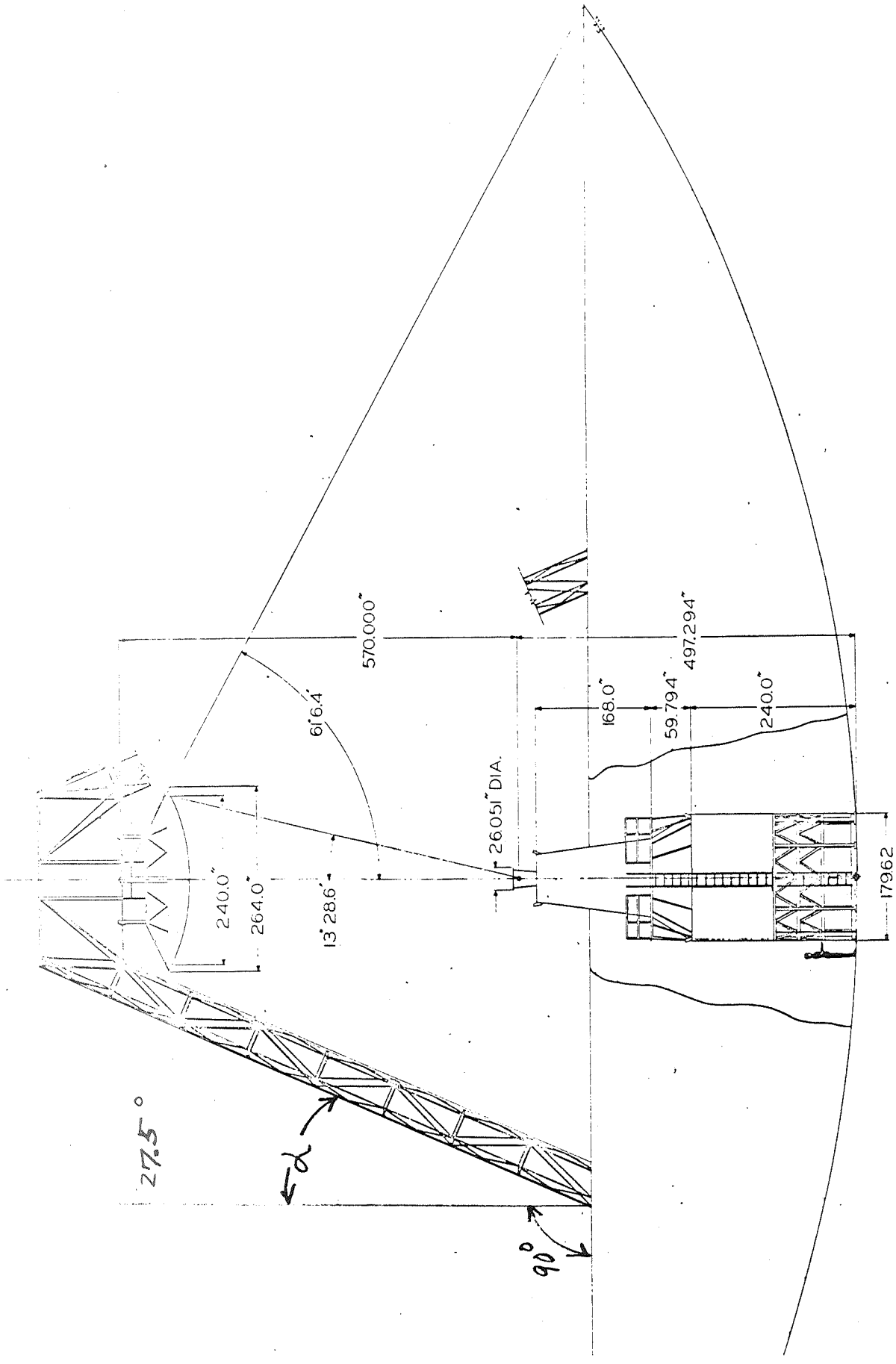

Fig. IV-9. Geometry of AAS Feed System Support Structure

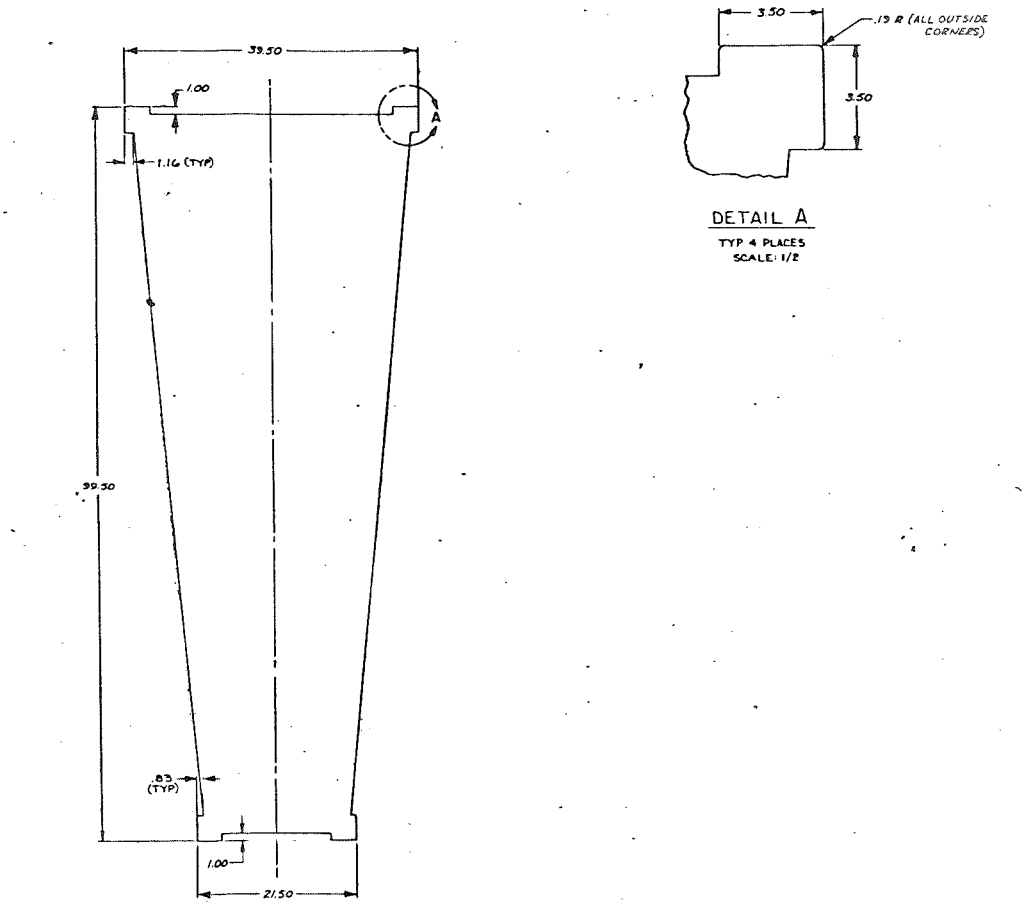

Fig. IV-10. Geometry of Cross Section of AAS Tetrapod Leg

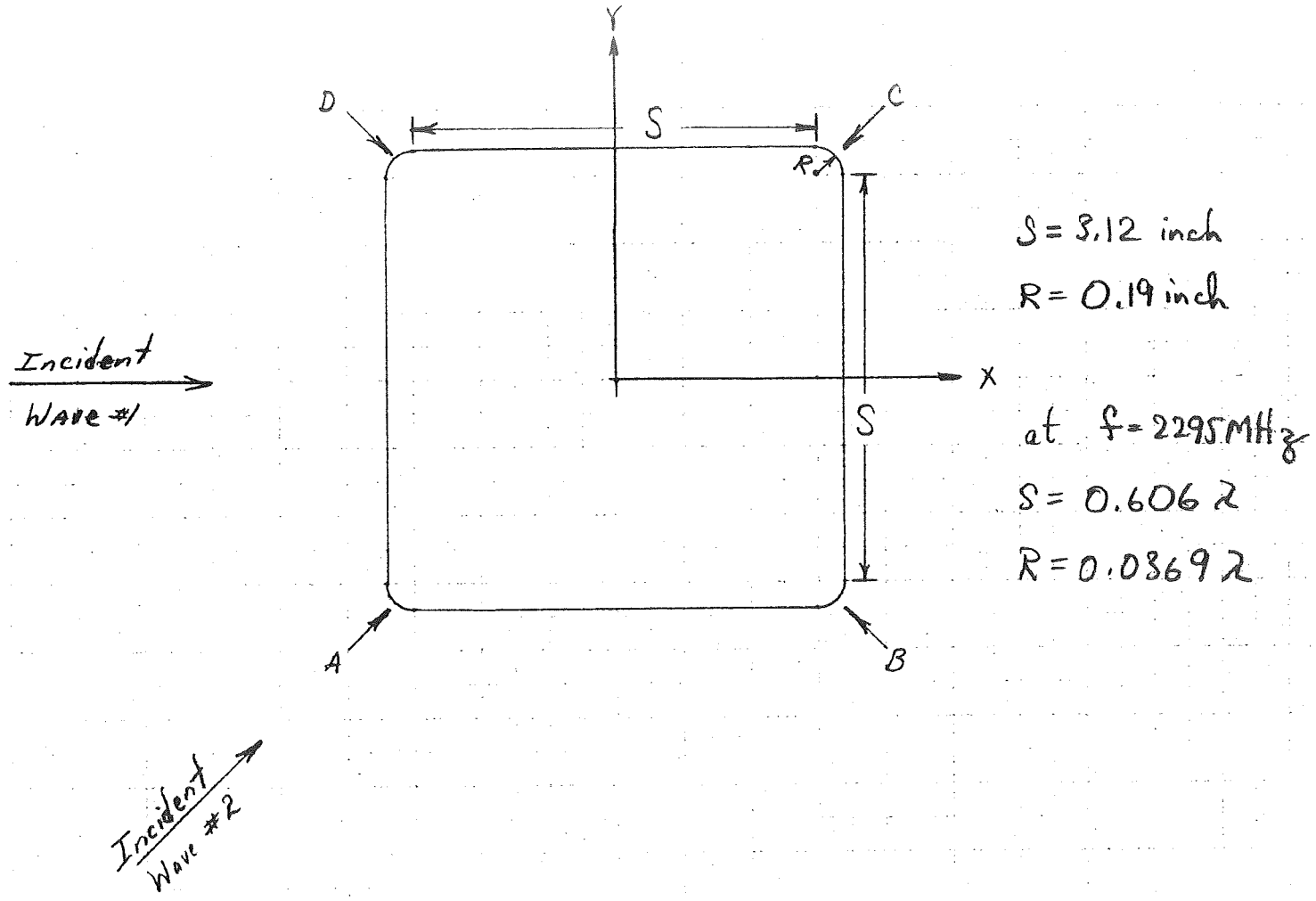

Fig. IV-11. Geometry of Plane Wave Incident on Square Cylinder

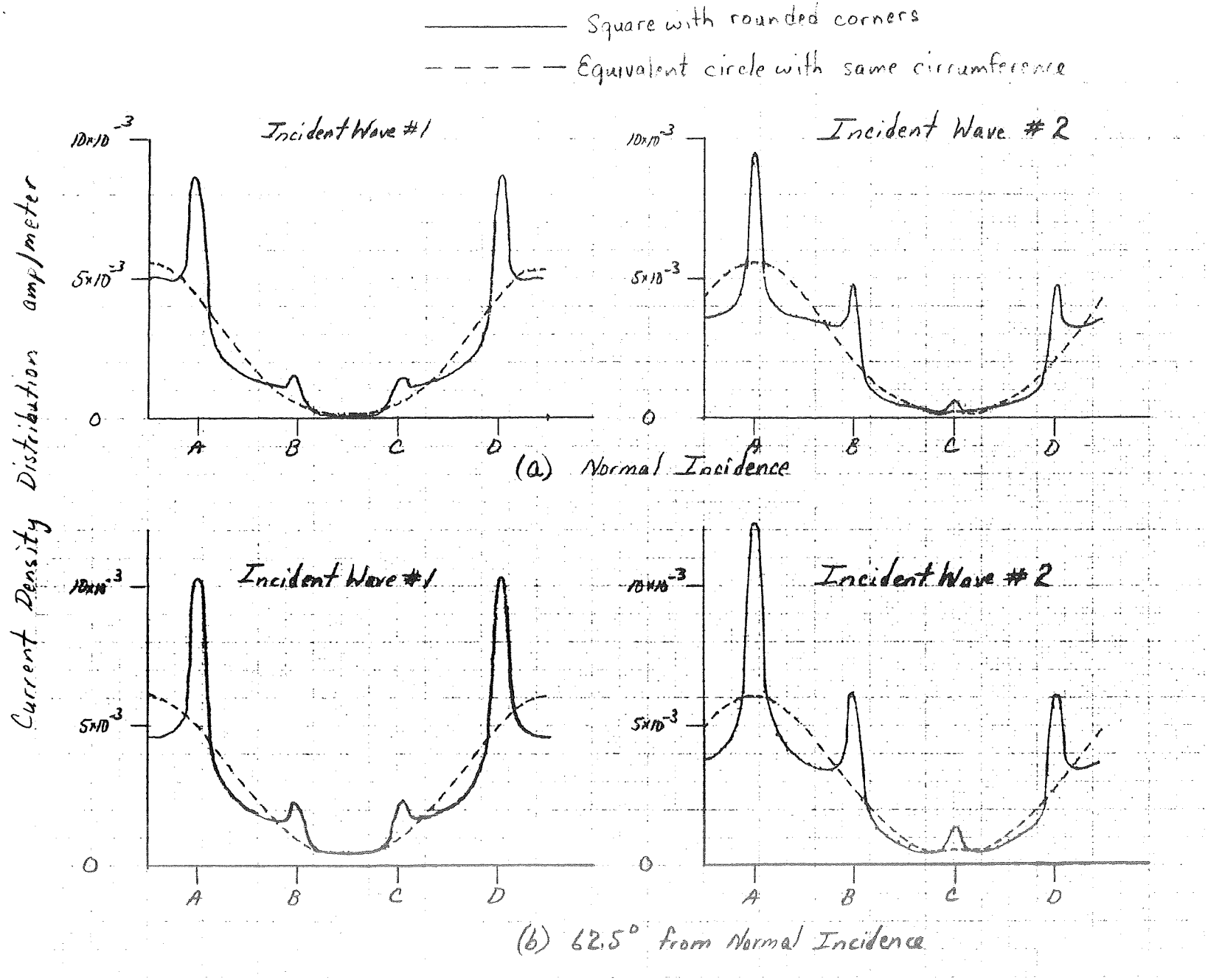

Fig. IV-12. Current Density Induced on Square Cylinder by Incident E-Wave

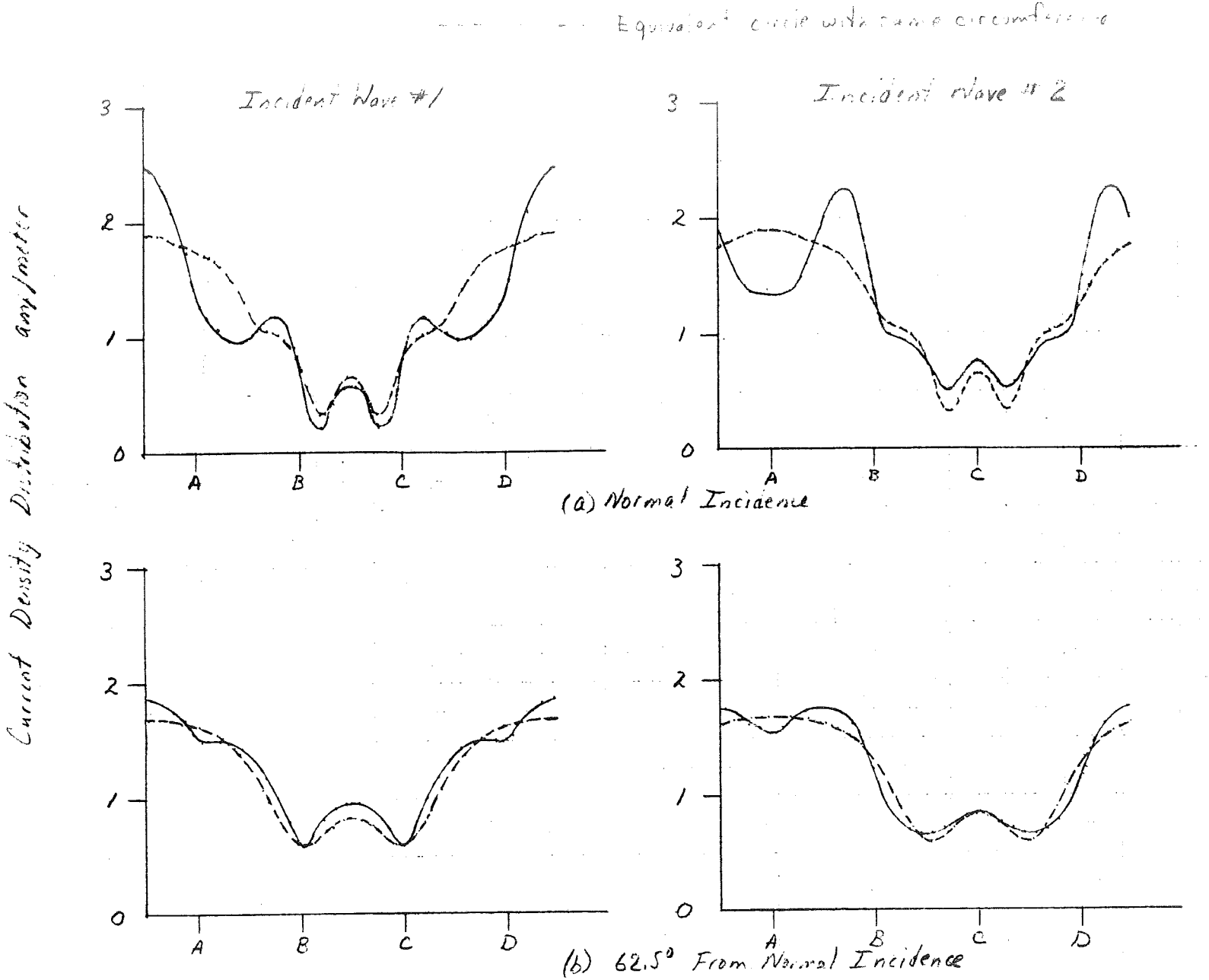

Fig. IV-13. Current Density Induced on Square Cylinder by Incident H-Wave

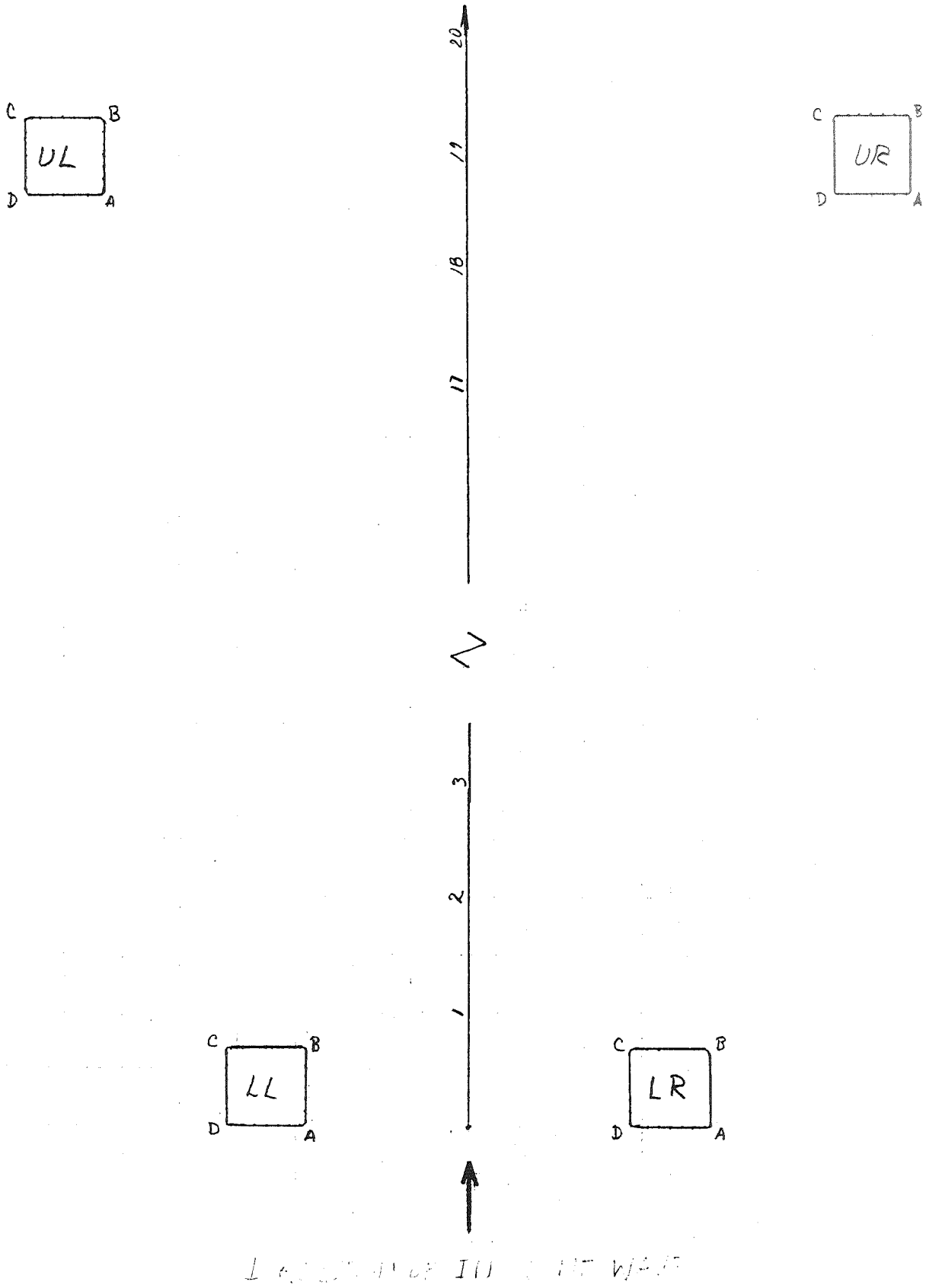

Fig. IV-14. Geometry of Array of Four Square Cylinders

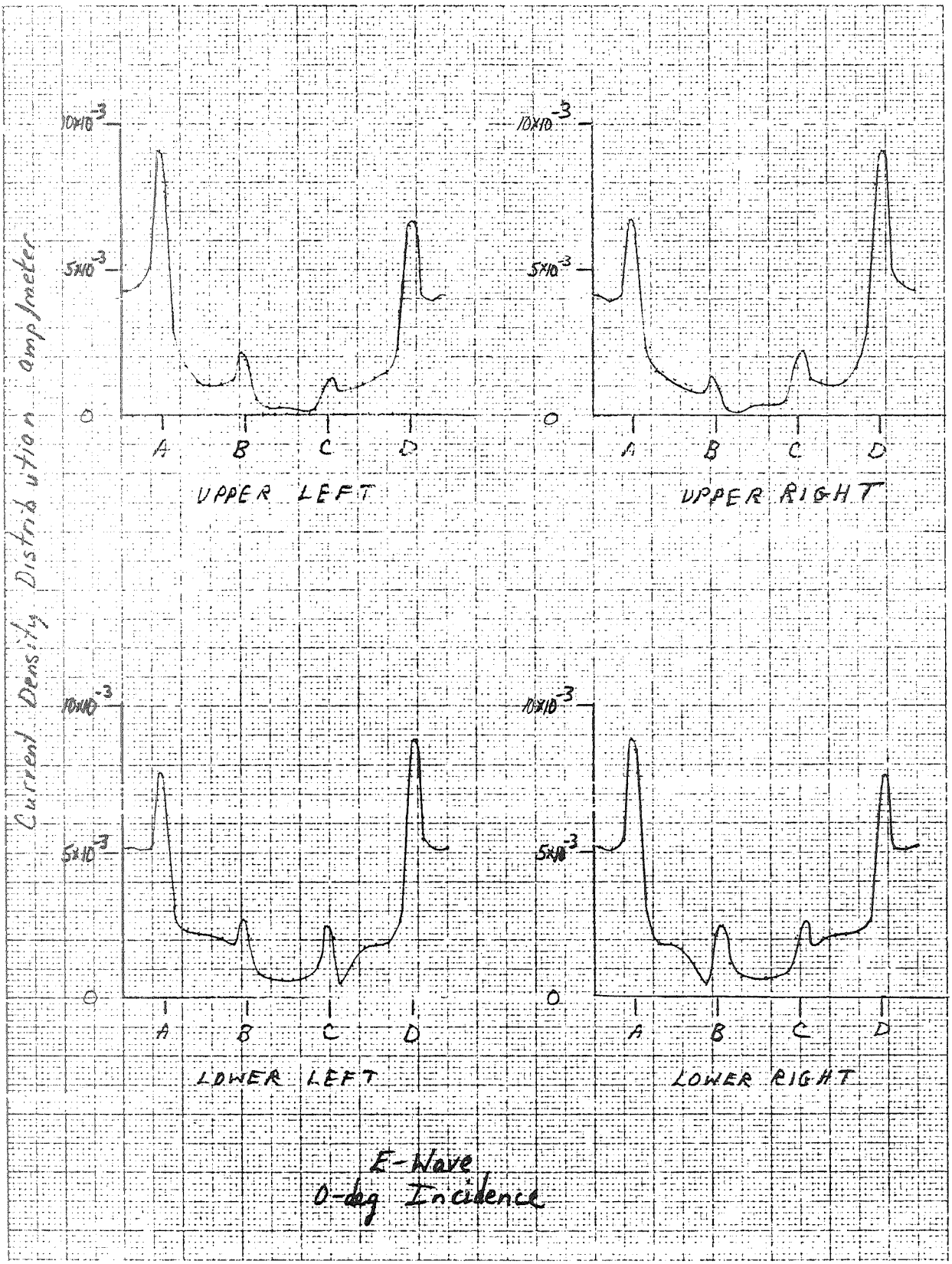

Fig. IV-15. Current Densities Induced on Four Square Cylinders by E-Wave (Normal Incidence)

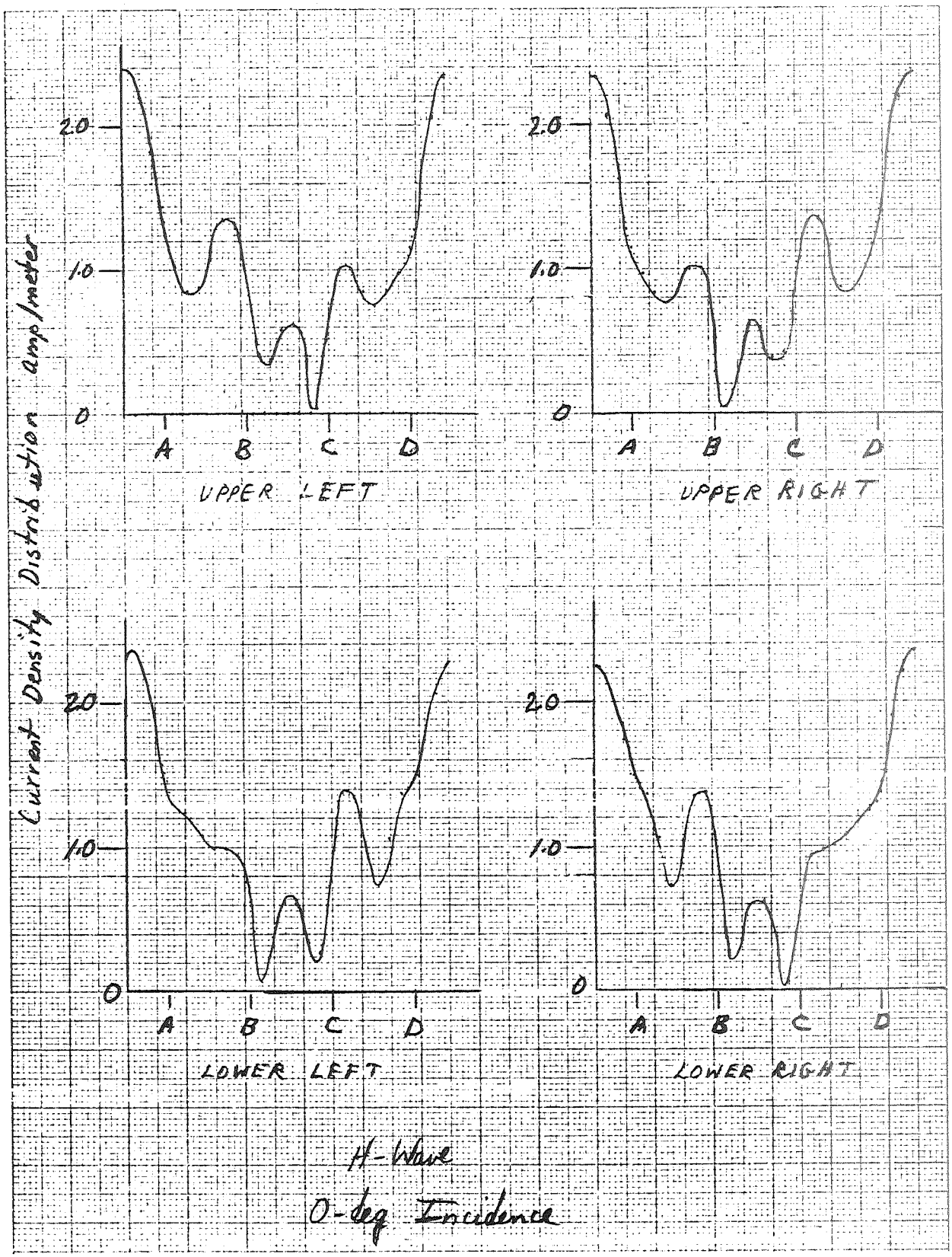

Fig. IV-16. Current Density Induced on Four Square Cylinders by H-Wave (Normal Incidence)

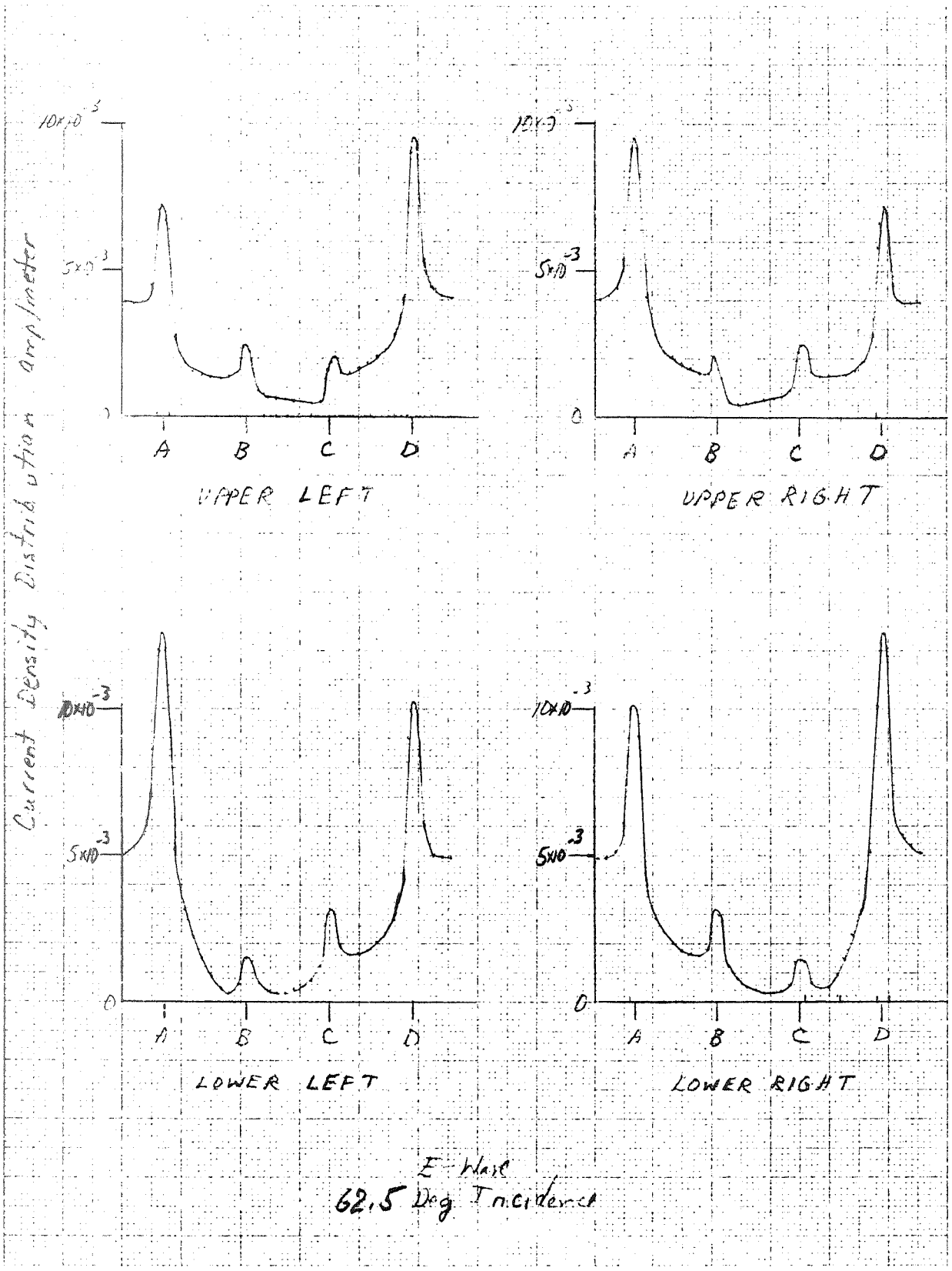

Fig. IV-17. Current Density Induced on Four Square Cylinders by E-Wave (62.5-deg Incidence)

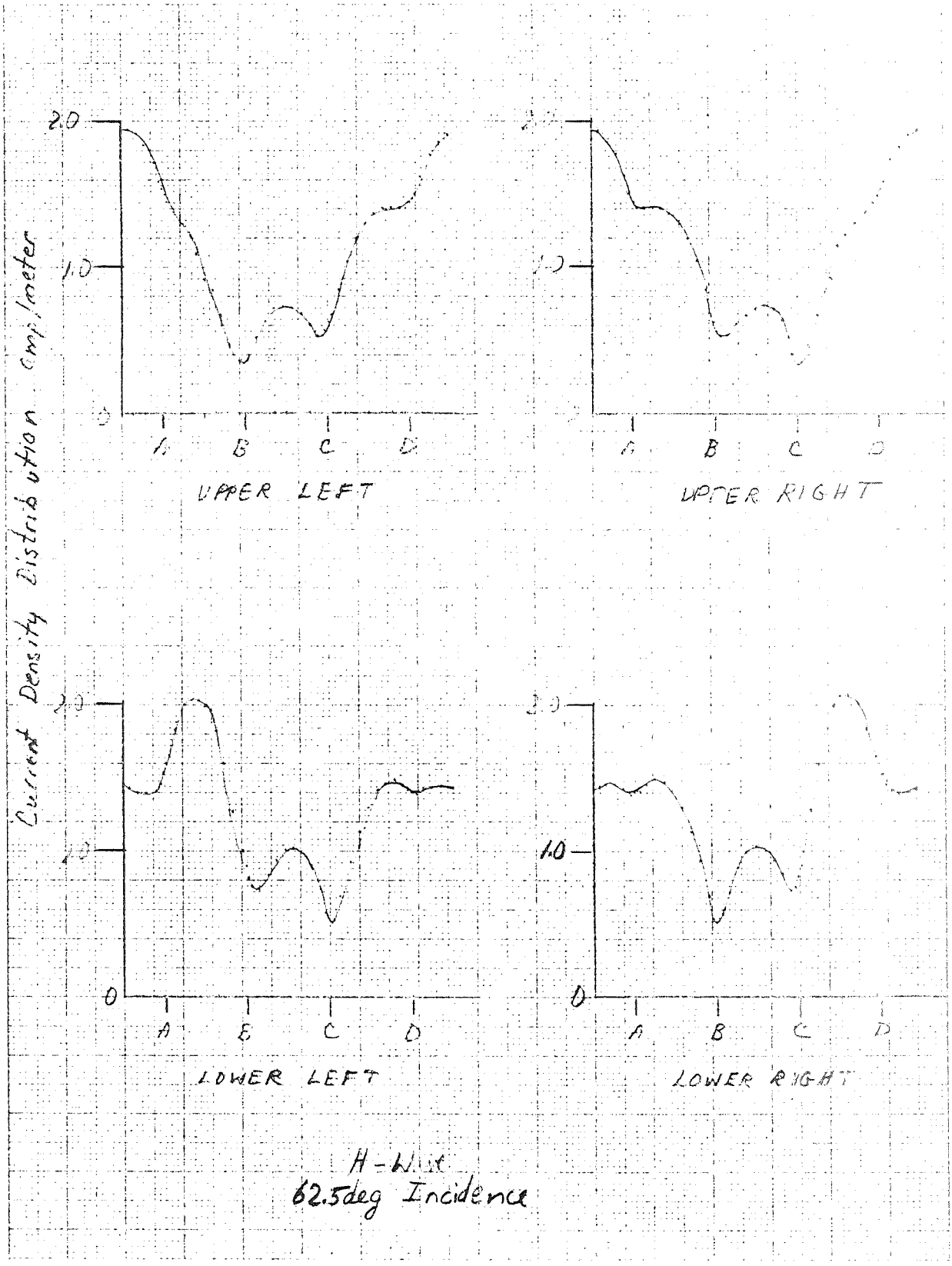

Fig. IV-18. Current Density Induced on Four Square Cylinders by H-Wave (62.5-deg Incidence)

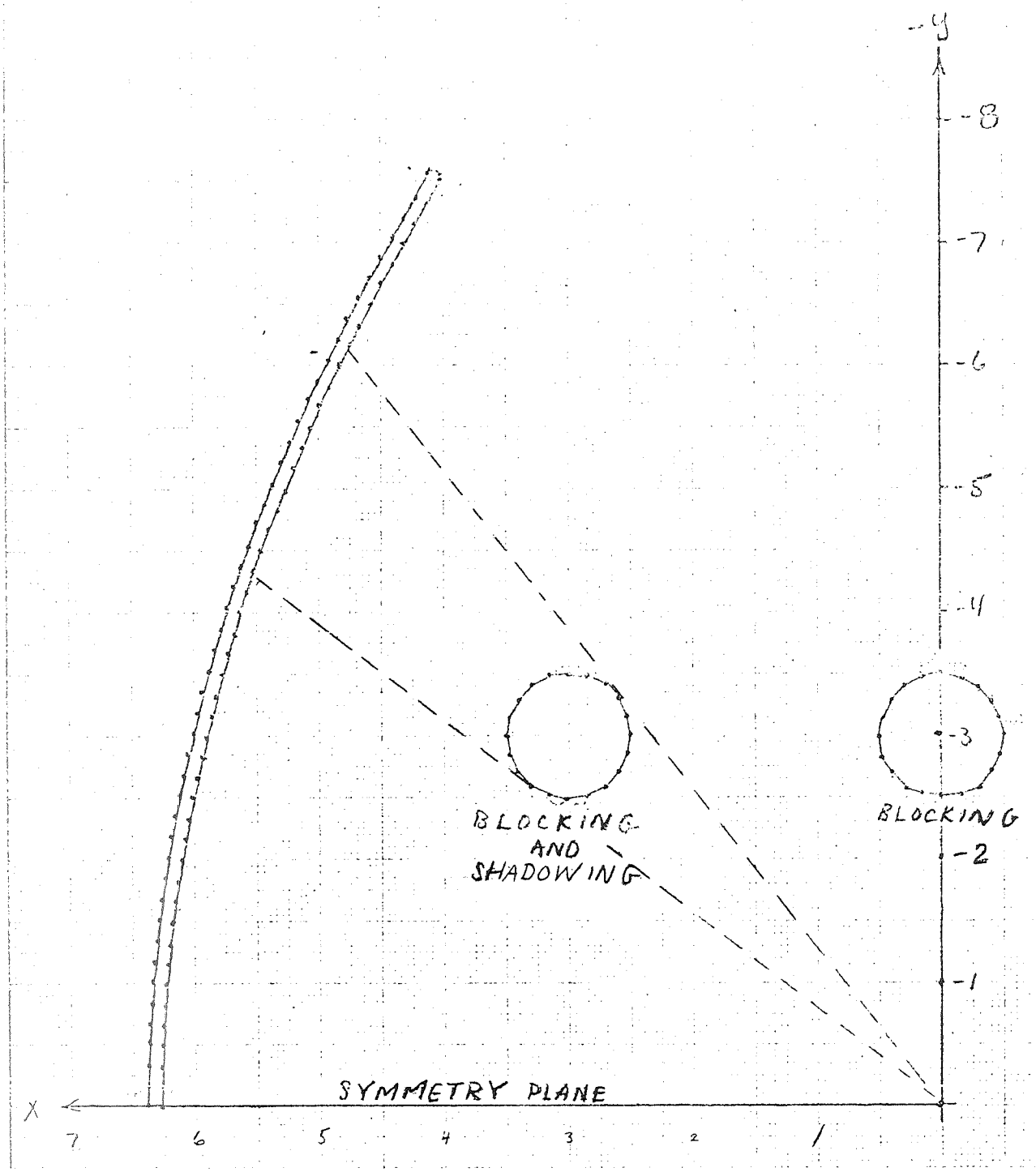

Fig. IV-19. Geometry of Blocked and Shadowed Cylindrical Parabola Reflector

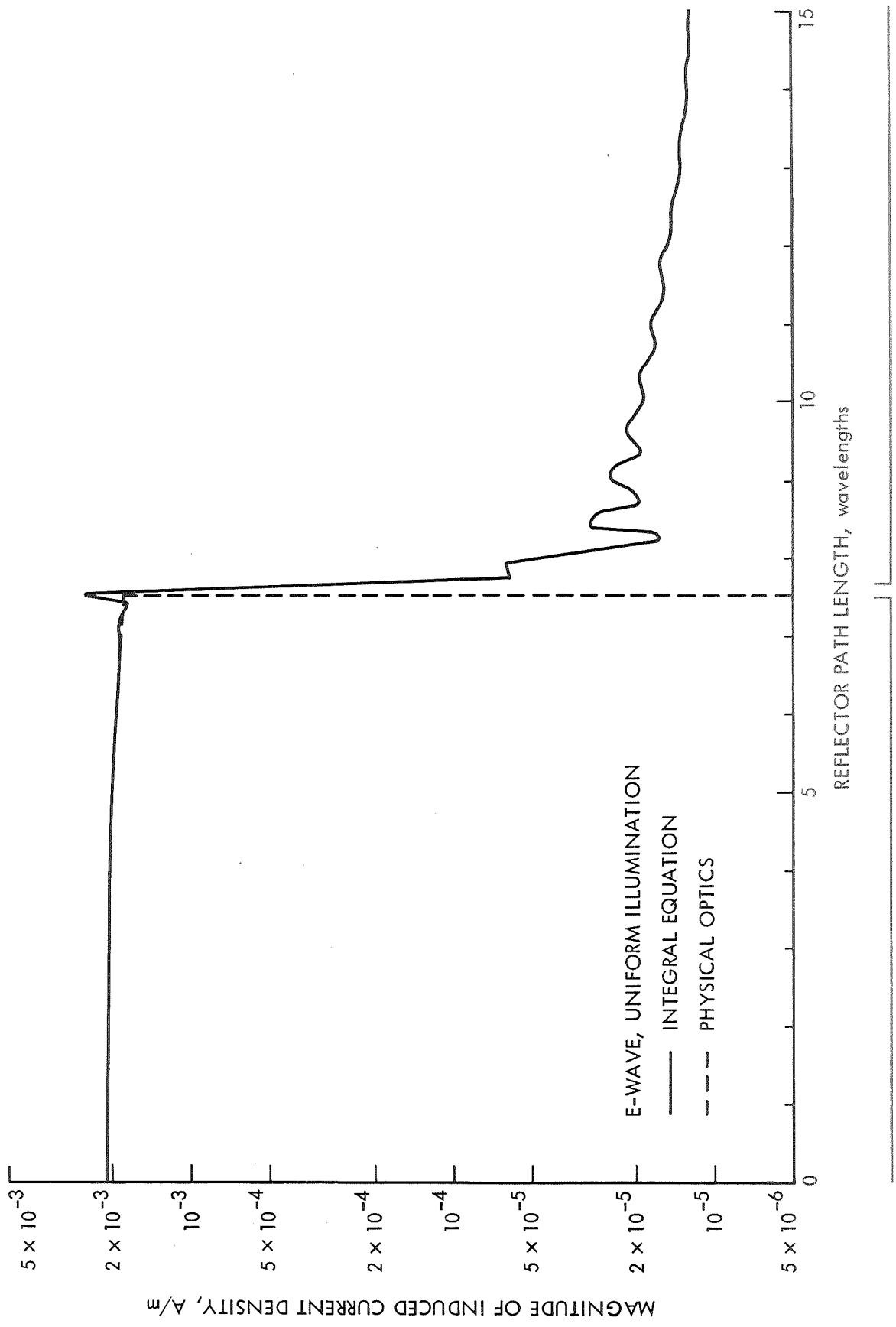

Fig. IV-20. Current Induced on Unblocked Reflector by Feed with Parallel Polarization

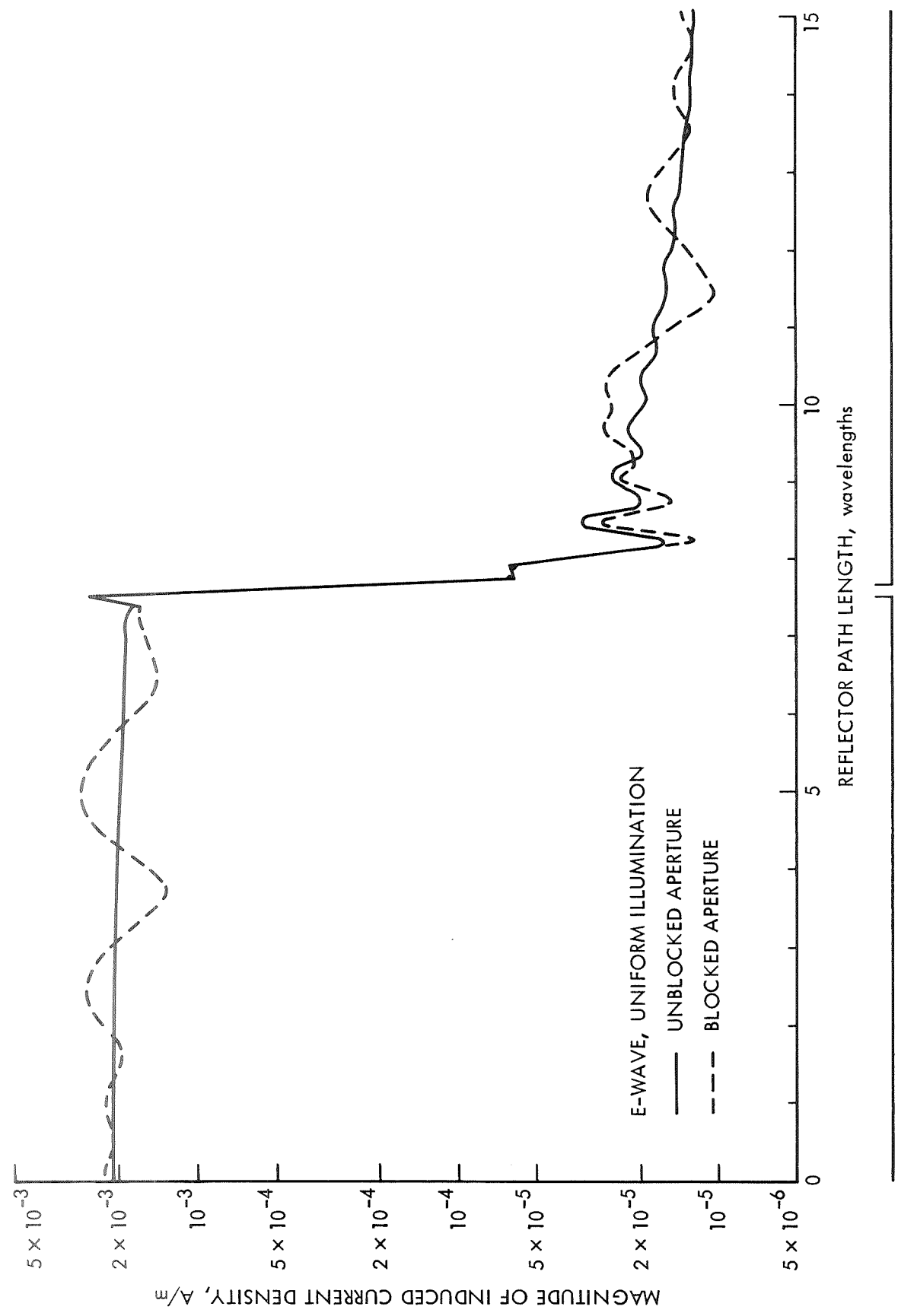

Fig. IV-21. Current Induced on Blocked Reflector by Feed with Parallel Polarization

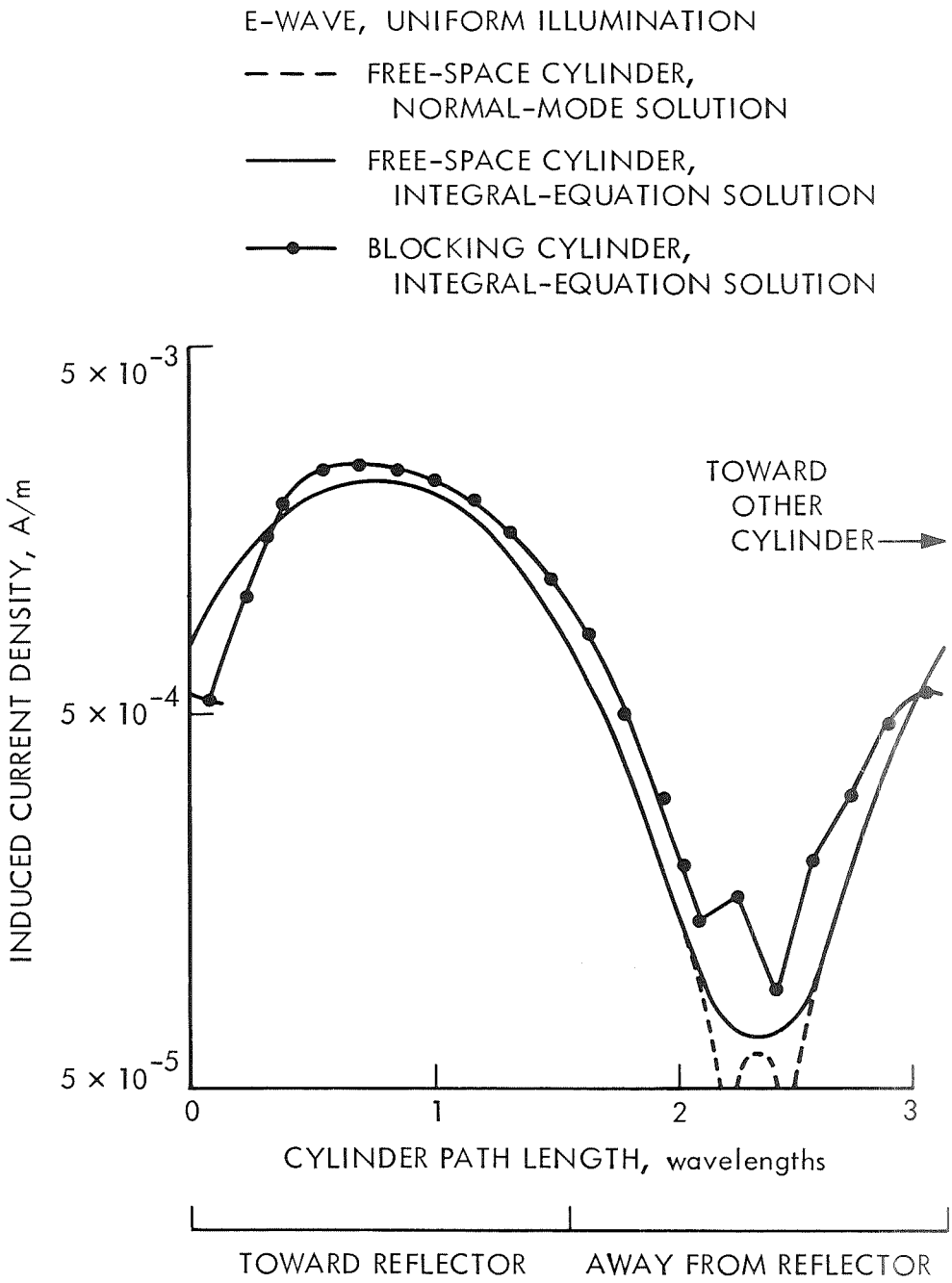

Fig. IV-22. Comparison of Currents Induced on Blocking Cylinder by Parallel Polarization

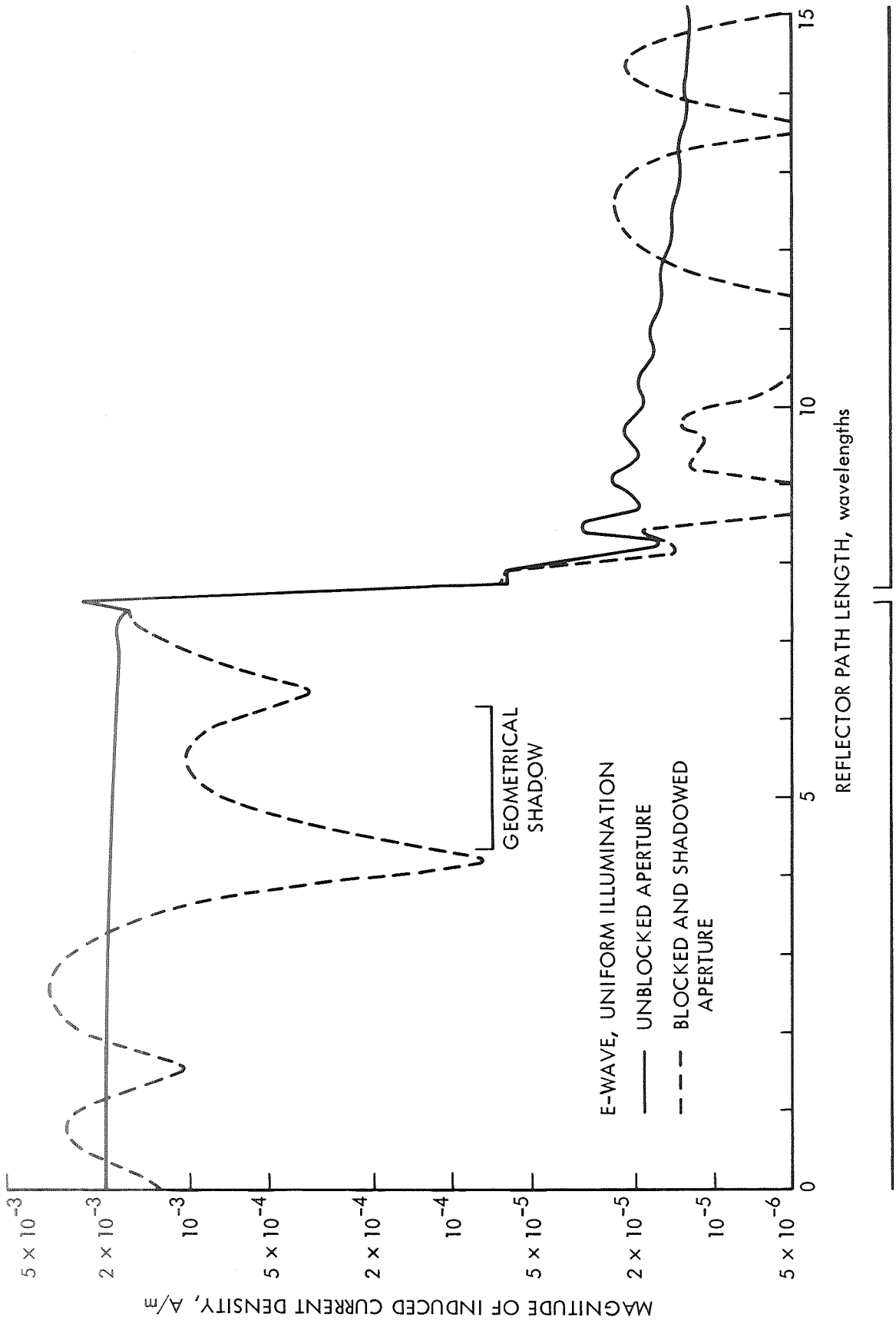

Fig. IV-23. Current Induced on Blocked and Shadowed Cylinder by Parallel Polarization

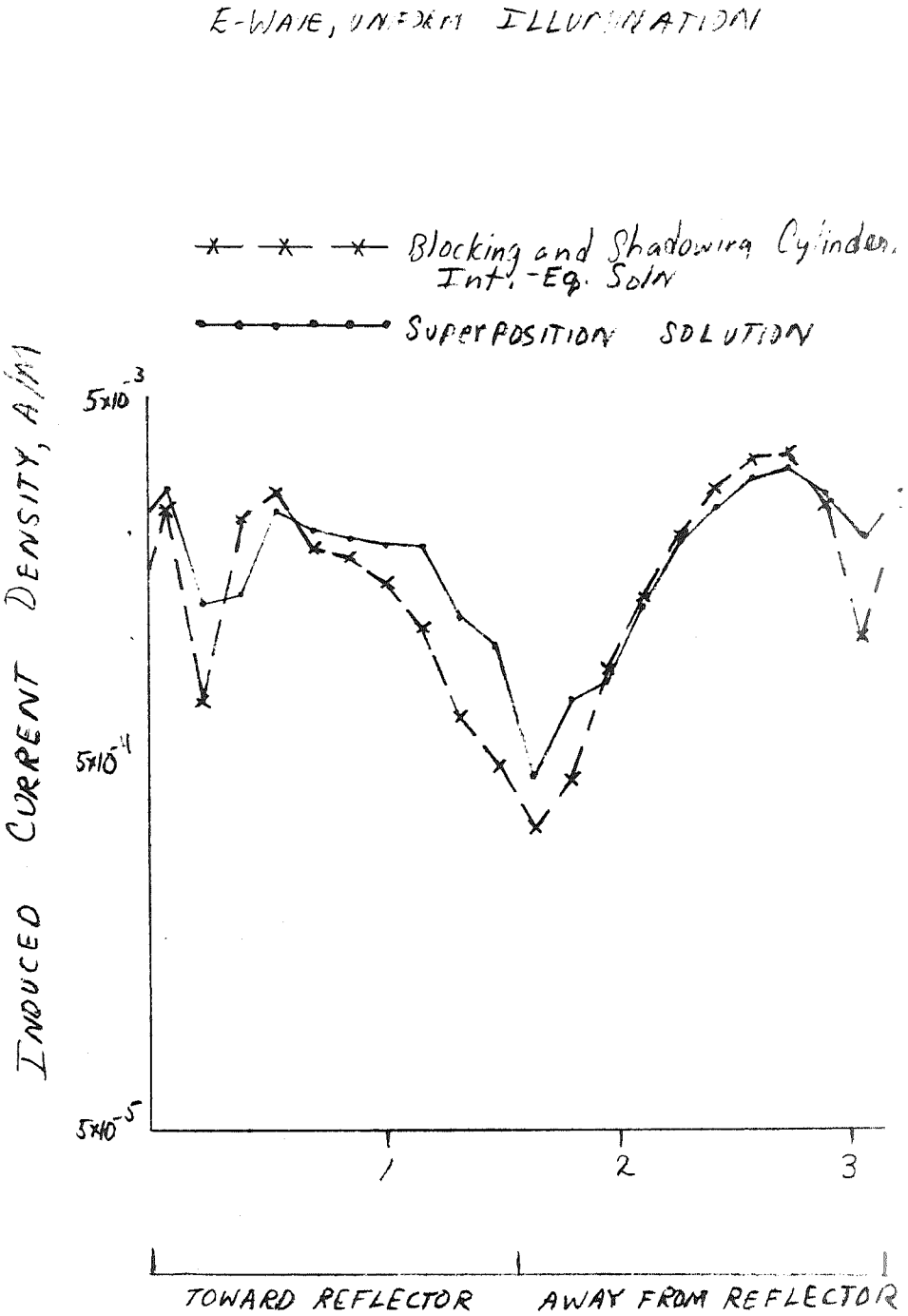

Fig. IV-24. Comparison of Currents Induced on Blocking and Shadowing Cylinder by Parallel Polarization

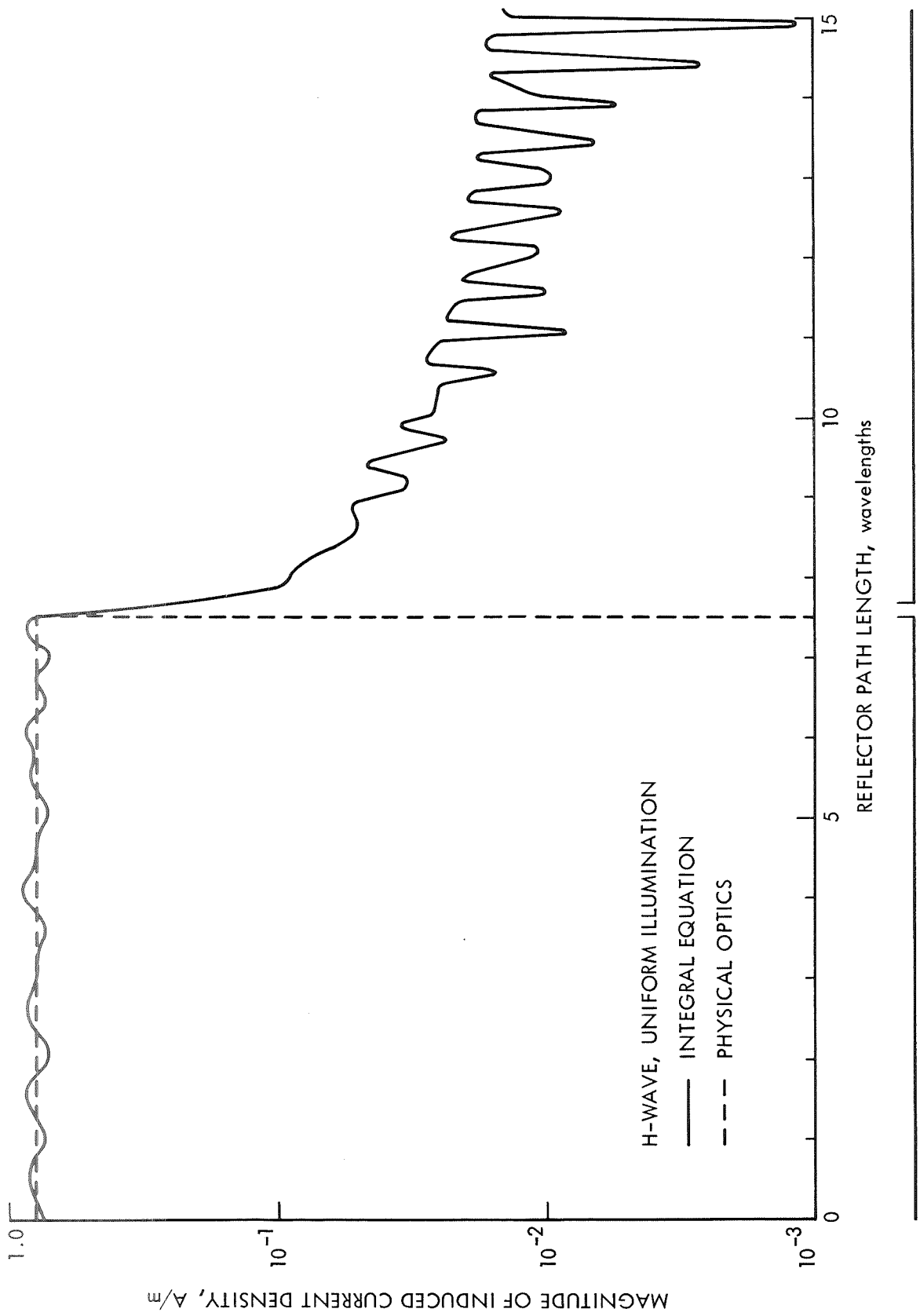

Fig. IV-25. Current Induced on Unblocked Reflector by Feed with Perpendicular Polarization

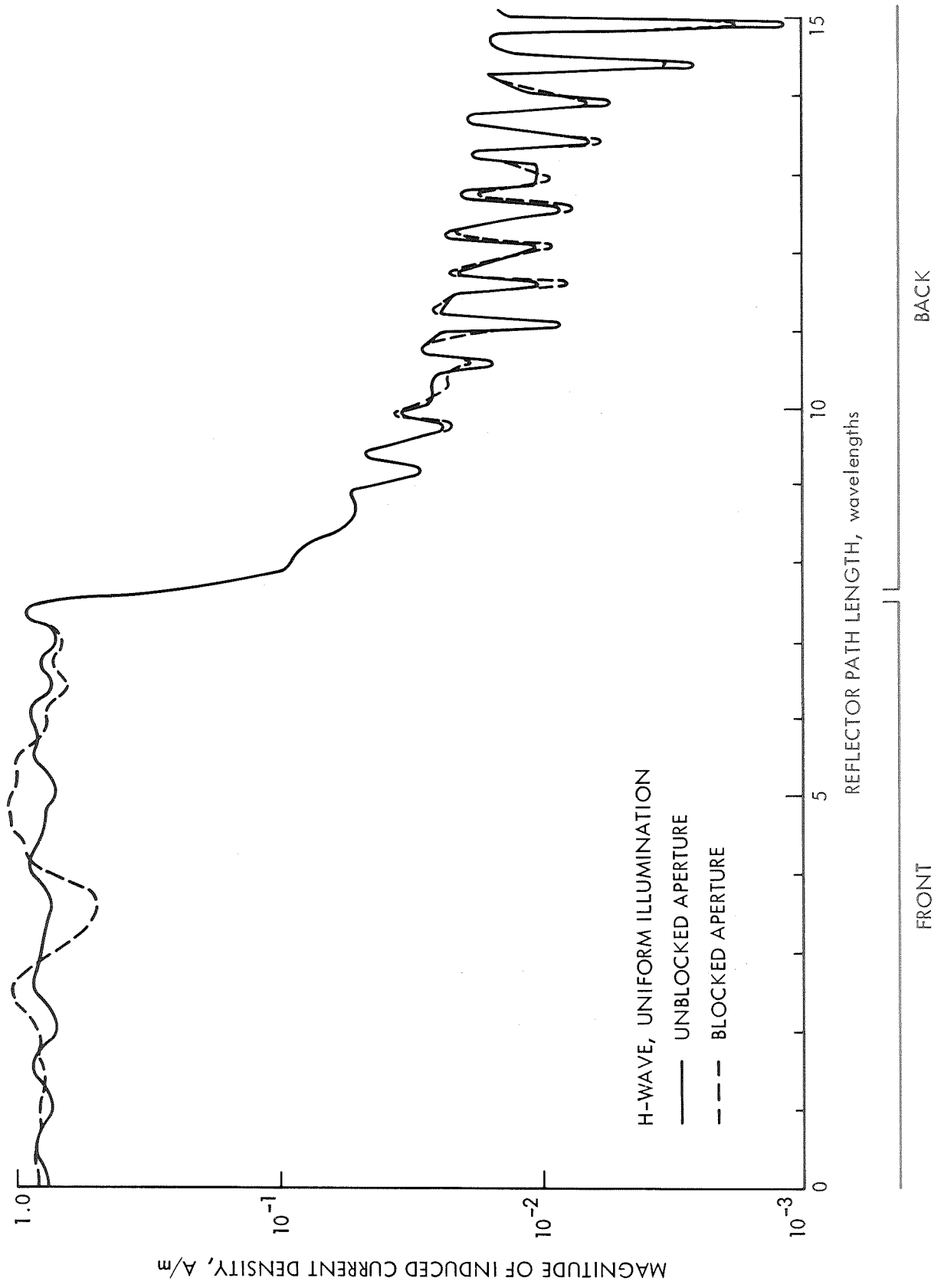

Fig. IV-26. Current Induced on Blocked Reflector by Feed with Perpendicular Polarization

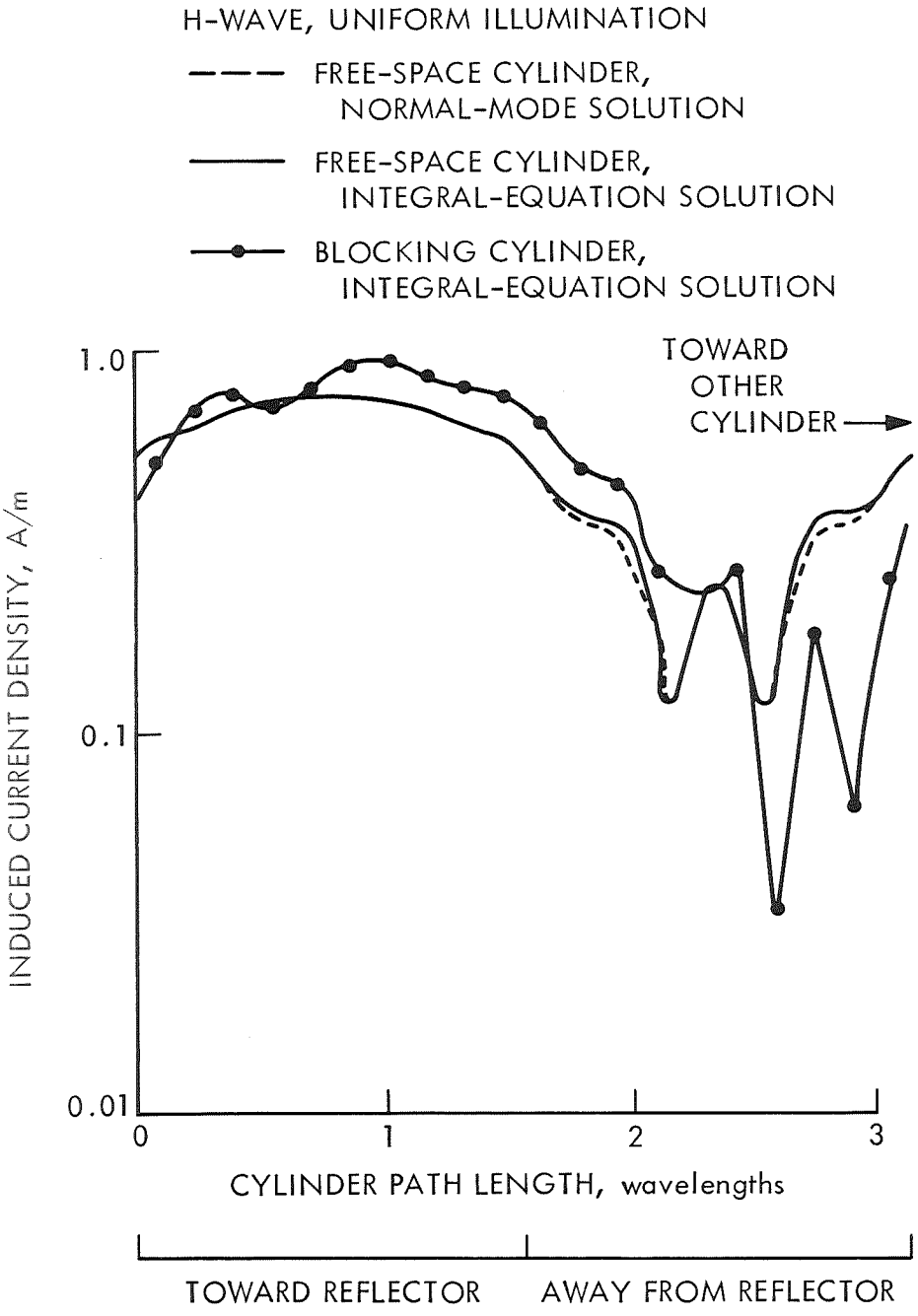

Fig. IV-27. Comparison of Currents Induced on Blocking Cylinder by Perpendicular Polarization

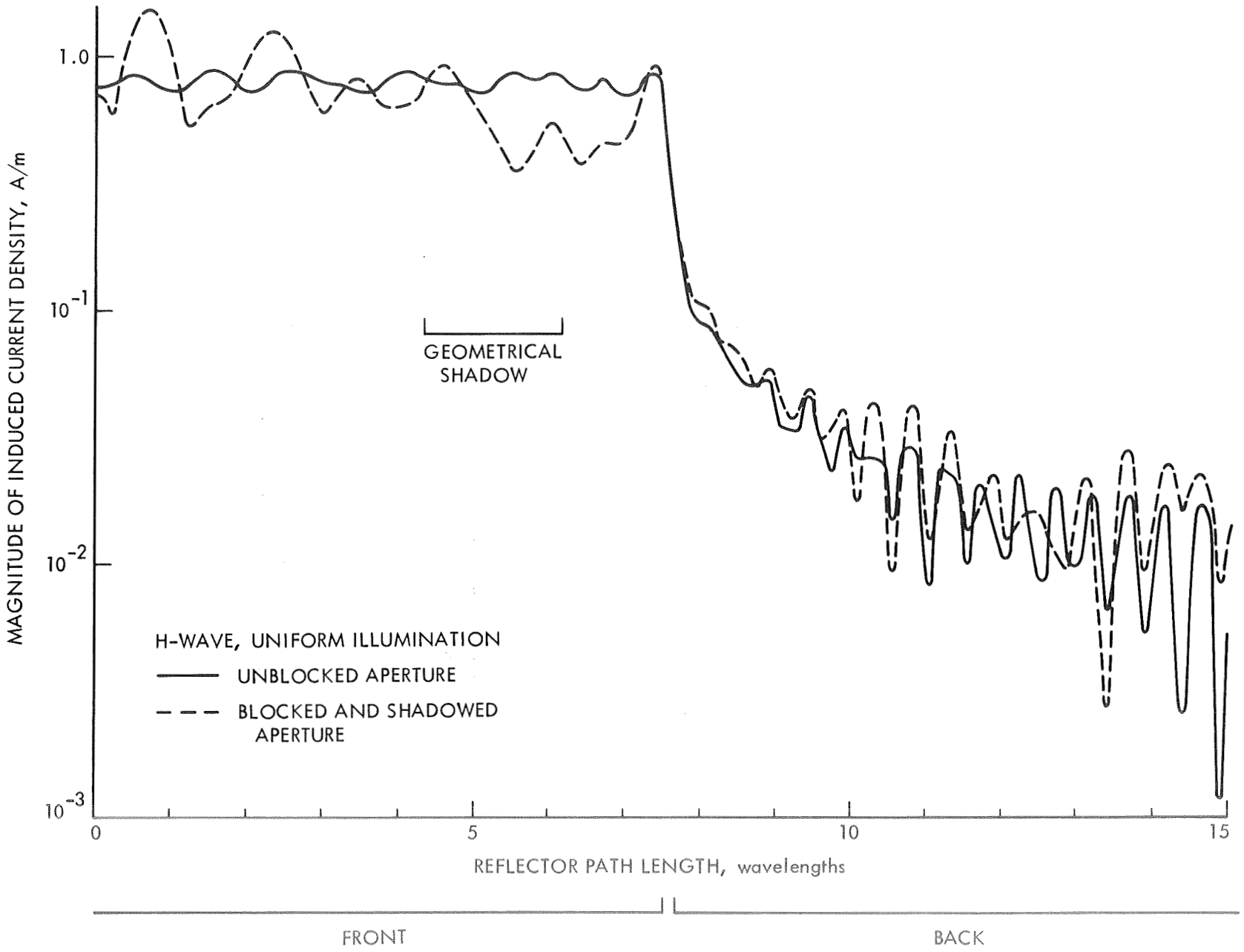

Fig. IV-28. Current Induced on Blocked and Shadowed Cylinder by Perpendicular Polarization

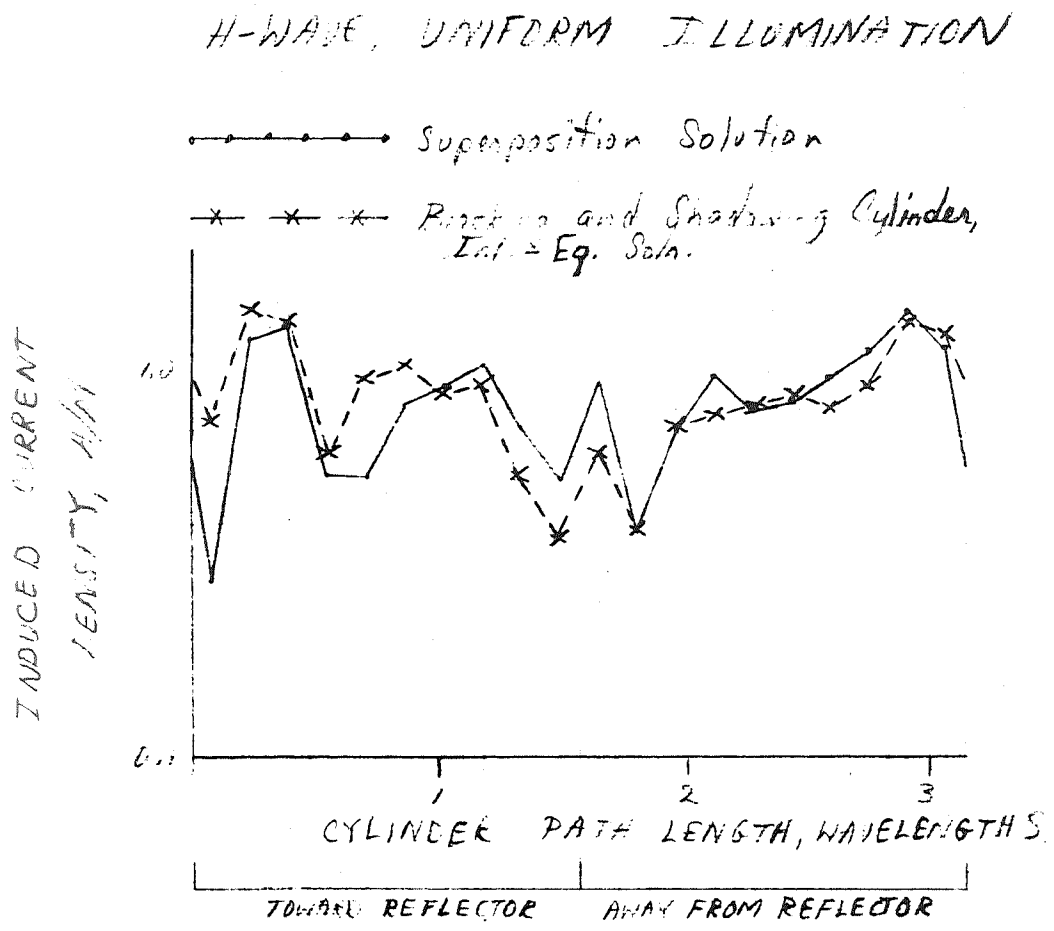

Fig. IV-29. Comparison of Currents Induced on Blocking and Shadowing Cylinder by Perpendicular Polarization

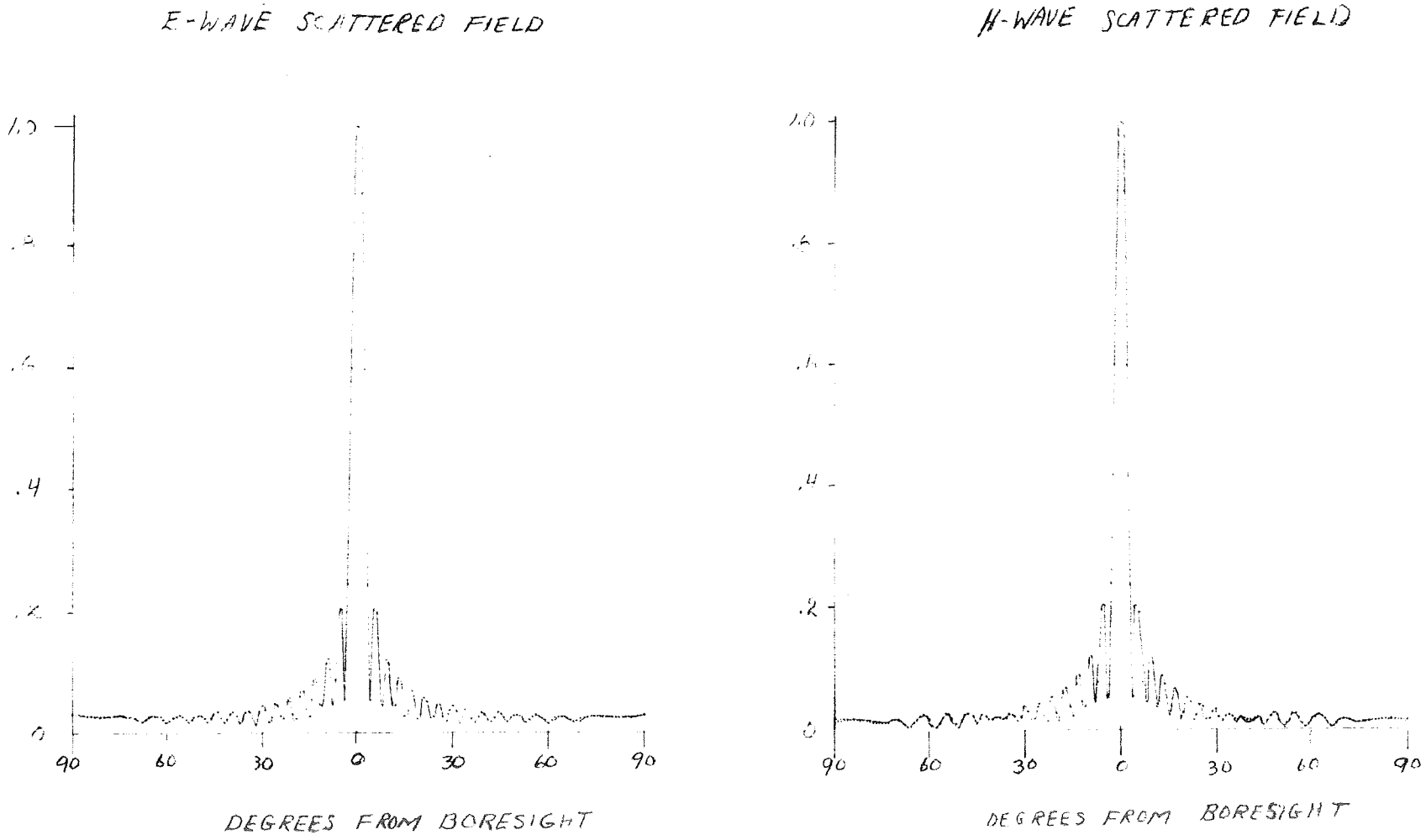

Fig. IV-30. Radiation Pattern of Uniformly Illuminated Parabolic Cylinder

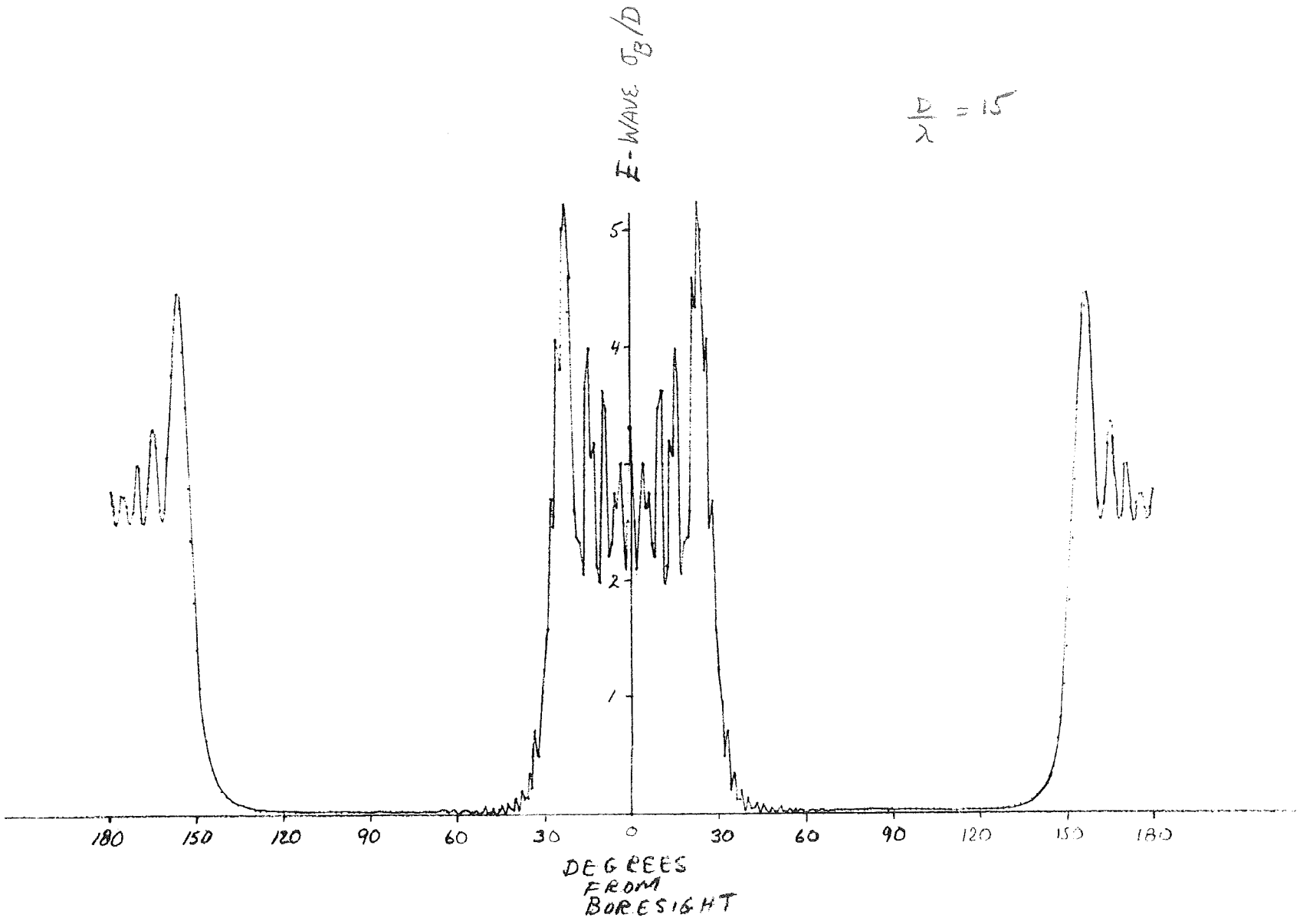

Fig. IV-31. Radar Cross-Section of Parabolic Cylinder (E-Wave)

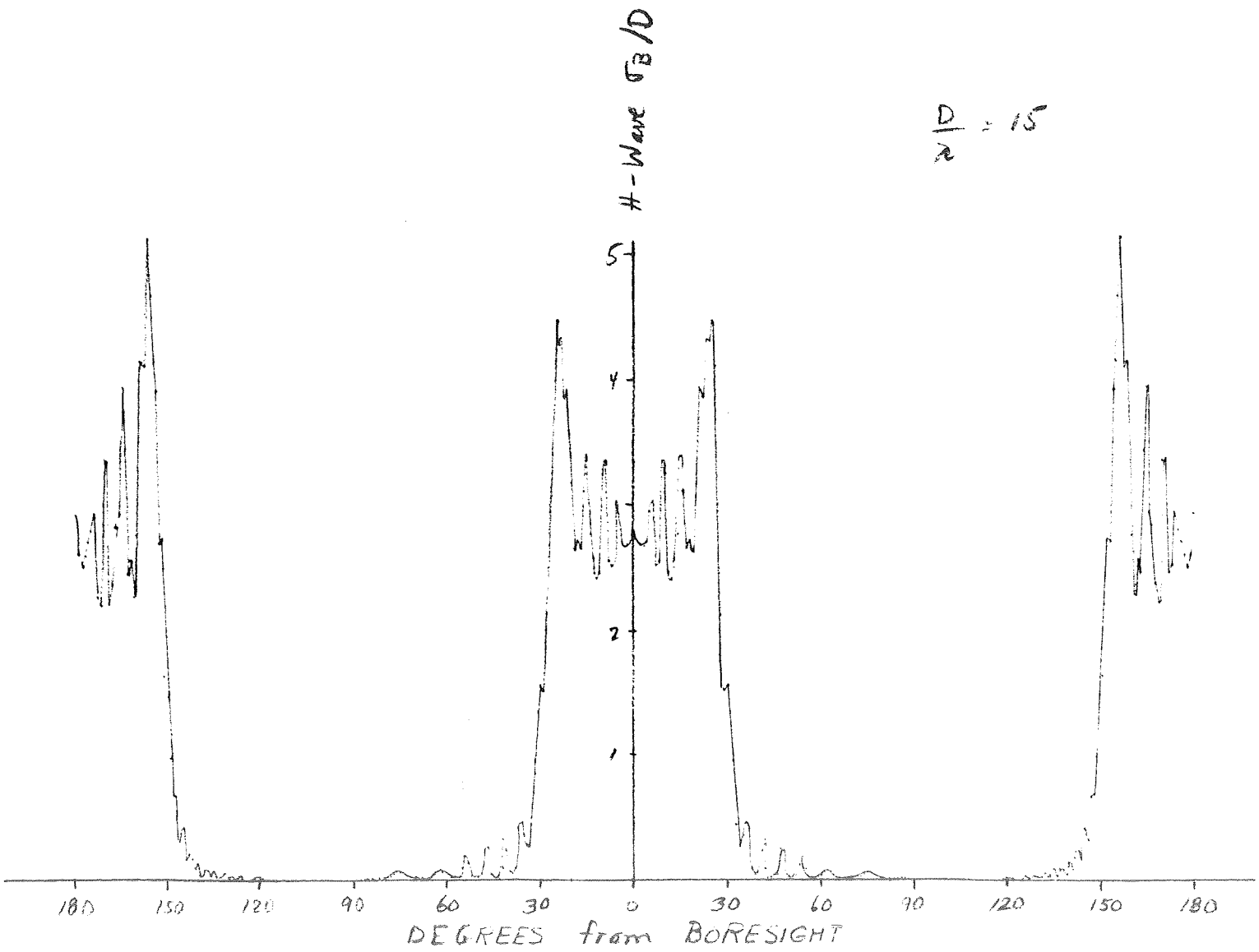

Fig. IV-32. Radar Cross-Section of Parabolic Cylinder (H-Wave)

V. CONCLUSIONS

Integral-equation techniques can be used to extend two-dimensional scattering theory to cylindrical scatterers of arbitrary cross-section. These results can be applied to many problems of practical interest in antenna design. For example, the problem of an aperture blocked by long, thin feed-support members is solved more accurately when the concepts of two-dimensional scattering theory are used in place of classical geometrical techniques. The problem of optimum member cross-section can be analyzed. It is also possible to analyze the problem of "double blocking", i.e., the situation when one or more blocking members lies in the shadow of another. It can be shown that when the separation is large it is necessary to consider that each member constitutes an independent blockage. This result is in direct contradiction to geometrical analysis.

It is also possible to extend similar techniques to dielectric and lossy cylinders, although these problems do not appear to be of immediate interest.

Apertures as large as 15 wavelengths or more in transverse dimension can be handled on a two-dimensional basis. It is expected that rotationally symmetric scatterers of comparable size can also be handled with similar techniques (although with different algorithms). Such analyses should be the next step in continuing studies.

APPENDIX A

DERIVATION OF THE BASIC TWO-DIMENSIONAL INTEGRAL EQUATION

Consider the "incident" or "exciting" field to be of the form

$$\Psi^i = \Psi^i_{xy} e^{-jk \sin \alpha z} \tag{A-1}$$

where Ψ^i_{xy} is a function of x and y (cf. Figure A-1) and $0 \leq \sin \alpha < 1$. Then, if the incident field satisfies the scalar Helmholtz equation

$$\nabla^2 \Psi^i + k^2 \Psi^i = 0 \tag{A-2}$$

the transverse part will be subject to an equivalent equation

$$\nabla^2_{xy} \Psi^i_{xy} + k^2 \cos^2 \alpha \Psi^i_{xy} = 0 \tag{A-3}$$

where ∇^2_{xy} is the Laplacian operator in the x-y plane, and may be chosen in any convenient separable coordinate system. The sources of the incident field will be located outside S_3. Consequently, equation (A-3) will be valid in regions V_1, V_2, and V of Figure A-1.

Similarly, it is convenient to define a two-dimensional Green's Function

$$G = G_{xy} e^{-jk \sin \alpha z} \tag{A-4}$$

where

$$G_{xy} = H_0^{(2)}(k \cos \alpha r) \tag{A-5}$$

and $H_0^{(2)}(x)$ is the Hankel function of the second kind and r is the distance measured from P, the field point. The transverse Green's function is also subject to a scalar Helmholtz equation:

$$\nabla_{xy}^2 G_{xy} + k^2 \cos^2 \alpha G_{xy} = 0 \qquad \text{(A-6)}$$

where equation (A-6) is valid in V_1, V_3, and V but not in V_2 since G_{xy} is singular at P.

Multiplying (A-3) by G_{xy} and (A-6) by Ψ_{xy}^i, and subtracting yields

$$\left(G_{xy} \nabla_{xy}^2 \Psi_{xy}^i - \Psi^i \nabla_{xy}^2 G_{xy} \right) = 0 \qquad \text{(A-7)}$$

which is valid in V_1, V, and V_3. Integrating over V_1 yields

$$\int_{V_1} \left(G_{xy} \nabla_{xy}^2 \Psi_{xy}^i - \Psi_{xy}^i \nabla_{xy}^2 G_{xy} \right) dV = 0 \qquad \text{(A-8)}$$

where this "volume" integral is taken over the cross-section of the cylindrical volume defined by V_1 and multiplied by a unit length (parallel to the z-axis). But a simple vector manipulation shows that

$$\nabla_{xy} \cdot \left(G_{xy} \nabla_{xy} \Psi_{xy}^i - \Psi_{xy}^i \nabla_{xy} G_{xy} \right) = G_{xy} \nabla_{xy}^2 \Psi_{xy}^i - \Psi_{xy} \nabla_{xy}^2 G_{xy}^i \qquad \text{(A-9)}$$

which, when inserted into (A-8) yields

$$\int_{V_1} \nabla_{xy} \cdot \left(G_{xy} \nabla_{xy} \Psi_{xy}^i - \Psi_{xy}^i \nabla_{xy} G_{xy} \right) dV = 0 \qquad \text{(A-10)}$$

Application of a two-dimensional divergence theorem yields

$$\int_{S_1} \left(G_{xy} \frac{\partial \Psi_{xy}^i}{\partial n} - \Psi_{xy}^i \frac{\partial G_{xy}}{\partial n} \right) dS = 0 \qquad \text{(A-11)}$$

where this "surface" integral is carried out over the contour S_1 and multiplied by a unit length, and $\bar{n}$ is out of V_1 into V.

The above manipulations can be repeated for the region defined by $V_1 + V$, yielding surface integrals over the enclosing surfaces $S_2 + S_3$:

$$\int_{S_2} \left(G_{xy} \frac{\partial \Psi^i_{xy}}{\partial n} - \Psi^i_{xy} \frac{\partial G_{xy}}{\partial n} \right) dS + \int_{S_3} \left(G_{xy} \frac{\partial \Psi^i_{xy}}{\partial n} - \Psi^i_{xy} \frac{\partial G_{xy}}{\partial n} \right) dS = 0 \qquad \text{(A-12)}$$

where the positive normal at each surface is directed <u>into</u> V. If the circle around P (which defines S_2) is allowed to shrink, then

$$G_{xy} = H_0^{(2)}(k \cos \alpha r) \xrightarrow[r \to 0]{} -j \frac{2}{\pi} \log \frac{\gamma k \cos \alpha r}{2} \qquad \text{(A-13a)}$$

$$\frac{\partial G_{xy}}{\partial n} = \frac{\partial H_0^{(2)}(k \cos \alpha r)}{\partial r} = -k \cos \alpha H_1^{(2)}(k \cos \alpha r) \xrightarrow[r \to 0]{} 2j/\pi r \qquad \text{(A-13b)}$$

Then, if Ψ^i_{xy} and $\frac{\partial \Psi^i_{xy}}{\partial n}$ remain finite as $r \to 0$,

$$\int_{S_2} \left(G_{xy} \frac{\partial \Psi^i_{xy}}{\partial n} - \Psi^i_{xy} \frac{\partial G_{xy}}{\partial n} \right) dS \xrightarrow[r \to 0]{} 4j \Psi^i_{xy}(P) \qquad \text{(A-14)}$$

Inserting this result into (A-12) yields

$$\int_{S_3} \left(G_{xy} \frac{\partial}{\partial n} \Psi^i_{xy} - \Psi^i_{xy} \frac{\partial G_{xy}}{\partial n} \right) dS = -4j \Psi^i_{xy}(P) \qquad \text{(A-15)}$$

The presence of the incident field will induce currents within S_1. The currents, in turn, will radiate a scattered field of the form

$$\Psi^s = \Psi^s_{xy} e^{-jk \sin \alpha z} \tag{A-16}$$

where

$$\nabla^2_{xy} \Psi^s_{xy} + k^2 \cos^2 \alpha \Psi^s_{xy} = 0 \tag{A-17}$$

in V_2, V_3, and V. Also, Ψ^s_{xy} is subject to a radiation condition such that

$$\int_{S_\infty} \left(G_{xy} \frac{\partial \Psi^s_{xy}}{\partial n} - \Psi^s_{xy} \frac{\partial G_{xy}}{\partial n} \right) dS = 0 \tag{A-18}$$

Manipulations similar to those leading to equation (A-10) yield

$$\int_{V_3} \nabla \cdot \left(G_{xy} \nabla_{xy} \Psi^s_{xy} - \Psi^s_{xy} \nabla_{xy} G_{xy} \right) dV = 0 \tag{A-19}$$

Converting this to an integration over S_3 and S_∞ which enclose V_3 yields

$$\int_{S_3} \left(G_{xy} \frac{\partial \Psi^s_{xy}}{\partial n} - \Psi^s_{xy} \frac{\partial G_{xy}}{\partial n} \right) dS + \int_{S_\infty} \left(G_{xy} \frac{\partial \Psi^s_{xy}}{\partial n} - \Psi^s_{xy} \frac{\partial G_{xy}}{\partial n} \right) dS = 0 \tag{A-20}$$

But from (A-18) the second term in (A-20) is zero. Hence

$$\int_{S_3} \left(G_{xy} \frac{\partial \Psi^s_{xy}}{\partial n} - \Psi^s_{xy} \frac{\partial G_{xy}}{\partial n} \right) dS = 0 \tag{A-21}$$

The volume integral of equation (A-19) could also be carried out over V, and the 1 converted into an integral over the surface $S_1 + S_2 + S_3$ enclosing V. The resulting equation is

$$\int_{S_1} \left(G_{xy} \frac{\partial \Psi^s_{xy}}{\partial n} - \Psi^s_{xy} \frac{\partial G_{xy}}{\partial n} \right) dS + \int_{S_2} \left(G_{xy} \frac{\partial \Psi^s_{xy}}{\partial n} - \Psi^s_{xy} \frac{\partial G_{xy}}{\partial n} \right) dS$$

$$+ \int_{S_3} \left(G_{xy} \frac{\partial \Psi^s_{xy}}{\partial n} - \Psi^s_{xy} \frac{\partial G_{xy}}{\partial n} \right) dS = 0 \qquad \text{(A-22)}$$

The third term of equation (A-22) has previously been shown to be zero. The second term, using the analysis leading to equation (A-15) is $+4j\Psi^s_{xy}(P)$. Consequently

$$\int_{S_1} \left(G_{xy} \frac{\partial \Psi^s_{xy}}{\partial n} - \Psi^s_{xy} \frac{\partial G_{xy}}{\partial n} \right) dS = -4j\Psi^s_{xy}(P) \qquad \text{(A-23)}$$

Finally, the total field will be defined as the sum of the incident and the reflected field, i.e.,

$$\Psi = \Psi^i + \Psi^s = \Psi_{xy} e^{-jk \sin \alpha z} \qquad \text{(A-24)}$$

where

$$\Psi_{xy} = \Psi^i_{xy} + \Psi^s_{xy} \qquad \text{(A-25)}$$

and

$$\nabla^2_{xy} \Psi_{xy} + k^2 \cos^2 \alpha \Psi_{xy} = 0 \qquad \text{(A-26)}$$

From the volume integral

$$\int_V \left(G_{xy} \nabla^2_{xy} \Psi_{xy} - \Psi_{xy} \nabla^2_{xy} G_{xy}\right) dV = 0 \tag{A-27}$$

it follows that

$$\int_{S_1} \left(G_{xy} \frac{\partial \Psi_{xy}}{\partial n} - \Psi_{xy} \frac{\partial G_{xy}}{\partial n}\right) dS + \int_{S_2} \left(G_{xy} \frac{\partial \Psi_{xy}}{\partial n} - \Psi_{xy} \frac{\partial G_{xy}}{\partial n}\right) dS$$

$$+ \int_{S_3} \left(G_{xy} \frac{\partial \Psi_{xy}}{\partial n} - \Psi_{xy} \frac{\partial G_{xy}}{\partial n}\right) dS = 0 \tag{A-28}$$

From the analysis leading to equation (A-14)

$$\int_{S_2} \left(G_{xy} \frac{\partial \Psi_{xy}}{\partial n} - \Psi_{xy} \frac{\partial G_{xy}}{\partial n}\right) dS \xrightarrow[r \to 0]{} 4j \Psi_{xy}(P) \tag{A-29}$$

Also, the field in the third term of equation (A-28) can be expanded into its component parts

$$\int_{S_3} \left(G_{xy} \frac{\partial \Psi_{xy}}{\partial n} - \Psi_{xy} \frac{\partial G_{xy}}{\partial n}\right) dS =$$

$$\int_{S_3} \left(G_{xy} \frac{\partial \Psi^i_{xy}}{\partial n} - \Psi^i_{xy} \frac{\partial G_{xy}}{\partial n}\right) dS + \int_{S_3} \left(G_{xy} \frac{\partial \Psi^s_{xy}}{\partial n} - \Psi^s_{xy} \frac{\partial G_{xy}}{\partial n}\right) dS$$

(A-30)

From equation (A-15) the first term on the right of equation (A-30) is $-4j\Psi^{i}_{xy}(P)$; from equation (A-21) the second term on the right is zero. Hence equation (A-28) becomes

$$\int_{S_1}\left(G_{xy}\frac{\partial\Psi_{xy}}{\partial n} - \Psi_{xy}\frac{\partial G_{xy}}{\partial n}\right)dS + 4j\Psi_{xy}(P) - 4j\Psi^{i}_{xy}(P) = 0 \qquad \text{(A-31)}$$

or, rearranging

$$\Psi_{xy}(P) = \Psi^{i}_{xy}(P) + \frac{j}{4}\int_{S_1}\left(G_{xy}\frac{\partial\Psi_{xy}}{\partial n} - \Psi_{xy}\frac{\partial G_{xy}}{\partial n}\right)dS \qquad \text{(A-32)}$$

Equation (A-32) provides the starting point for two-dimensional integral equation theory.

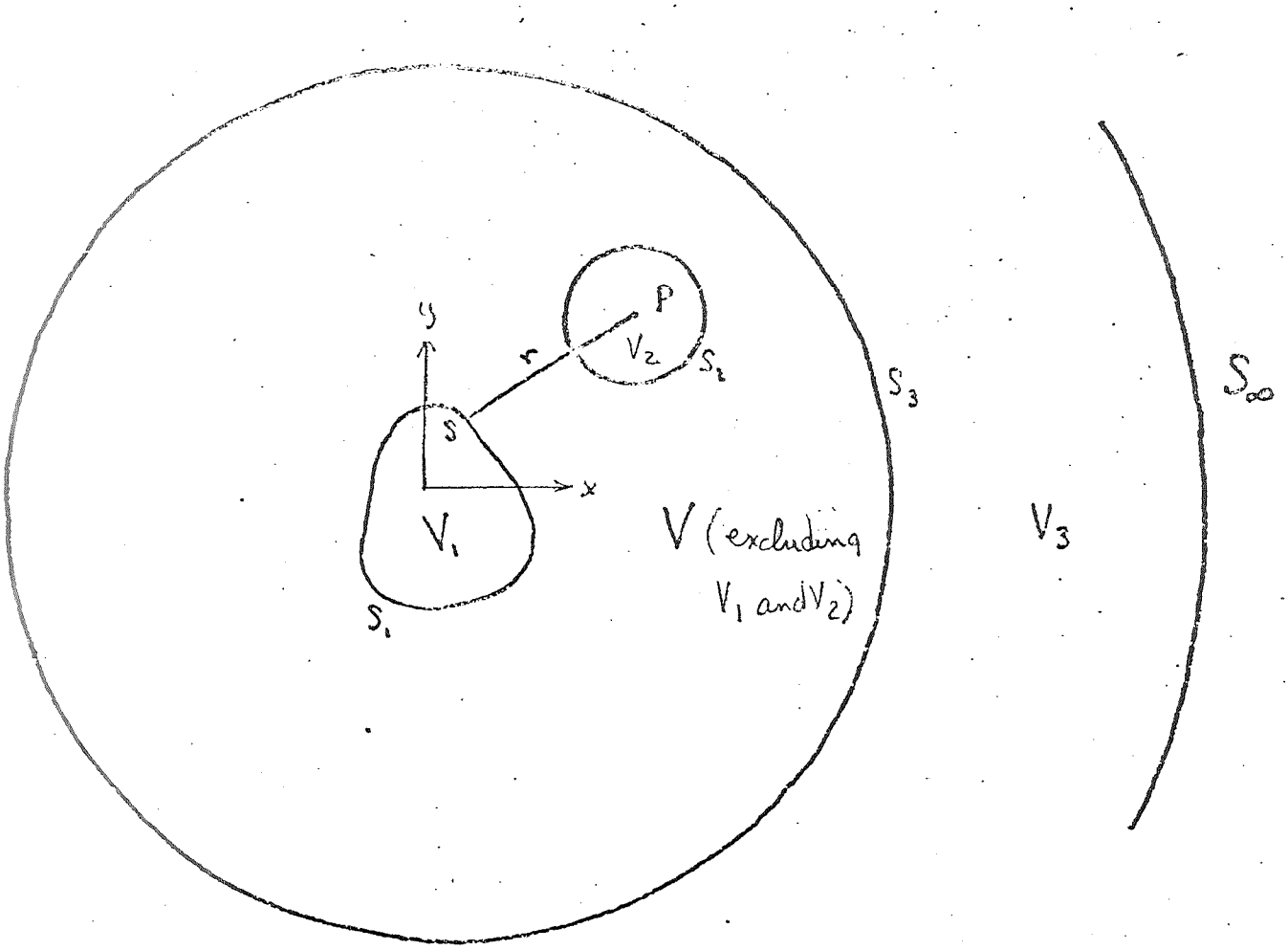

Fig. A-1. Geometry

APPENDIX B

SIMPLIFICATION OF THE MATRIX EQUATIONS IF THE GEOMETRY HAS A MIDPLANE OF SYMMETRY

If the xz plane is a symmetrical midplane for the scattering geometry, the matrix inversion process can be simplified considerably (Ref. 13). The basic equation to be inverted is the form

$$Zx = b \tag{B-1}$$

in which the matrix Z is square, 2k x 2k, and, because of the symmetrical midplane has

$$Z_{ij} = Z_{2k+1-i,\,2k+1-j} \tag{B-2}$$

This symmetry permits Z to be partitioned

$$Z = \begin{bmatrix} C & D \\ PDP & PCP \end{bmatrix} \tag{B-3}$$

where C and D are k x k matrices and P is the k x k permutation matrix

$$P = \begin{bmatrix} 0 & & & & 1 \\ & & & \cdot & \\ & & \cdot & & \\ & \cdot & & & \\ & 1 & & & \\ 1 & & & & 0 \end{bmatrix} \tag{B-4}$$

Let I denote the k x k identity matrix and define

$$R = \begin{bmatrix} I & P \\ I & -P \end{bmatrix} \tag{B-5}$$

It may then be verified that

$$R^{-1} = 1/2\begin{bmatrix} I & I \\ P & -P \end{bmatrix} \tag{B-6}$$

and

$$RZR^{-1} = \begin{bmatrix} C+DP & 0 \\ 0 & C-DP \end{bmatrix} \tag{B-7}$$

Making the linear change of variables

$$x = R^{-1}u \tag{B-8}$$

and premultiplying equation (B-1) by R gives

$$RZR^{-1}u = Rb \tag{B-9}$$

In view of the partitioned form of RZR^{-1}, equation (B-9) has effectively decoupled the original set of 2k equations into two separate sets of k equations.

To display these k x k systems more explicitly, partition x, u, and b in the form

$$X = \begin{bmatrix} y \\ z \end{bmatrix} \tag{B-10a}$$

$$u = \begin{bmatrix} v \\ w \end{bmatrix} \tag{B-10b}$$

$$b = \begin{bmatrix} e \\ \\ f \end{bmatrix} \tag{B-10c}$$

Then, by using equations (B-5) and (B-7), equation (B-9) can be written as a pair of k x k systems.

$$(C + DP)v = e + Pf \tag{B-11a}$$

$$(C - DP)w = e - Pf \tag{B-11b}$$

Inverting these equations for v and w to yield u; this result, in turn yields y and z, the partitioned components of x:

$$y = (v + w)/2 \tag{B-12a}$$

$$z = P(v - w)/2 \tag{B-12b}$$

REFERENCES

1. Bathker, D. A., and Brown, D. W., "Large Ground Antenna Performance with Solar Noise Jamming," Proc. IEEE, Vol. 54, No. 12, pp. 1949-1951, Dec. 1966.

2. Andreasen, M. G., "Scattering by Conducting Rectangular Cylinders," IEEE Trans. on Antennas and Propagation, Vol. AP-12, No. 6, pp. 746-754, Nov. 1964.

3. Van Bladel, J., Electromagnetic Fields, McGraw-Hill Book Company, New York, 1964, pp. 387-397.

4. Oshiro, F. K., and Cross, R. C., "A Source Distribution Technique for Solution of Two-Dimensional Scattering Problems," Phase III Report, NOR 66-74, March 1966, Northrop Corporation, Hawthorne, California.

5. Andreasen, M. G., "Scattering from Bodies of Revolution," IEEE Trans. on Antennas and Propagation, Vol. AP-13, No. 2, March 1965, pp. 303-310.

6. Oshiro, F. K., and Mitzner, K. M., "Digital Computer Solutions of Three-Dimensional Scattering Problems," presented at 1967 IEEE International Antennas and Propagation Symposium, Ann Arbor, Michigan, October 1967.

7. Mautz, J. R., "Radiation and Scattering from Bodies of Revolution," Ph. D. Dissertation, Syracuse University, 1969.

8. Ruze, J., "Feed Support Blockage Loss in Parabolic Antennas," Microwave Journal, Vol. II, No. 12, pp. 76-80, Dec. 1968.

9. Kay, A. F., "Electrical Design of Metal Space Frame Radomes," IEEE Trans. on Antennas and Propagation, Vol. AP-13, No. 2, pp. 188-202, March 1965.

10. Stratton, J. A., Electromagnetic Theory, McGraw-Hill Book Company, New York, 1941, pp. 354-5.

11. R. F. Harrington, Time-Harmonic Electromagnetic Fields, McGraw-Hill Book Company, Inc., 1961, Section 5-9.

12. Mei, K. K. and Van Bladel, J. G., "Scattering by Perfectly-Conducting Rectangular Cylinders," IEEE Trans. on Antennas and Propagation, Vol. II, pp. 185-192, March 1963.

13. Lawson, C. L., "Solution of a Linear Algebraic System Whose Matrix Elements Satisfy $A_{ij} = A_{n+1-i,\, n+1-j}$," JPL Section 314 Technical Document 187, April 9, 1968.

NASA — JPL — Coml., L.A., Calif.